Doctoral Thesis

A Study on Intrinsic Graphene Defects of Different Origins in CVD-Grown Graphene

Yongsu Jo

Department of Materials Science and Engineering

Graduate School of UNIST

2020

A Study on Intrinsic Graphene Defects of Different Origins in CVD-Grown Graphene

Yongsu Jo

Department of Materials Science and Engineering

Graduate School of UNIST

A Study on Intrinsic Graphene Defects of Different Origins in CVD-Grown Graphene

A dissertation
submitted to the Graduate School of UNIST
in partial fulfillment of the
requirements for the degree of
Doctor of Philosophy

Yongsu Jo

6. 8. 2020 of submission

Approved by

Advisor
Soon-Yong Kwon

A Study on Intrinsic Graphene Defects of Different Origins in CVD-Grown Graphene

Yongsu Jo

This certifies that the dissertation of Yongsu Jo is approved.

6/8/2020 of submission

signature

Advisor: Soon-Yong Kwon

signature

Kibog Park: Thesis Committee Member #1

signature

Myoung Hoon Song: Thesis Committee Member #2

signature

Zonghoon Lee: Thesis Committee Member #3

signature

Jinsung Kwak: Thesis Committee Member #4;

ABSTRACT

Chemical vapor deposition method has been spotlighted as a tool growing large-area, good quality, mass-producible and uniform graphene. In particular, the copper that grows a uniform monolayer of graphene has attracted researchers' attentions as a graphene growth substrate. However, CVD graphene growth has a nature that graphene has various intrinsic defects such as point defects, grain boundaries, and wrinkles, undermining the properties of graphene. So, it is important to visualize various intrinsic defects in terms of optimizing graphene growth.

Firstly, we examined selective oxygen permeation through atomic structural defects in CVD-grown graphene/copper composites measured by optical and electron microscopies. Using an simple air oxidation of graphene coated copper foils with heating of 200 °C, we developed a simple and large area characterization tool to visualize intrinsic graphene defects induced by different origins such as nucleation sites, inter grain boundaries and intra grain boundaries from CVD-grown graphene. The oxidation conduct of copper can vary with disorder of graphene structures according to sources of various graphene intrinsic defects such as growth condition, crystallographic orientations of copper substrates and growth rate. From the experimental and computational experiments, we found that oxygen atoms were dissociated from the water vapor of air are main origins oxidizing copper surface under graphene and selective oxygen permeation occurred at Stone–Wales defects into graphene membrane promoted by other accumulated oxygen atoms as catalyst.

Secondly, we use HCl etching method to systemically investigate the water permeable origins on the graphene grown on copper by CVD observing copper etching pits through OM and SEM. When we observed the distribution of these etching pits through SE and BSE mode of SEM, it was found the copper etching pits were observed at the intersection of wrinkles of CVD-grown graphene and copper step bunches. In addition, it was also confirmed that nanosized ruptures, cracks, and holes were formed in folded graphene wrinkles through TEM. The HCl etching method can determine where the water permeations occur in the CVD-grown graphene, and these results will contribute to optimizing the graphene growth as production of water impermeable layer.

Finally, we described a large-area technique to enhance impermeability of graphene by amorphous carbon layer deposited by an electron beam, sputtered carbon, and CH_4 plasma. It was utilized to passivate the graphene nanosized ruptures, cracks and holes less than 3nm, developed on intersecting points of wrinkle and copper step bunch. In addition, the wrinkles on the part of multilayer graphene also had excellent water impermeability to copper etchants. Applying these carbon-based layers, flexible, transparent, and thin barrier films will be developed for water impermeable electrodes and substrates to safely protect future ubiquitous electronics from ambient air being exposed to everyday life

CONTENTS

LIST OF FIGURES

Figure 2.13 (**a**) An OM image of the graphene islands after transfer onto silicon oxide substrate. (b-d) Corresponding Raman mapping images of the D (**b**), G (**c**), and 2D band (**d**), respectively. (**e**) Raman single spectrum taken from colored arrows along the black dotted line in d.

Figure 2.14 Raman maps of the D/G bands of graphene islands with the 4-lobe shape that were grown on Cu foils at 1000 °C for 30 sec (**a**), 15 sec (**b**), and 5 sec (**c**) and then transferred onto the silicon oxide substrate.

Figure 2.15 (**a**) EBSD images with mapping of copper foil after partially graphene growth at 1000 ºC. The EBSD data show that Cu (100) are abundant area (left) and, in some regions, having orientations of (111), (101), and high-index orientations (right). (b-f) SEM images of partially grown graphene diverse orientation of (**b**, **c**) (100), (**d**) (101), (**e**) (111), and (**f**) the boundary between (100) and (111) after oxidation. (**g**) Raman D/G mapping image of the partially grown graphene on Cu (111) after transfer

Figure 2.16 OM images of the partially grown graphene on Cu (100) after oxidation method under various growth rate of graphene. Graphene were partially grown (**a**) at 1050 °C for 30 sec with CH_4 of 10 sccm and H_2 of 5 sccm, (**b**) at 1000 °C for 30 sec with CH_4 of 10 sccm and H_2 of 20 sccm, and (**c**) at 1,000 °C for 3min with CH_4 of 2 sccm and H_2 of 5 sccm

Figure 2.17 (**a**) SEM image of partially grown graphene on Cu (100) after oxidation. Inset indicates a highly magnified SEM image of in (a). SEM images of the as-grown graphene composites after oxidation for (**b**) 120 and (**c**) 240 min. Blue arrows indicate multilayer formed on nucleation center

Figure 2.18 (**a**) OM image and Raman mapping images for G/2D and D of partially grown graphene having a multilayer, after transfer onto silicon oxide. White arrows indicate multilayer formed on nucleation center

Figure 2.19 (**a**) SEM images of the graphene containing folded wrinkles after oxidation. The right is a high magnified SEM image, and the red arrows indicate a kink of oxidation features formed on the wrinkle. (**b**) Scheme of the folded wrinkles in graphene acted as effective barrier film to air oxidation

Figure 2.20 SEM images of as-grown graphene composites after air oxidation at 200 °C (**a**) for 120min under vacuum (**b**) for 120min in dry oxygen environment of 150 Torr, (**c**) for 120min in air (RH ≈ 30–40%), (**d**) for 60min in a humid oxygen environment (RH ≈ 80%), and (**e**) for 60min in a humid nitrogen environment (RH ≈ 50%).

Figure 3.9 Typical SEM images of as-grown graphene without (**a**) and with heating in vacuum at 500 °C for 1 min (**b**) after HCl etching method. (**c,d**) High magnification SEM images of a yellow square in (**b)** detected by SE (**c**) and BSE mode (**d**).

Figure 3.10 A typical OM and an AFM image of the as-grown graphene surface on Cu (100) (**a,b**) and Cu(111) (**c,d**). In **a** and **c**, right panels are corresponding EBSD maps.

Figure 3.11 (**a**) Lowly magnified TEM image of CVD-grown graphene having the wrinkle marked by a yellow arrow. (**b**) Highly resolved TEM image of wrinkle. Inset of (**b**) is a scheme of folded wrinkle structure. (**c**–**e**) Highly magnified TEM images of intrinsic defects located at wrinkle in (**b**) (**c**) nanosized ruptures located at the edge of wrinkle, (**d**) cracks, and (**e**) holes.

Figure 4.1 (**a**-**e**) Typical SEM images of as-grown graphene irradiated by electron beam for (**a**) 10, (**b**) 20, (**c**) 30, (**d**) 40, and (**e**) 50 min after etching in a 3.7 wt% HCl solution for 10 min. Lower panels in (**a**-**e**) are high-magnification SEM images of the a-C region. Blue arrows and red-dotted circles indicate wrinkles and Cu etch pits, respectively. (**f**) Thickness of a-C layer depending on irradiation time under the same irradiation conditions.

Figure 4.2 (**a,b**) OM images of the as-grown graphene deposited by amorphous carbon layer induced by electron beam before (**a**) and after dipping in an aqueous HCl solution (3.7 wt%) for 20 min (**b**). In **b**, right indicates highly magnified OM images of two squares. (**c-d**) Representative BSE-SEM and AFM images of as-grown graphene without and with a-C layer after the HCl treatment. (**f**) A BSE-SEM image of as-grown graphene after patterning with amorphous carbon along wrinkle of graphene after HCl etching method for 20 min.

Figure 4.3 OM image of graphene island transferred onto silicon oxide substrate after the electron beam treatment (**b**) Raman spectra from red, blue, and green circles in **a**. (**c**) Raman spectra after the e-beam treatment on a SiO_2/Si, in which the D bands are significantly increased because of the interaction of the energetic electrons with both Gr and SiO_2.

Figure 4.4 OM images of graphene surfaces selectively coated with the a-C layer using the accelerated electron-beam of (**a**) 15, (**b**) 10, (**c**) 5, (**d**) 1 kV, respectively. In **a**-**d**, right indicate representative OM images taken from the region

LIST OF TABLES

CHAPTER 1

Introduction to intrinsic defects of CVD-grown graphene

1.1 Graphene

Graphene is ultrathin 2D materials of sp^2-hybridzied carbon allotrope with honeycomb lattice[13]. Overlapping π-orbitals and large scattering path of graphene contribute to high room-temperature mobility. Graphene exhibits high optical transparency (97.7 %), good electrical and thermal conductivity, and good mechanical property. In this regard, graphene has a potential to several extraordinary applications[14-17].

Although graphene has one atomic thickness, it is interesting to have impermeability. π-orbitals of graphene forms a defense for other molecules[18], blocking the gap within its romantic rings by delocalized cloud (Figure 1.1). The repelling field, which does not permit tiny molecules such as He and H_2, is created and the penetration does not occur even if the difference of pressure is 1-5 atm pressure at room temperature (Figure. 1.2). The bond length of C-C in graphene is 0.142 nm, so the graphene has the size of pore as 0.246 nm. In consideration of van der Waals radius, the pore size would be predicted to decrease to 0.064 nm. The tiny hole is smaller than the van der Waals radius of small molecules like H_2 and He.

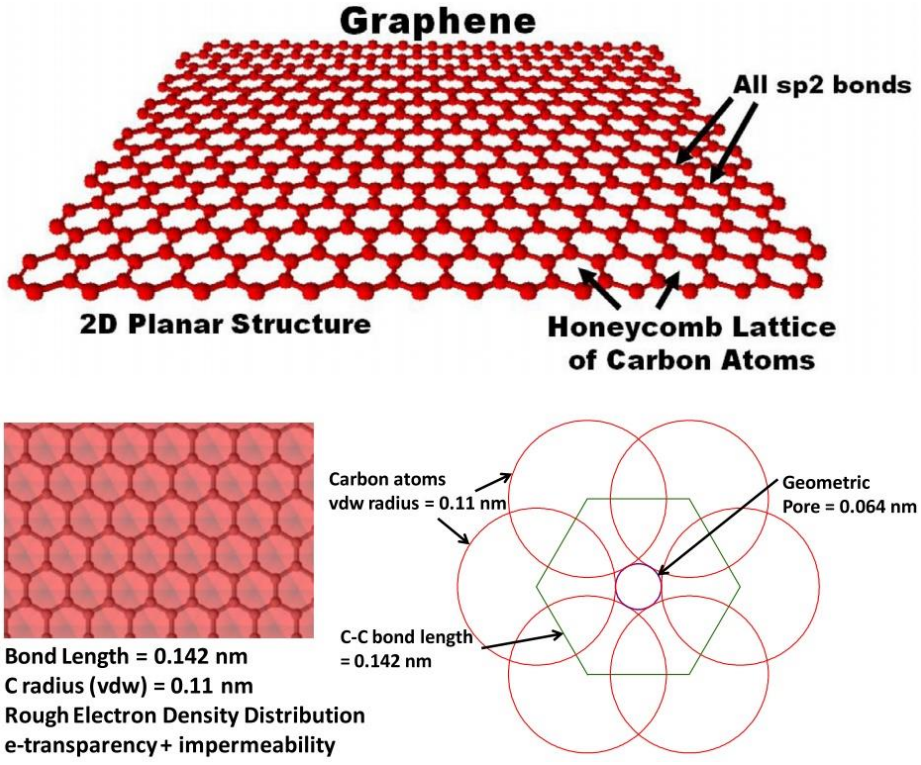

Figure 1.1 sp^2 hybridized carbon atoms formed in a honeycomb lattice of graphene lattice. Reproduced from ref [1]

.

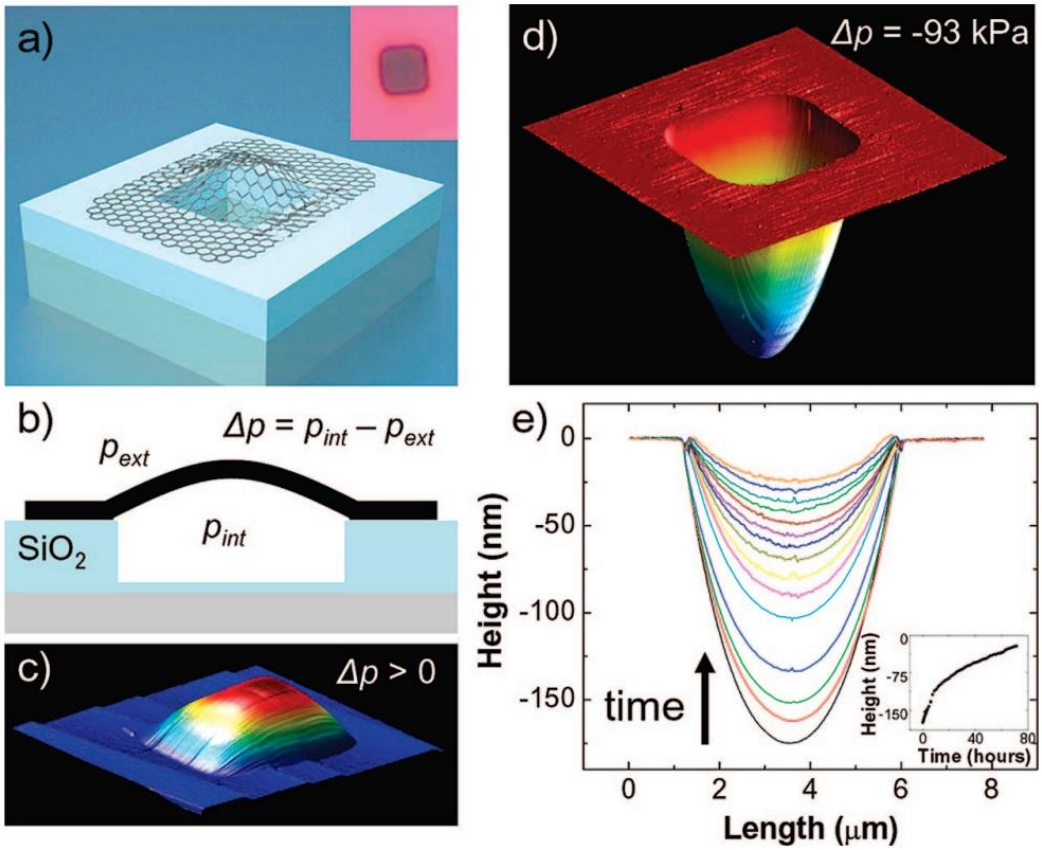

Figure 1.2 Impermeability and stiffness of graphene sealed microchamber. Reproduced from ref [2].

1.2 Synthesis of graphene

Since the exfoliation of graphene, researchers have tried to develop the techniques of handling high quality, large area and uniform graphene. The representative synthesis methods for graphene are mechanical exfoliation, chemical exfoliation, epitaxy growth, and chemical vapor deposition (CVD) method[13, 19-21].

Graphite is composed of stacked layers of many graphene sheets, bonded together by weak van der Waals force. High quality graphene can be obtained from high crystalline graphite by detaching the weak vdw bonding. The mechanical exfoliation is that graphite is placed on scotch tape and repeatedly peeled off for cleaving the weak bonding between layers. The graphene gained by mechanical exfoliation from highly oriented pyrolytic graphite has the highest quality for ideal material study, but it has a disadvantage of low production yield.

For increasing production yield, chemical exfoliation has been introduced to disperse graphite into water-based solution by chemical modification as graphite oxide. Graphite is converted to a layered stack of crumbled sheets through oxidation such as Hummers' method, and completely exfoliated to graphene oxide by additional mechanical energy such as sonication. In addition to that, the exfoliated graphene oxide can be reduced to nano-sized graphene. Furthermore, for omitting oxidation and reduction process, graphite is also intercalated with Li^+ ion which provokes a vigorous reaction in water. The chemical exfoliated graphene has the highest production yield, but it has a disadvantage of low quality nature with nano-sized graphene.

For ensuring good quality and large area growth, SiC wafer is used to grow epitaxially graphitic layers on the silicon and carbon faces by sublimating Si atoms. The epitaxy-grown graphene on SiC has high-quality with hundreds of micrometers in size, but the SiC wafer is high cost. Therefore, SiC epitaxy growth is unsuitable for graphene industry.

For large-area, uniform, and good-quality graphene, CVD method is introduced to react gas or solid precursors on transition metal surface. At high temperature and catalytic metal surface, hydrocarbon sources are decomposed, and the cracked carbon sources are soluble in metal or attached on surface with crystallinity. The metal substrate not only act as catalyst for reducing activation energy for the reaction, but also affect the mechanism of graphene. The solubility of carbon is different with various metal substrates, and this determines the mechanism of graphene growth. For high carbon solubility, the graphene is segregated out from metal surface during cooling. However, for low carbon solubility as copper, carbon atoms nucleate on surface, and then they are laterally grown around the nucleus forming graphene domains. The surface growth process is over when the graphene domains are stitched each other. The copper substrate is not only applicable for growing good-quality, large-area, and uniform monolayer graphene, but also have the ability to break self-limited surface growth mode for

growing bi- and few layer graphene.

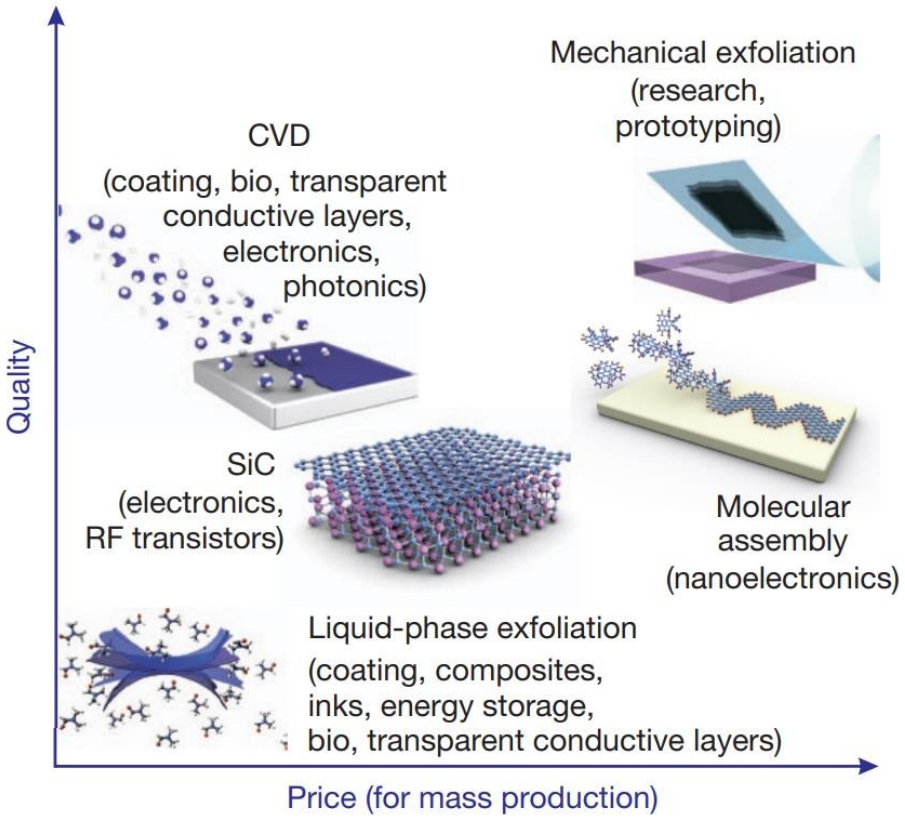

Figure 1.3 Several methods of graphene production. Reproduced from ref[3]

Method	Crystallite size (μm)	Sample size (mm)	Charge carrier mobility at RT($cm^2V^{-1}s^{-1}$)	Application
Mechanical exfoliation	> 1,000	> 1	≥ 100,000	Research
Chemical exfoliation	≤ 0.1	Infinite	100	Coatings, ink, composites, and so on
Epitaxy	50	100	10,000	High-frequency transistors, electronic devices
CVD	1,000	~1,000	≥ 10,000	Photonics, nanoelectronics, conductive layers, barrier film

Table 1 Properties of graphene synthesized with different methods. Reproduced by ref[3]

Metal (bulk)	Carbon solubility at 1000 ℃ (at. %)	Primary growth mechanism
Copper (Cu)	0.04	Surface deposition/penetration
Cobalt (Co)	3.41	Segregation
Platinum (Pt)	1.76	Segregation/surface deposition
Nickel (Ni)	2.03	Segregation/surface deposition
Palladium (Pd)	5.98	Segregation
Iron (Fe)	7.89	Segregation
Germanium (Ge)	0.00	Surface deposition

Table 2 The information about growth mechanism and carbon solubility along various transition metal for CVD graphene. Reproduced by ref [12]

1.3 Intrinsic defects of CVD-grown graphene

CVD method can grow large area, good quality, and uniform graphene on metal surface, but the graphene is polycrystalline with various defects as intra-grain boundaries, inter-grain boundaries, points defects, and wrinkles falling short of ideal exfoliated graphene. As shown in Figure 1.4, graphene islands on metal surface was not a single orientation of graphene through selected-area diffraction (SAED) pattern. The individual islands had lobes having different orientation. In Figure 1.4b-e, each 4 lobes of different orientated graphene domains came together at the center of the island sharing the same nucleation site as intra-grain boundaries. Most of graphene produced by CVD is polycrystalline to have inter-grain boundaries between graphene islands expanded from many nucleation sites as shown in Figure 1.5. The grain boundaries are origins of charge carriers scattering, so degrade performance of graphene-based devices relative to exfoliated idea graphene. Not only various line defects of graphene are distributed in CVD-grown graphene, but also some 0D structural defects also are formed during growth and processing as shown in Figure 1.6.

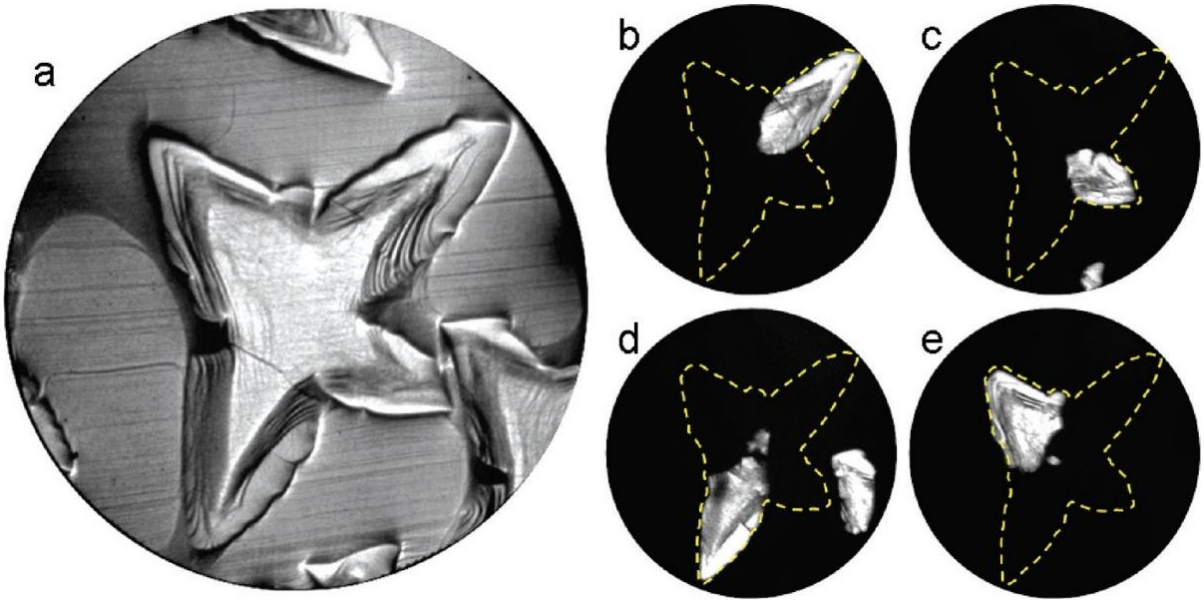

Figure 1.4 Bright and dark field low-energy electron microscope image of partial grown graphene on Cu (100). Reproduced from ref [4]

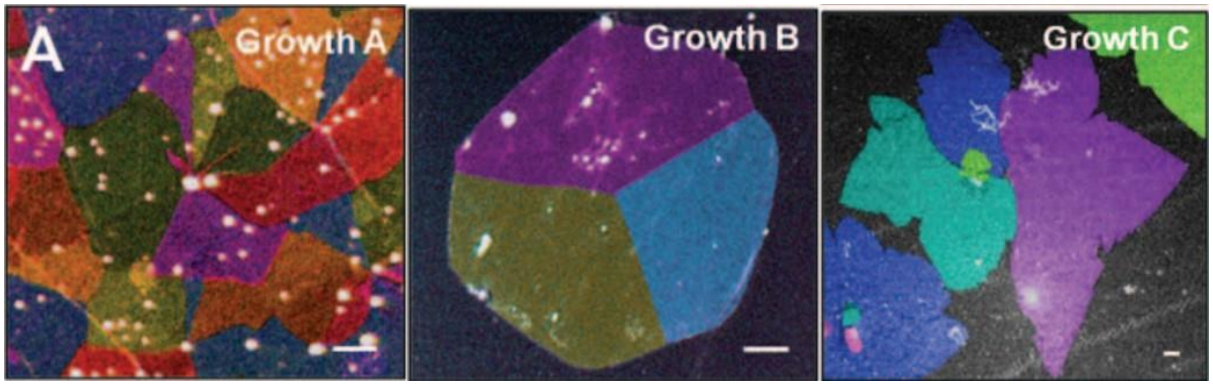

Figure 1.5 Composite imaginary colored dark-field TEM image of graphene grown by CVD. Reproduced from ref[5]

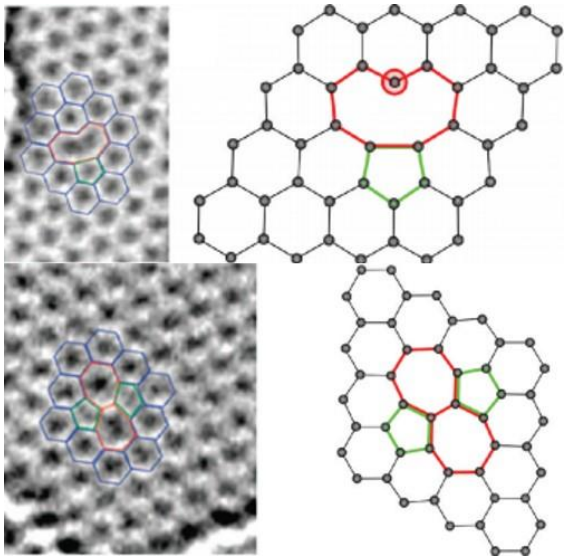

Figure 1.6 Experimental TEM image of various vacancies. Reproduced by Ref [6]

Many researchers have been trying to visualize various defects of graphene with large area as boundaries between graphene islands, point defects, and intra-boundaries for optimizing graphene growth condition, since the structural defects of CVD-grown graphene were observed through TEM, Raman spectroscopy, STM, LEEM, and SEM because of their microscopic and spectroscopic observation. The microscopic and spectroscopic observations are only applicable for domains that are less than a few micrometer size. There are some techniques, which can visualize the distribution of graphene defects with large area such as liquid crystal method, ultraviolet (UV) method, and metal deposition through atomic layer deposition as shown in Figures 1.7-1.19. Liquid crystal method visualizes the domains and grain boundaries of graphene using alignment of nematic liquid crystal molecules with strong epitaxial interaction. And this method is applied to the graphene on any substrates, but the information of substrate is also reflected on images. UV method also observes the grain boundaries of graphene through optical microscopy. However, the method is quiet destructive for

graphene samples and mainly visualizes the distribution of 1D defects as grain boundaries. ALD method also deposits Pt particles on various defects of graphene, not only 1D grain boundaries but also nucleation defects. Conductivity of graphene is enhanced with Pt deposition on graphene defects, however the nature of graphene is loss because of bonding of Pt to the defects and high cost and long time are required for deposition Pt particles through ALD. The method, which is nondestructive, facile, and low cost, is required for visualizing the defects of CVD grown graphene for evaluation of graphene nature in industry level.

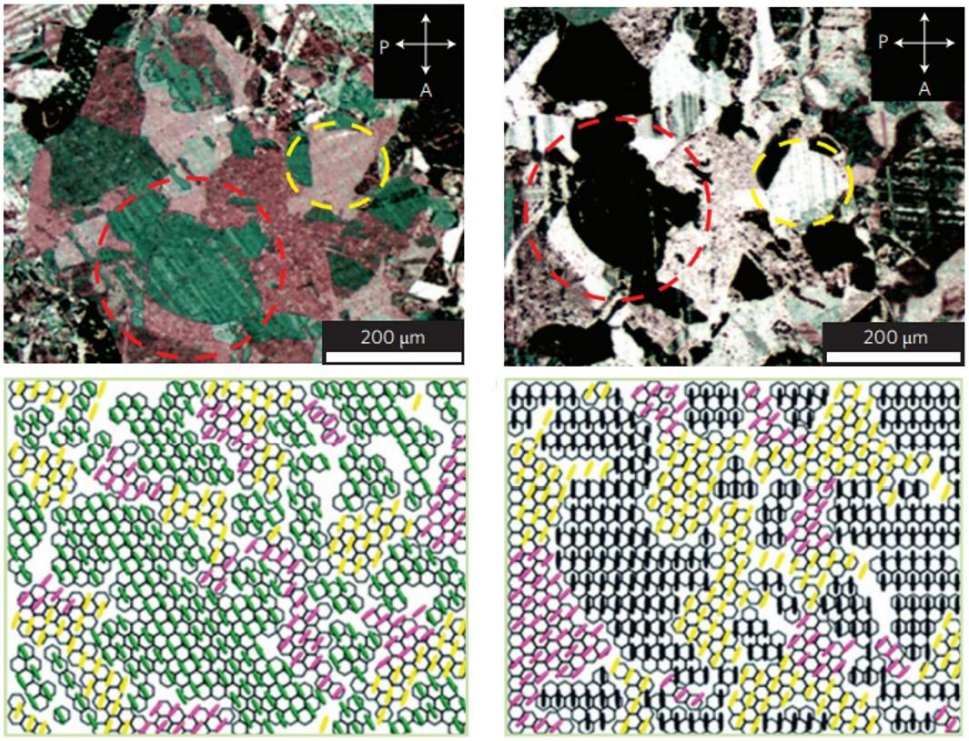

Figure 1.7 OM images of the graphene grain boundaries using liquid-crystal method. Reproduced from ref[7]

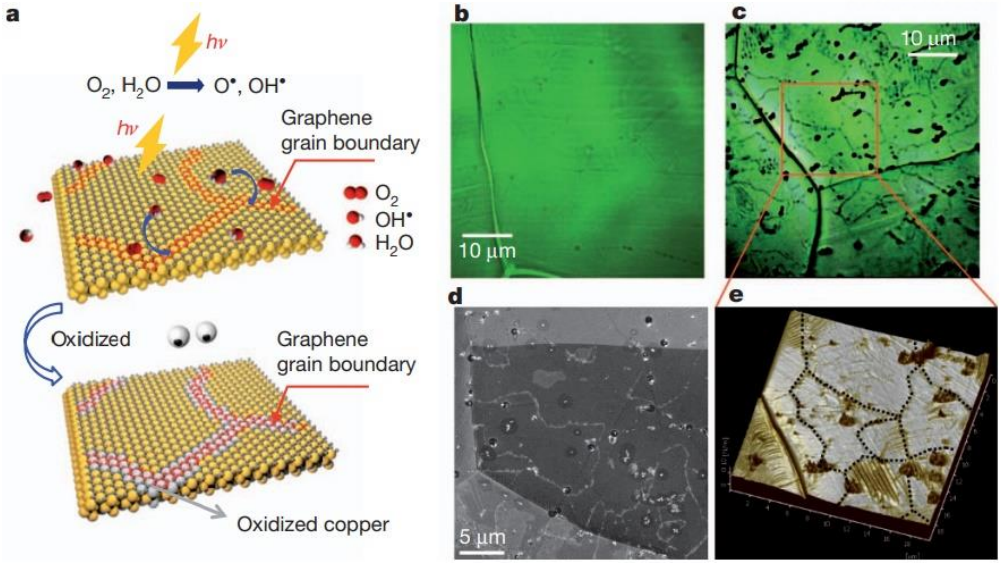

Figure 1.8 OM images of graphene domains after UV exposure with humid air. Reproduced from ref[8]

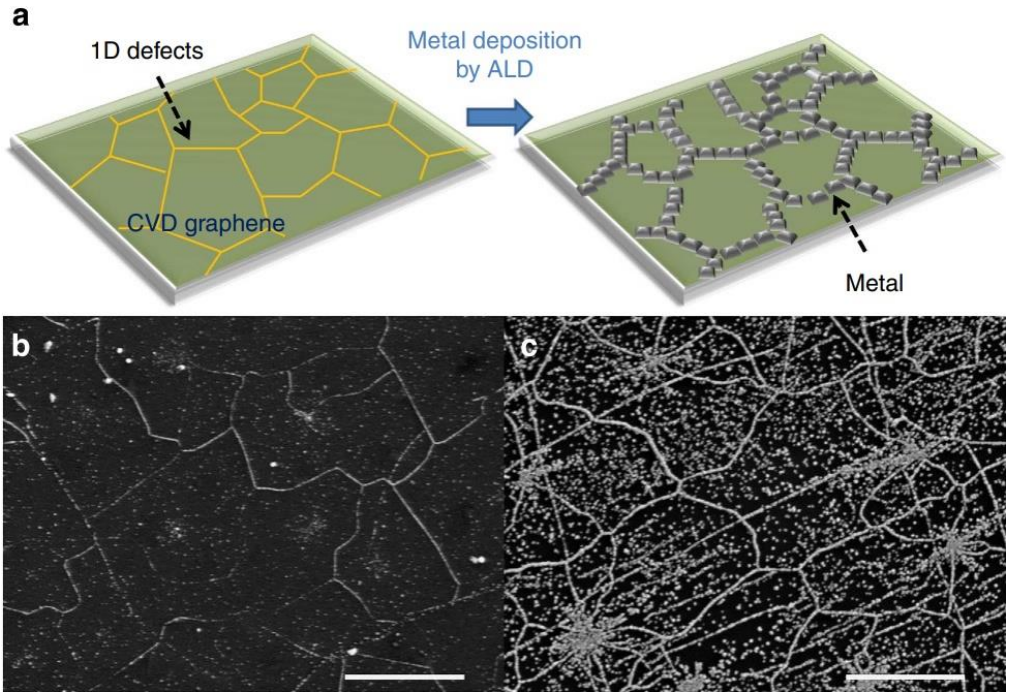

Figure 1.9 Selective Pt deposition using ALD on CVD grown graphene. Reproduced from ref[9]

Graphene has been attracted as barrier film, which protects substrates from reactive environments being significant to industry and science field. There are some techniques which evaluate passivation

of graphene through substrate etching solution. HCl solution is good equipment for tracking water permeable origins for CVD grown graphene on copper to etch the copper substrate under graphene as shown in Figure 1.10. HCl with large ionization constant is soluble in water making chloride anions and hydronium cations. When the HCl solution is reacted with Cu, compound of Cu and Cl was formed as $CuCl_2$ or $H2CuCl_4$ being soluble in water. Through this protocol, the copper contacting to HCl solution is etched out and etching fits are formed on surface, which can be observed by optical microscope or SEM. Because the reaction between HCl solution and copper is required with contact, the HCl solution can be the equipment for evaluating water vapor transmission rate (WVTR) As shown in Figure 1.11. WVTR is correlated with the total area of HCl solution etching pits. For study the graphene composites as water impermeable layer, the HCl method can be good tool to evaluate impermeability. The defects of CVD grown graphene are inevitable to industrial application. The tools, which trace structural defects and water permeable origins of CVD grown graphene, are integral for evaluating graphene based composites as water impermeable substrates and electrodes for thin, transparent, and flexible electronic devices.

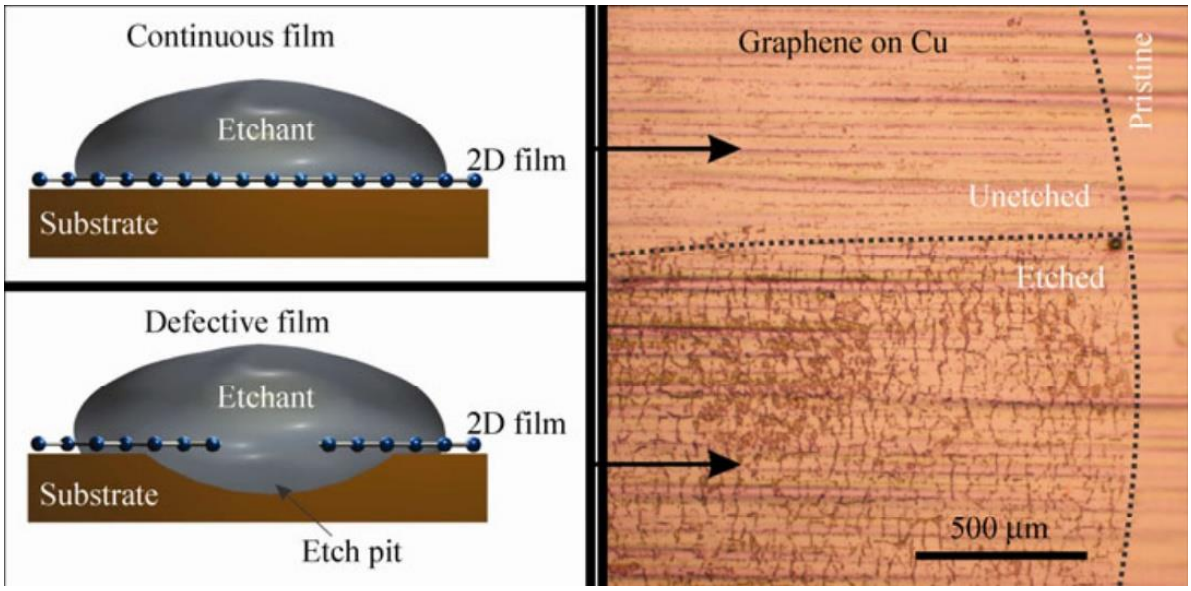

Figure 1.10 Water permeable origins etching through HCl solution. Reproduced from ref[10]

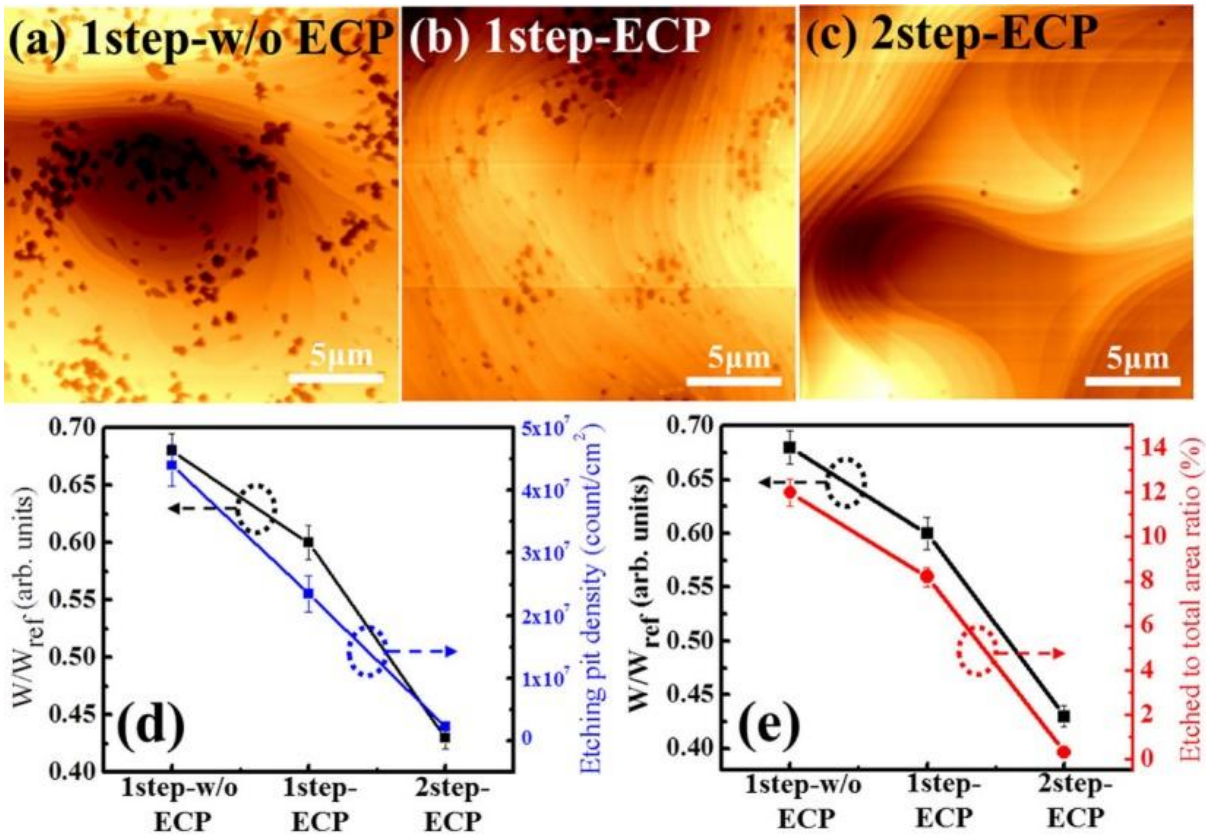

Figure 1.11 Correlation between WVTR and HCl etching area. Reproduced from ref[11]

CHAPTER 2

Oxygen radicals permeation through atomic structural defects of graphene

2.1 Graphene intrinsic defects distribution

Many researchers have been increasingly eager to synthesize graphene such as physical exfoliation, chemical exfoliation, thermal decomposition, unzipping carbon allotropes, and chemical vapor deposition. Among them, CVD can grow large-area, good quality, mass-producible and uniform graphene through activation and subsequent chemical reaction of gaseous reactants on transition metals such as Pt, Ni, Rb, Fe, and Cu[22]. Especially, copper that grows a uniform monolayer of graphene has attracted researchers' attentions as a graphene growth substrate involving surface reaction growth with low carbon solubility.

Differently with bulk materials, the graphene of two-dimensional material has reduced dimensionality of defects as point defects, line defects and grain boundaries during CVD graphene growth because of the second law of thermodynamics. In addition, graphene wrinkles are formed on the metal substrate due to the difference in thermal expansion coefficient during the cooling process after high temperature growth with weak adhesion energy to substrate for reducing compressive strain energy. These diverse intrinsic defects and deformations undermine primary properties of graphene such as chemical stability, mechanical property, electronic property, and impermeability by breaking stable sp_2 hybridized bonding and occurring tears.

It is important to find various intrinsic defects, tears and deformations of graphene in terms of optimizing graphene growth. The deformation of graphene as wrinkles can be observed by SEM system or OM after transfer because of difference of thickness. However, it is hard to estimate the distribution of intrinsic defects on as-grown CVD graphene because of their atomic sized distortion although their existence can be confirmed by TEM, STM, or Raman spectroscopy. Many researchers have been devoted to developing methods to find the distribution of defects, as grain sizes, nucleation sites, inter-granular grain boundaries, and intra-granular grain boundaries to optimize graphene growth conditions through polarized optical microscopy after liquid crystal coating, UV treatment with water, and metal deposition from atomic metal deposition.

Here, we examined selective oxygen permeation through atomic structural defects in CVD-grown graphene/copper composites measured by optical and electron microscopies. Using an simple air oxidation of graphene coated copper foils with heating of 200 °C, we developed a simple and large area characterization tool to visualize intrinsic graphene defects induced by different origins such as nucleation sites, inter grain boundaries and intra grain boundaries from CVD-grown graphene. This tool can be applied to observe the existence and distribution of intrinsic defects including properties of large area graphene. The oxidation conduct of copper can vary with the disorder of graphene structures in

CVD-grown graphene according to sources of various graphene intrinsic defects such as growth condition, crystallographic orientations of copper substrates and deformation of graphene during cooling. From the experimental and computational experiments, we found that oxygen atoms were dissociated from the water vapor of air are main origins oxidizing copper surface under graphene and that selective oxygen permeation occurs at stone–wales defects into graphene membrane promoted by other accumulated oxygen atoms as catalyst. Finally, we suggest the mechanism of underlying copper oxidation through selective permeation of oxygen atoms for an atomically thin CVD-grown graphene membrane.

2.2 Experimental Methods

Graphene synthesis

A conventional thermal CVD equipment was utilized to grow graphene on copper foils (99.8% purity, 25-μm) that were cut into 4 × 3 cm^2. The foils were rinsed with acetone followed by isopropyl alcohol (IPA) to eliminate surface organic matters. After organic matters cleaning, those went through a process of electropolishing in 85 % w/w phosphoric acid for 15min to eliminate the impurities of copper surface and then they were washed in fresh water followed by IPA for eliminating phosphoric acid residue. The Cu foils were put into a 4-inch quartz tube and the chamber was evacuated to ~3mTorr after the cleaning process. After evacuation, the temperature was increased to 1000–1050 °C with H_2 gas (5 sccm) flow maintaining evacuation of chamber. After the copper foils were annealed for 30min, the graphene was grown with CH_4 gas (10 sccm) for 30 min, and then cooling chamber with H_2 gas and CH_4 gas for full growth and without gas for partial growth.

Oxidation method

As-grown graphene/Copper composites were placed on Hot plate with 200 ºC for 30min~24 hr. The oxidation method was progressed in open system with hot water and oxygen for high moisture oxidation and in close system with water and evacuation for water vapor oxidation.

Graphene transfer

Graphene/copper foil composites were coated with 5 wt. % poly(methyl methacrylate) (PMMA) as supporting layer by spin coating of 3000 revolutions per minute for 60 sec and annealed at 130 ºC for 10 min. After PMMA coating, the graphene of copper foils backside was eliminated with O_2 plasma for 30 min and the copper foils were etched with 0.1 M ammonium persulfate with floating those composites. After etching process, the PMMA/graphene layers are rinsed by floating on fresh deionized water three times and scooped on SiO_2/Si substrates. PMMA layers is eliminated with acetone after mild dry(50 ºC for 30 min) and hard dry(130 ºC for 30 min).

Characterization

Raman spectroscopy and mapping data were gained with a WiTec Alpha 300R M-Raman which controlled the stage along x-y axis and have a 532 nm excitation source. The laser had a 640 nm spot size with a x50 objective lens (numerical aperture: 0.5). The measurement was proceeded with ~1 mW of laser power at the surface for preventing laser-induced thermal damage and effects. The data of Raman spectra and mapping were analyzed by the WiTec Project 2.10 provided from WiTec.

Electron-backscatter diffraction (EBSD) measurement was proceeded for analyzing the crystallographic orientations of the copper foils during CVD graphene growth with AMETEK EBSD

equipment installed in a FEI Quanta 3D FEG SEM. The condition of measurements was set with the probe current, the incident angle, and the accelerating voltage being maintained at 16 nA, 70º, and 15 kV. The EBSD mapping was proceeded with a 0.25 μm steps and the data of EBSD mapping were analyzed through the TSL OIM Analysis 6 software for getting mapping images of inverse pole figures of the copper crystallographic orientation.

X-ray photoelectron spectroscopy (XPS) measurement was controlled with a K-alpha spectrometer produced from Thermo Fisher with X-ray of 72 W-power using a aluminum Kα excitation source. The X-ray has ~400 μm beam spot size and the electron was accelerated to 50 eV during electron analysis. The measurement was proceeded with ultra-high vacuum chamber less than ~7.5×10^{-10} Torr. We proceeded the Gaussian-Lorentzian curve fitting of XPS spectrum from high resolution O 1s line scan after performing a Shirley background correction[23] to gain the result of oxygen composition.

CVD-grown graphene was directly transferred[24] on gold TEM grid made from Quantifoil for high resolution plan-view transmission electron microscopy (HR-TEM). High resolution TEM images and the selective area electron diffraction (SAED) patterns were gained through an FEI Titan cube G2 60-300 using a monochromator and an corrector of image-aberration. The voltage for TEM was accelerated to 80kV for decreasing the direct beam damage to the measured samples consisted of graphene layer for the purpose of observing the graphene grain boundaries and measuring the grain size of graphene domains.

Density-functional theory (DFT) calculations were performed for predicting the inversion energy of an oxygen radical into a graphene membrane and the energy for the horizontal diffusion of oxygen and hydrogen radicals from unsaturated carbon atoms. We used Vienna AB-initio Simulation Package (VASP) based on the spin-polarized density functional theory[25, 26] for the calculations. In addition, the ultra-soft pseudo-potential, and local density approximation of Ceperley and Alder type[27, 28] was used for the calculations. In a plane-wave basis set, the wavefunctions electrons were expanded to 500 eV as cutoff energy. Until forces on ions became less than 0.01 eV $Å^{-1}$ the calculations were collected. The Monkhorst-Pack k-point grid was set to $5\times5\times1$[29] for modeling Brillouin zone. In addition, we employed a 6 by 6 structure consisting of 72 carbon atoms for a free-standing graphene and a 4 by 4 graphene layer (32 carbon atoms) and 3 layers of Cu(111) slab (48 Cu atoms) virtualizing a graphene grown on a copper substrate for the penetration calculations. Furthermore, we employed the mono vacancy defects by eliminating on carbon atom from above structures for the diffusion simulations. The minimum energy for predicting pathway of oxygen penetration and oxygen diffusion on graphene surface was calculated by the nudged elastic band method (NEB)[29].

2.3 Visualizing of structural defects on Gr/Cu through selective oxygen penetration

Graphene was grown on Cu foils having the thickness of 25 μm with the chamber was annealed to temperatures of ~1000 °C in chamber using CH_4 and H_2 gases. The as-grown graphene had enough good quality ensured from structural and optoelectronic measurements (Figure 2.1).

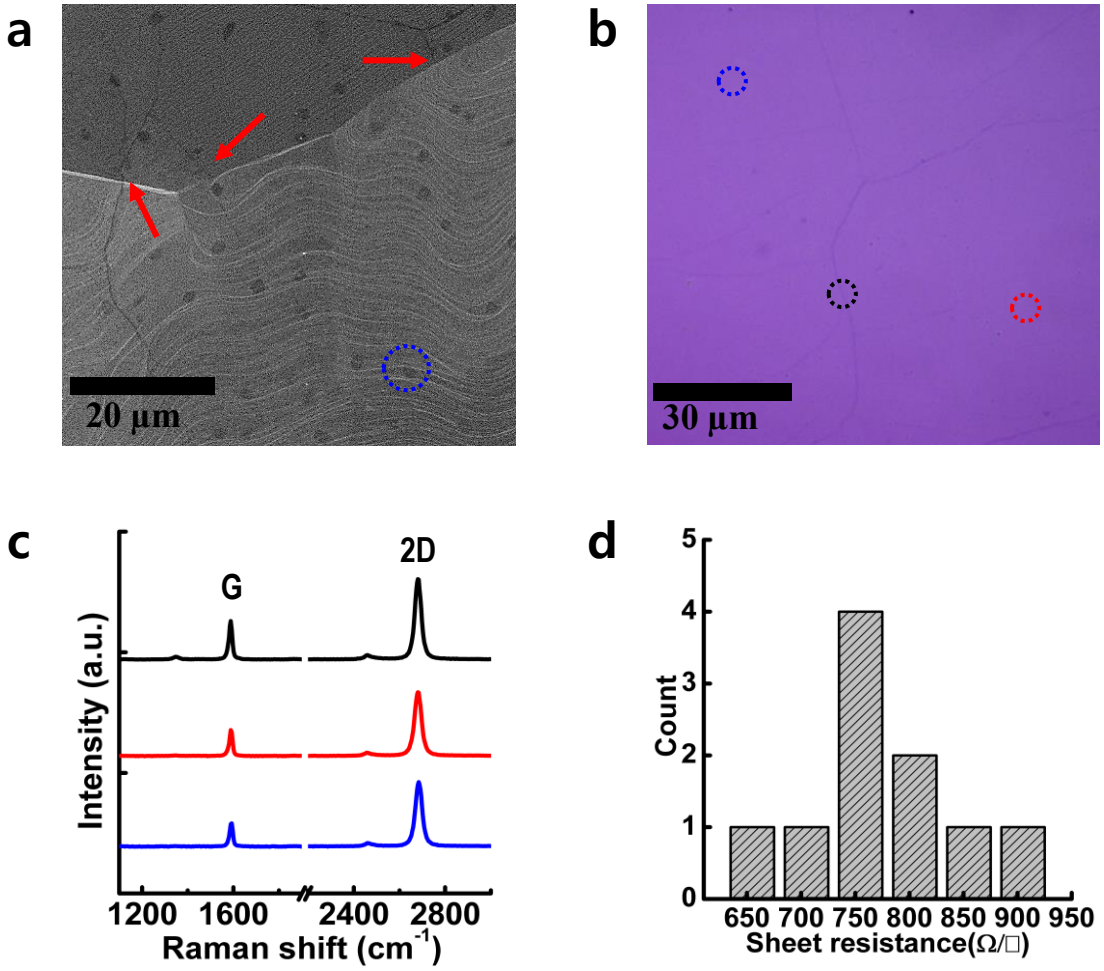

Figure 2.1 (**a**) SEM image of CVD grown graphene on copper foil. Blue circle indicates multilayer graphene flake and red arrows show wrinkles crossed the copper grain boundaries. (**b**) OM image of the graphene layer transferred on silicon oxide substrate (**c**) Raman spectra taken on black, red, and blue-dotted circle in (**b**), respectively. (**d**) Distribution of sheet resistance of graphene layer on silicon oxide substrate measured by Van der Pauw method.

The oxidation was proceeded by placing the as-grown graphene/copper composites on a hot plate. Typical images measured by optical microscopy (OM), which is the graphene/copper composites annealed at ~200 °C in air for 30, 60, 90, and 120min were showed in Figure 2.2. Oxidation features shaped with dots (marked by red arrows) began to occurrence precisely and additional oxidation features shaped with a polygon shape consisted of lines (marked by blue arrows) also occurred, as the oxidation times were expanded to longer than 30 and 90min, respectively. Interestingly, oxidized dots were mainly distributed at center of domains on the large area sample surface and the oxidation features were precisely developed as increase of annealing time. The scanning electron microscopy images with high resolution of the as-grown sample after 120min of annealing (Figure 2.3) shows the presence of dot features, line features, copper step bunch, and graphene wrinkles. Especially, the oxidation features were formed as globular-shaped nanoparticles and were protruded out from the smooth copper surface in high magnification images. However, other surfaces maintained their unoxidized flatness. Furthermore, we investigated the composition ratio and existence of other impurities in the oxidized graphene/copper composites using energy dispersive X-ray spectroscopy (EDS). Two substantial Cu peaks on the surface of samples with energies of 0.95 and 0.83 keV, which correlated to Cu Lα and Cu Lβ, respectively (Figure 2.4) from EDS spectrum of the samples. However, a weak oxygen signal with 0.53 keV energy was also measured only in the points of protruded features (denoted by red circle in Figure 2.3), indicating that the oxidation selectively occurred at the surface of samples along the dot and line features.

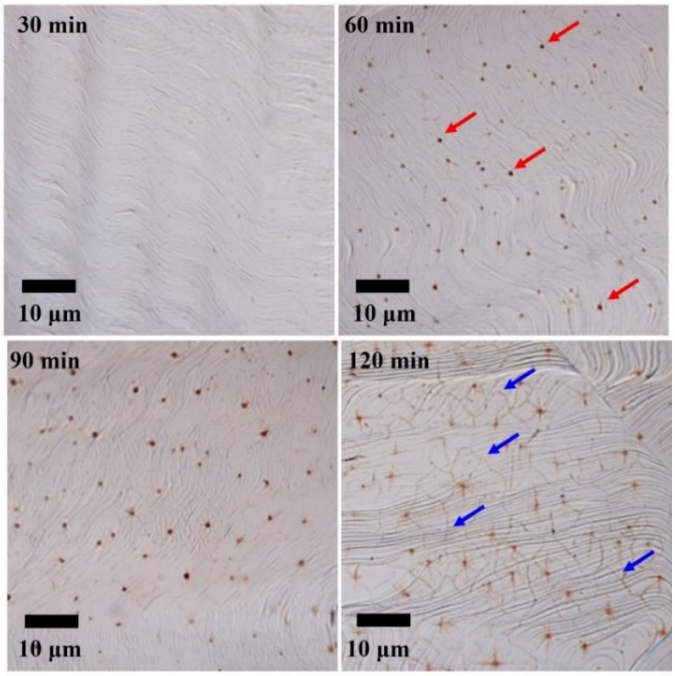

Figure 2.2 OM images of the as-grown graphene on Cu composite after oxidation for 30, 60, 90, 120 min

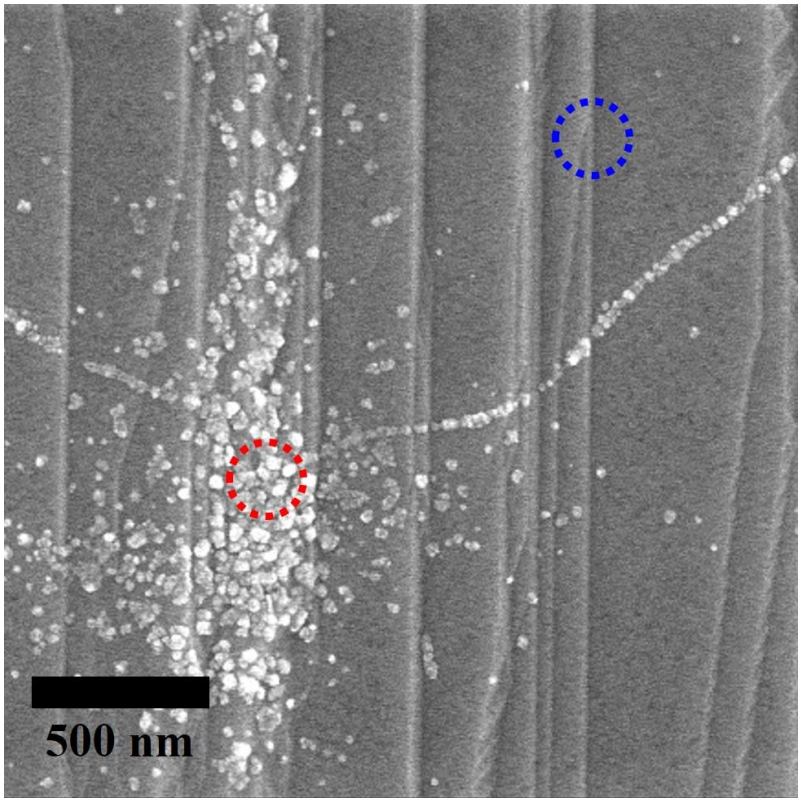

Figure 2.3 SEM image of the as-grown graphene on Cu composite after oxidation for 120 min in air

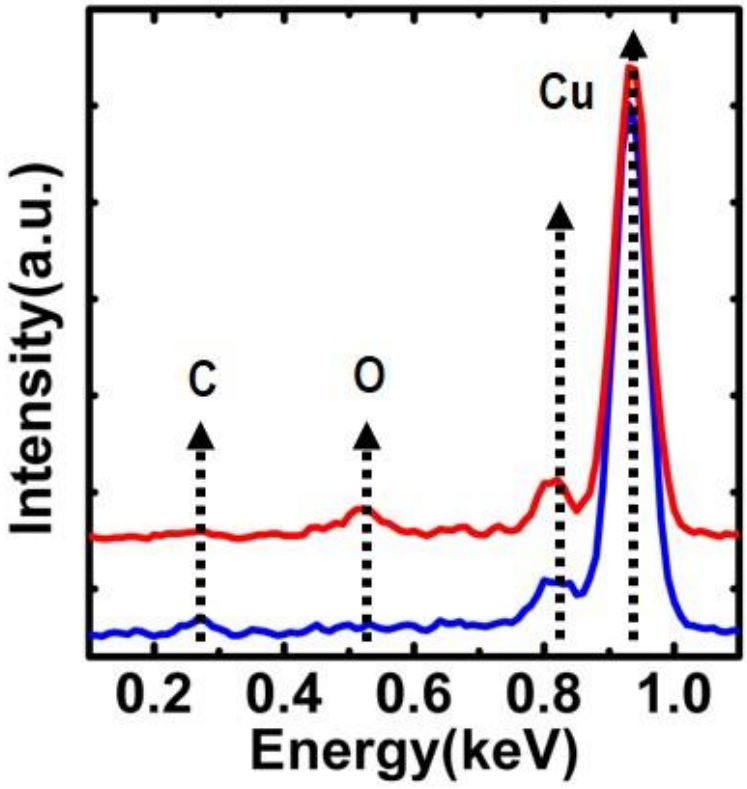

Figure 2.4 EDS spectra obtained from marked areas in Figure 2.3

The composition ratios in the samples with Ar^+ ion etching were also investigated by XPS paired to

confirm the origins of oxygen. In the high resolution C 1s line-scan spectra, the graphene, which had sp^2-hybridized carbon peak at ~284.4 eV, [23] gradually decreased and was shifted to lower energy as the Ar^+ ion etching time increased and then the peak was completely disappeared after 40 seconds etching (Figure 2.5). This phenomenon suggested that the graphene layer was completely etched away[30]. In Figure 2.6a, it was confirmed that the oxygen atoms were formed four different types based on their binding energy as hydroxyl group at 533.3 eV (4.7 at% of oxygen atoms), Cu_2O/CuO compounds at 530.3 eV (8.1 at% of oxygen atoms), carbonyl groups at 531.4 eV (67.6 at% of oxygen atoms), and carboxyl groups at 529.5 eV (19.6 at% of oxygen atoms) through the high resolution O 1s line-scan spectrum. Furthermore, the compounds of carbon and oxygen were perfectly eliminated after 10 s of etching ,but the peak at ~530 eV meaning the Cu_2O/CuO phase[31] was consistently observed for up to 40 s of etching in figure 2.6a. This was contrast to the case without oxidation features in Figure 2.5. From XPS studies, the protruded features are a distinct characteristic of being selectively oxidized copper surface under graphene after the oxidation method. In addition, the area of the Cu_2O/CuO peak considerably expanded as annealing time was increased from 60 to 120min at 200 °C, as shown in Figure 2.6b. From these studies, we can confirm that the oxidation features were certainly the result of the Gr/Cu composites being oxidized by the oxygen atoms from air.

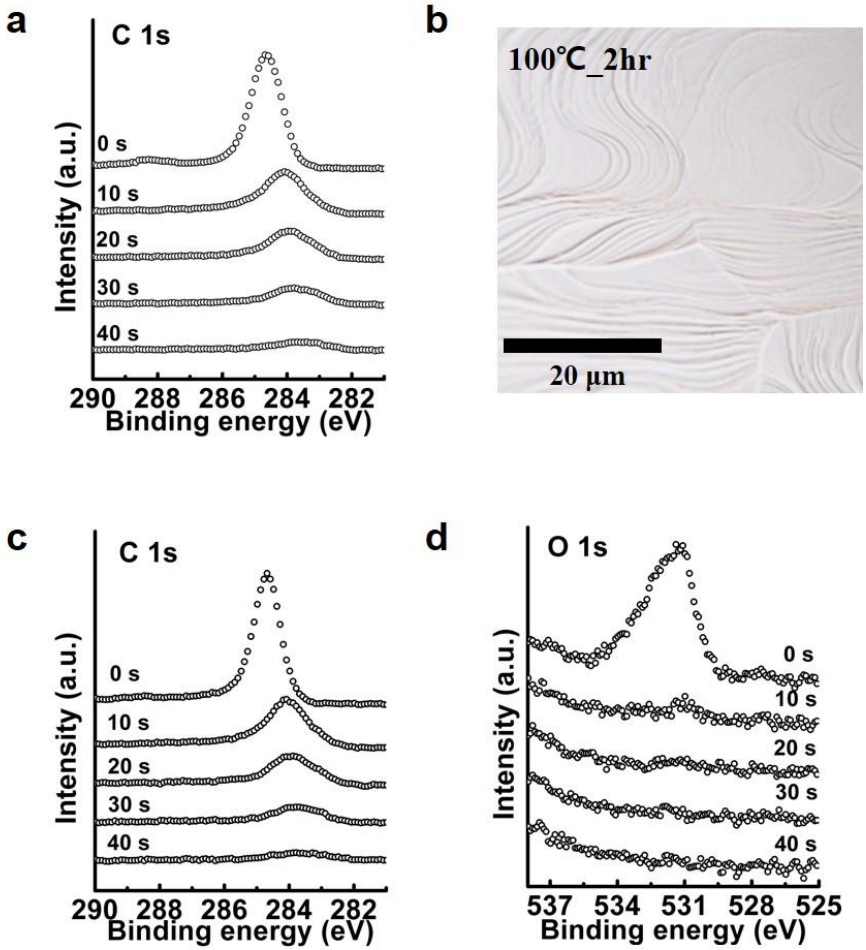

Figure 2.5 (**a**) High-resolution XPS C 1s scans of the as grown graphene composites after air oxidation at 200 ºC for 2hr followed by the Ar^+ ions etching for 0~40 sec. (**b**) OM image of the as-grown graphene composites after air oxidation at 100 ºC for 2 hr and corresponding XPS C 1s (**c**) and O 1s (**d**) scans followed by the Ar^+ ions sputter

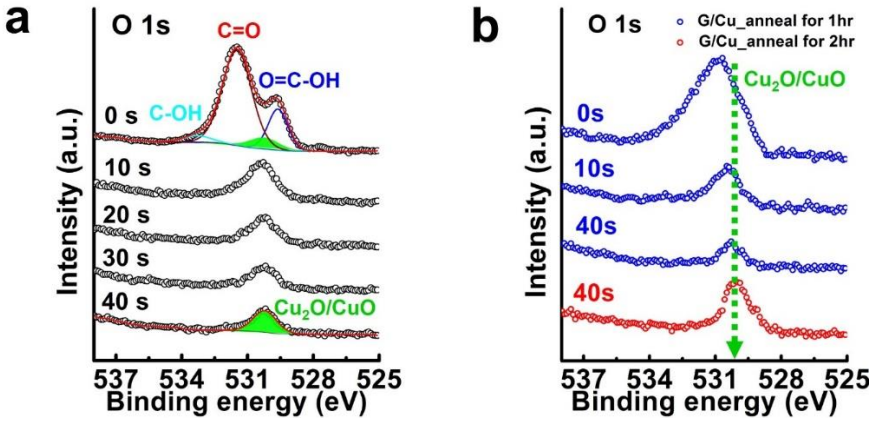

Figure 2.6 (**a**) Depth-profiling high resolution XPS O 1s scans of the as-grown graphene composites after air oxidation at 200 ºC for 120min (**b**) Comparison between high resolution O 1s peaks of the composites after oxidation for 60 min and 120 min in air

We proceeded a detailed analysis of the oxidation behaviors in the oxidized samples varying with the orientation of the copper grains. In particular, bare copper foils had dominantly the Cu (100) orientation (91%), and it was maintained after annealing copper foils (74%). Representative images of SEM and EBSD mapping are shown in Figure 2.7a, b that continuous graphene films after the oxidation method for 60min grown on Cu(100) and Cu(111) orientation, respectively. The major shapes of the granular oxidation features were related to those of the short time grown graphene islands on various copper orientations in the insets of Figure 2.7a, b. Therefore, the oxidation features formed on the Cu(100) orientations were mainly a four-lobed shape having average length of ~5.5 μm in Figure 2.7a, on the other hand that on the Cu(111) orientations was a hexagonal shape having average length of ~2.8 μm in Figure 2.7b.

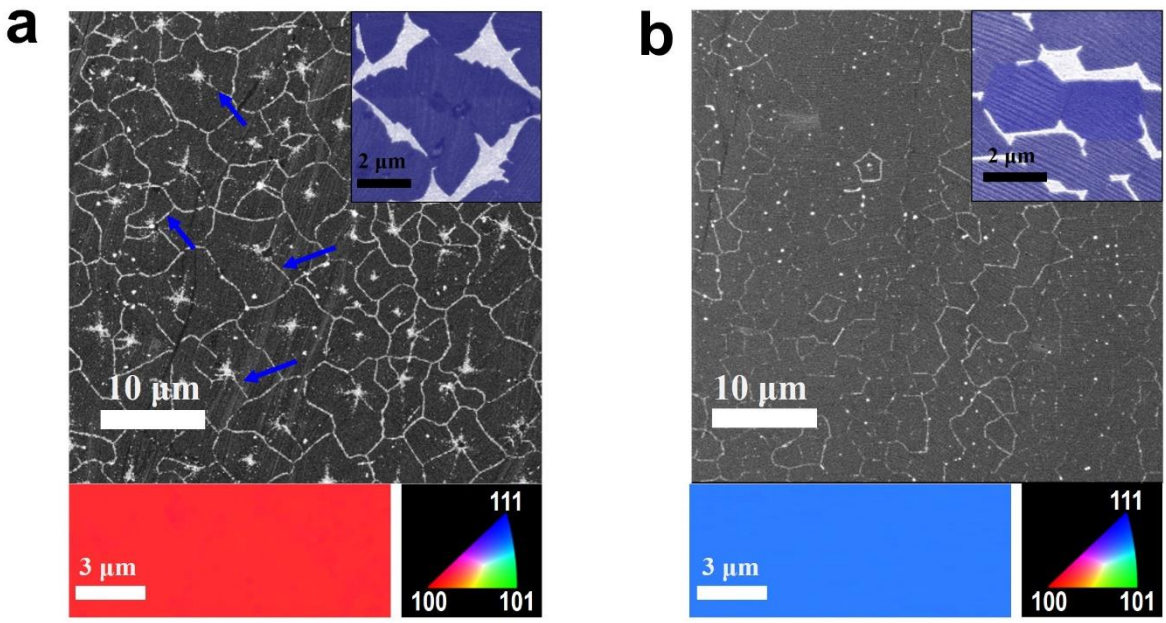

Figure 2.7 SEM and EBSD images of fully growth graphene grown on (**a**) Cu (100) and (**b**) Cu (111). The insets in (**a**) and (**b**) are the SEM images of graphene islands on copper with (100) and (111) orientation

In dark-field TEM observations, we also confirm that the average size of the granular oxidation features on various orientations was similar with the average size of the graphene domains grown on copper substrate as shown in bottom of Figure 2.8 and Figure 2.9. These results suggest that the oxidation method can estimate the inter grain boundaries of graphene. We also measured the size of graphene through the oxidation method to change growth conditions. The size of the graphene domains was decreased as increasing CH_4 flow rate provoked by having more nucleation sites[32, 33]. Through these experiments, the average length of the granular oxidation features decreased to ~3.1 μm when a methane

flow rate was increased to 50 sccm in top of Figure 2.8. It was interesting that the granular oxidation features of Cu (100) orientations were definitely observed as being thicker and more visible than those of Cu(111) orientations. Through this result, we can know that the copper orientation affect the impermeability of graphene to air oxidation and that Cu (111) orientations have advantages for growing the oxidation resistant graphene membranes having a higher degree of atomic stitching between the graphene islands[5, 34]. We sometimes found that intra grain boundaries within graphene domains on the Cu (100) orientations was oxidized in blue arrows of Figure 2.7a. The intra grain boundaries were the nature forming the multi-domain in the CVD-grown graphene islands[4]. The intra grain boundaries on the Cu (100) orientations can be completely detected with oxidation method for large area surface of samples when the annealing time was increased to 240min in blue circles of Figure 2.10. The results mean that intra grain boundaries in graphene islands are more impermeable to air oxidation than inter grain boundaries between graphene islands.

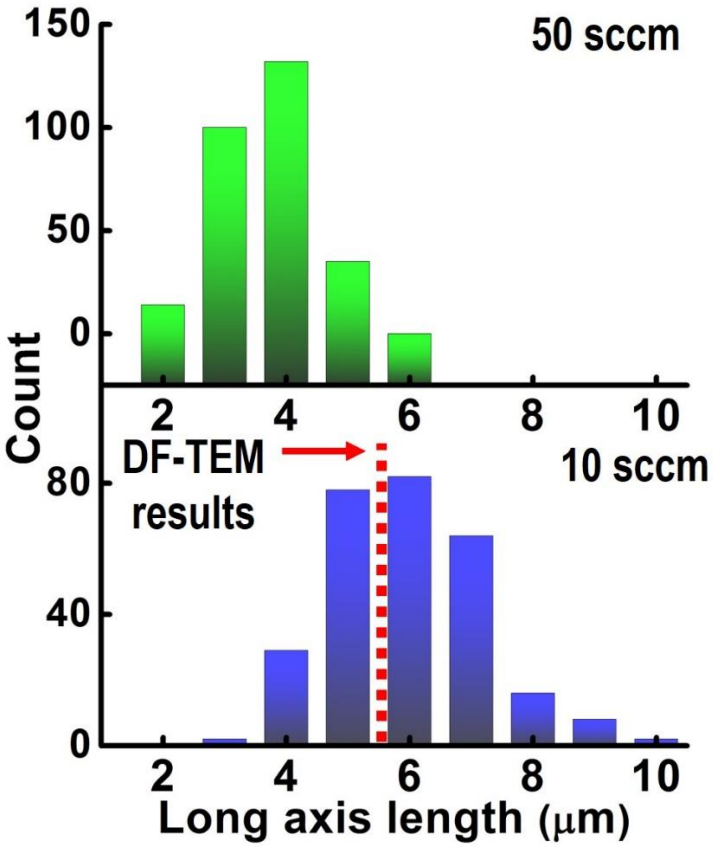

Figure 2.8 Change in the average length of the granular graphene grains developed on the oxidized graphene/copper composites measured by TEM and oxidation method as change of CH_4 flow rate

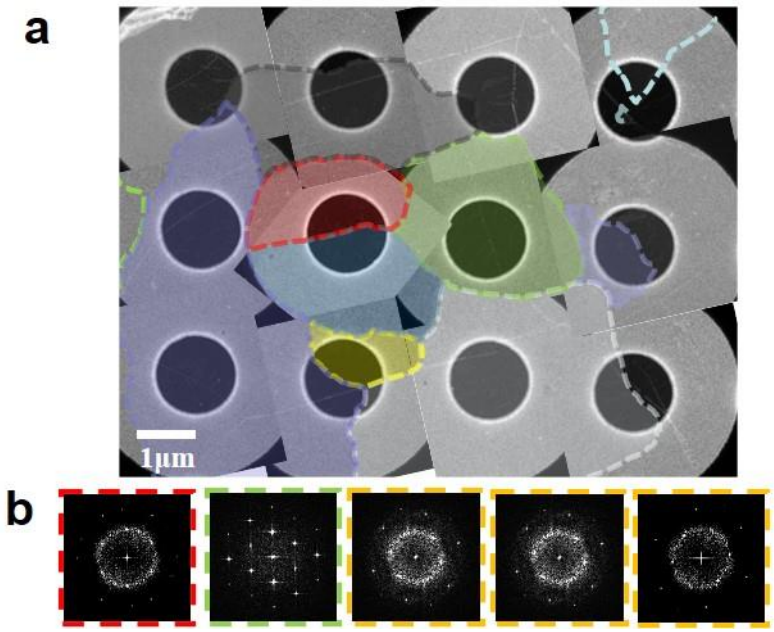

Figure 2.9 (**a**) A plan-view TEM image of a graphene grown on copper after direct transfer onto a TEM grid. The imaginary colored areas emphasize the different lattice structures of the graphene domains. (**b**) FFT patterns of the colored areas in (a)

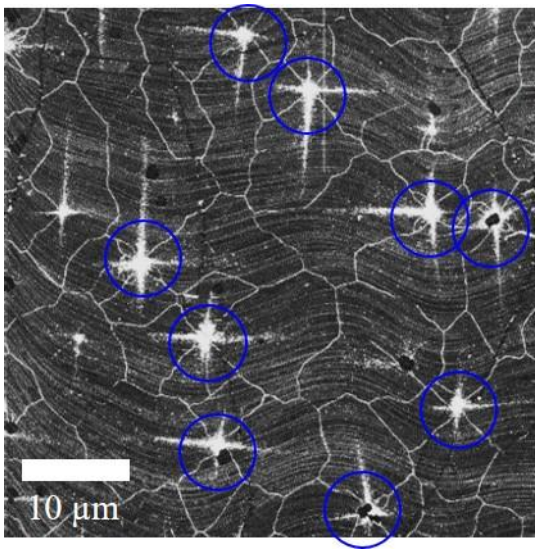

Figure 2.10 SEM image of the as-grown graphene composites after air oxidation at 200 ºC for 240 min. Blue circles indicate regions clearly showing the line oxidation features originated from intra-granular GBs

2.4 Oxidation conducts of Cu into intrinsic defects of graphene

We proceeded short time growth for synthesizing graphene islands which form isolated graphene film on copper substrates. There are SEM images of a not merged graphene island on Cu (100) orientations before and after oxidation method in Figure 2.11a, b. The oxidation features of dots were detected at the center in Figure 2.11b and the area out of graphene island. We find that the protruded oxide particles of graphene nucleation sites were similar with those of bare having the size from ~30 to ~50 nm through high resolution SEM images in Figure 2.1. Many researchers suggest that the copper oxide formed on copper with low temperature oxidation nether 300 °C commonly have small particles composed of thin cupric oxide layer, thick cuprous oxide layer, and oxygen containing copper bulk[35-37], and the size of copper particles was increased with solving the oxygen in copper bulk transforming to CuO/Cu_2O and being exerted with compressive stresses during the oxidation, which protruded the formation of small oxide crystals.

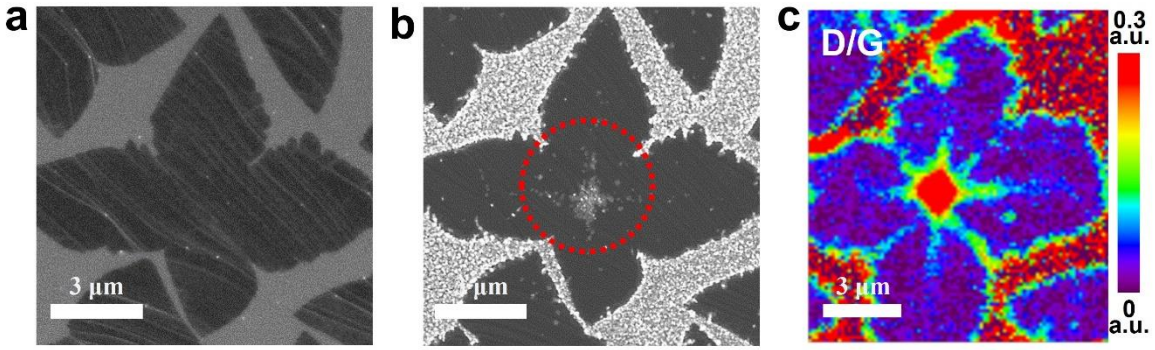

Figure 2.11 SEM images of graphene island grown on a copper for 1 min (**a**) before and (**b**) after oxidation. (**c**) Raman D/G mapping image of the partially grown graphene transferred onto silicon oxide substrate

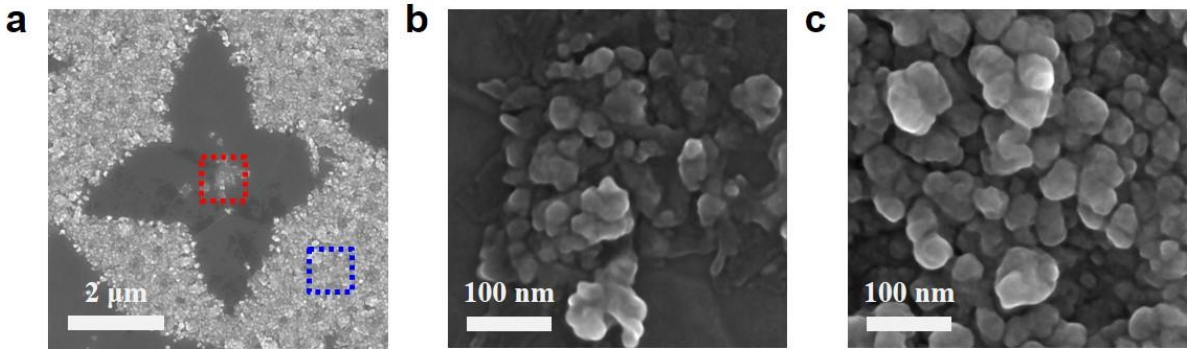

Figure 2.12 (**a**) A low-magnification SEM image of a Gr island grown on copper at 1000 °C for 1 min after air oxidation at 200 °C for 70 min. (b,c) High magnification SEM images of (**b**) the red-dotted and (**c**) blue-dotted square in (**a**).

We can know that the nucleation sites oxidation features were combined with cross-shaped feature and rhombus-shaped feature through confined nucleation sites oxidation experiments. For deeply studying the behaviors of nucleation sites oxidation, first, we transferred as-grown CVD graphene on silicon substrate without oxidation for Raman measurement. The representative Raman peaks of CVD-grown graphene were D, G, and 2D as value of 1351 cm^{-1}, 1588 cm^{-1} and 2685 cm^{-1}, respectively[38-40] as shown in Figure 2.11c, Figures 2.13 and 2.14. As shown in Figure 2.11c, there were two types of intrinsic defects at the center of CVD-grown graphene through D/G Raman mapping image. Almost area of graphene had, very small value of I_D/I_G intensity ratio below 0.05, but the value of that was high at the rhombus-shaped as 0.3 and cross-shaped as 0.2. We performed Raman mapping measurements for numerous graphene above 30 islands and confirmed that almost island grown on copper (100) had two defective features in the nucleation sites for all sizes of graphene islands grown as varying the conditions of growth in Figure 2.12. The I_D/I_G ratio detected from rhombus-shaped oxidation features was always higher than other defective sites such as edges of graphene islands and intra grain boundaries. This means that oxidation method is a facile tool for detecting the distribution of atomic structural defects of CVD-grown graphene as Raman spectroscopy. In addition, our discovery of nucleation sites defects through oxidation method suggests that there are still challenges for improving crystalline quality of graphene during occurrence of seeds and extension of graphene for large scaled and high quality CVD graphene.

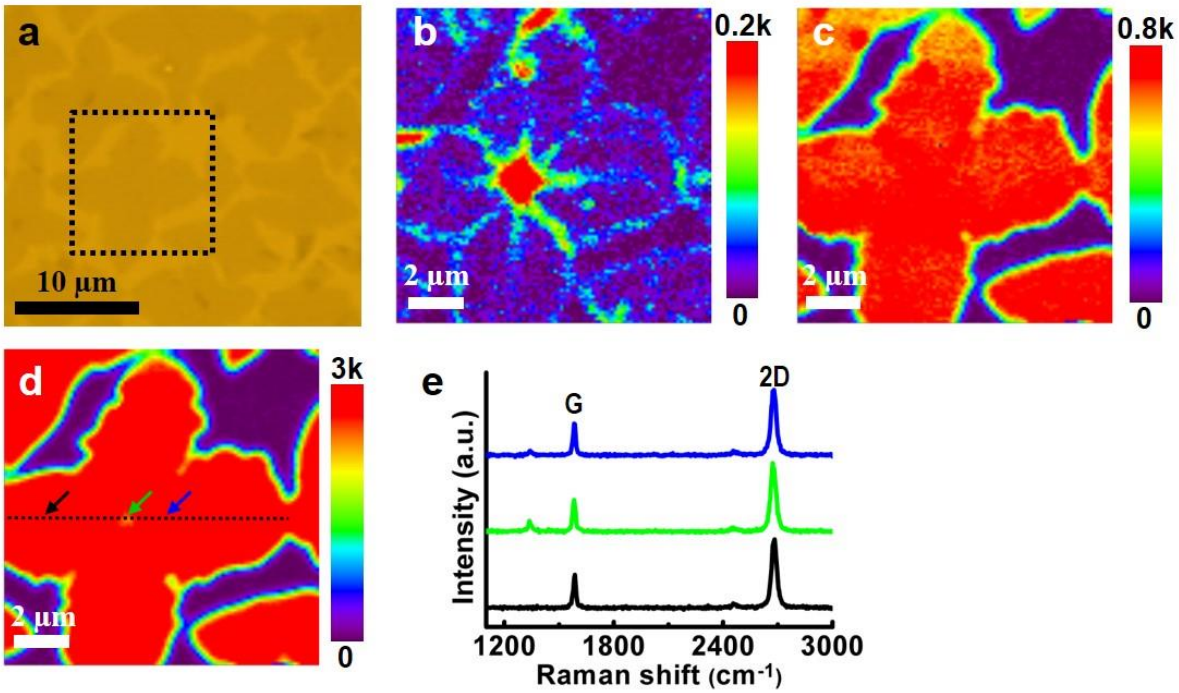

Figure 2.13 (**a**) An OM image of the graphene islands after transfer onto silicon oxide substrate. (b-d) Corresponding Raman mapping images of the D (**b**), G (**c**), and 2D band (**d**), respectively. (**e**) Raman single spectrum taken from colored arrows along the black dotted line in d.

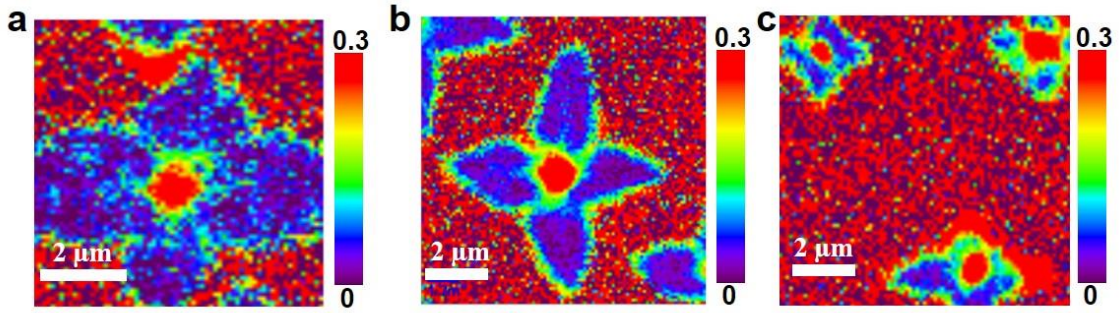

Figure 2.14 Raman maps of the D/G bands of graphene islands with the 4-lobe shape that were grown on Cu foils at 1000 °C for 30 sec (**a**), 15 sec (**b**), and 5 sec (**c**) and then transferred onto the silicon oxide substrate.

In Figure 2.15a–f there are EBSD mapping images gained from graphene islands with various crystallographic orientations of copper substrate. Although the Cu(100) orientation was dominant copper grains, in some area, the copper grain had other orientations such as Cu(111), Cu(101), and high index orientations in Figure 2.15a. The nucleation sites oxidation always occurred at center of 0graphene islands for Cu (100) and (101) orientations in Figure 2.15b–d, but there were no nucleation sites oxidation features on the Cu (111) orientations in Figure 2.15e. This phenomenon was clearly observed at the copper grain boundary between (100) and (111) in Figure 2.15f. In graphene islands formed on copper grain boundary (100) and (111), the nucleation sites oxidation features were detected at Cu (100) orientations, but the oxidation features were disappeared at Cu(111) orientation as shown in red dotted line of Figure 2.15f. From these results, we can know that the crystallin quality of graphene nucleation sites was better on Cu (111) orientations than Cu (100), Cu (101) and high-index orientations. We also proceeded Raman mapping of partially grown graphene on Cu(111) orientations to confirm our results. Three was no nucleation sites defects on Cu (111) orientations in Figure 2.15g with neglectable D/G ratio. Through these experiments, we confirm that the underlying copper orientations in CVD growth affect the quality of nucleation sites of graphene islands. Furthermore, Cu (111) orientation substrates are necessary for synthesizing high quality graphene.

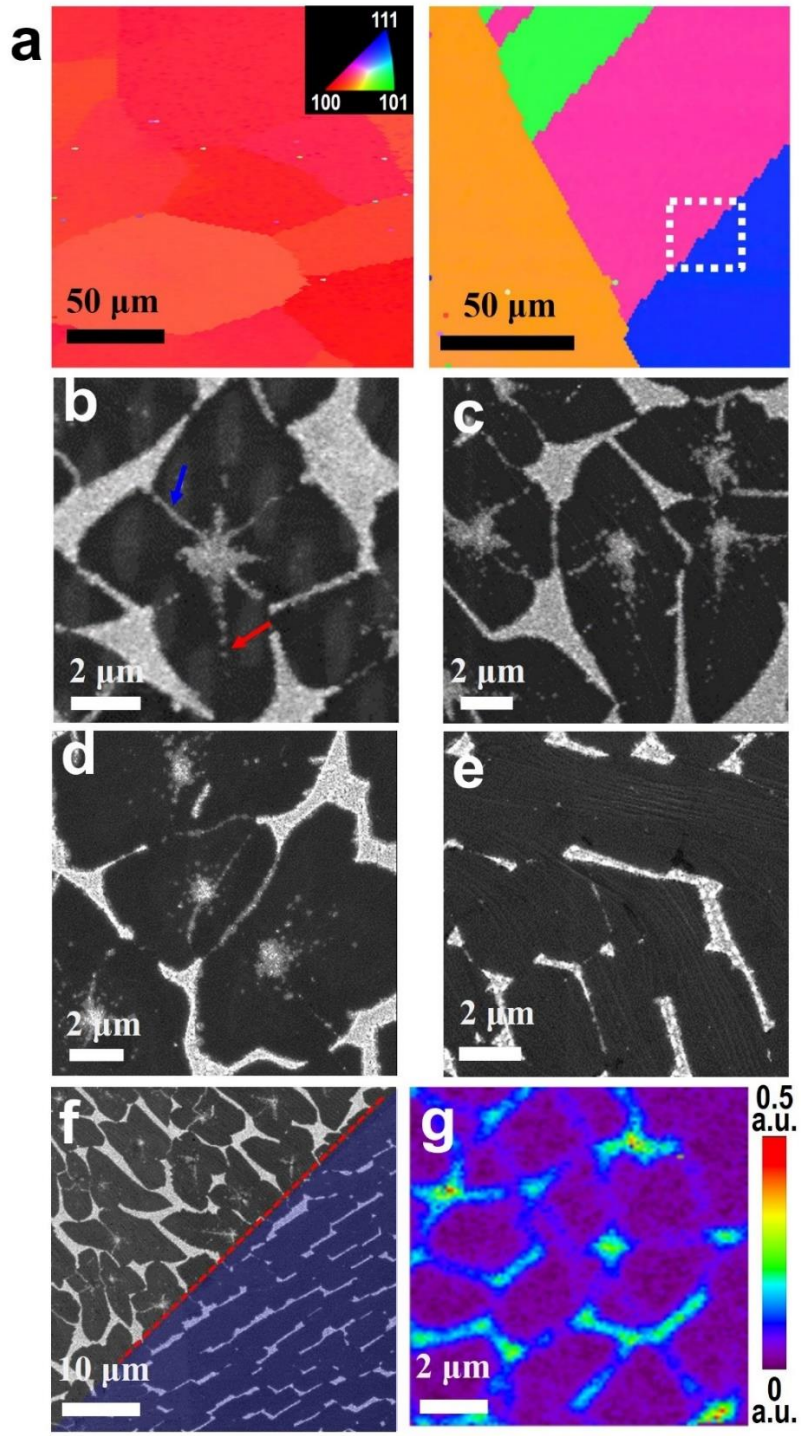

Figure 2.15 (**a**) EBSD images with mapping of copper foil after partially graphene growth at 1000 ºC. The EBSD data show that Cu (100) are abundant area (left) and, in some regions, having orientations of (111), (101), and high-index orientations (right). (b-f) SEM images of partially grown graphene diverse orientation of (**b**, **c**) (100), (**d**) (101), (**e**) (111), and (**f**) the boundary between (100) and (111) after oxidation. (**g**) Raman D/G mapping image of the partially grown graphene on Cu (111) after transfer

The cross-shaped oxidation features centered at nucleation sites were also evident characteristics of CVD grown graphene on Cu (100) orientations being separated from the intra and inter grain boundaries in blue arrow of Figure 2.15b. We predicted that the cross-shaped oxidation features were related to the kinetics of graphene growth on the copper substrate, because the cross-shaped oxidation features aligned to lobes of graphene islands in red arrow of Figure 2.15b and had different lengths along the length of lobes within same samples in Figure 2.15c. Therefore, we performed the control of graphene islands growth rate such as temperature and gas flow to understanding the behavior of cross-shaped nucleation sites oxidation. When we increased the growth temperature to 1050 °C, the cross-shaped oxidation features expanded to edge of graphene islands as shown in Figure 2.16a. However, we observed that the cross-shaped oxidation features remained as dot as nucleation seeds oxidation by reducing the growth rate by increasing the H_2 gas flow rate to 20 sccm in Figure 2.16b and decreasing the CH_4 gas flow rate 2 sccm in Figure 2.16c. We can know that the graphene islands with a high growth rate have long nucleation sites defects as various point defects, but the reducing of graphene growth rate at early stage can enhance the quality of graphene nucleation sites.

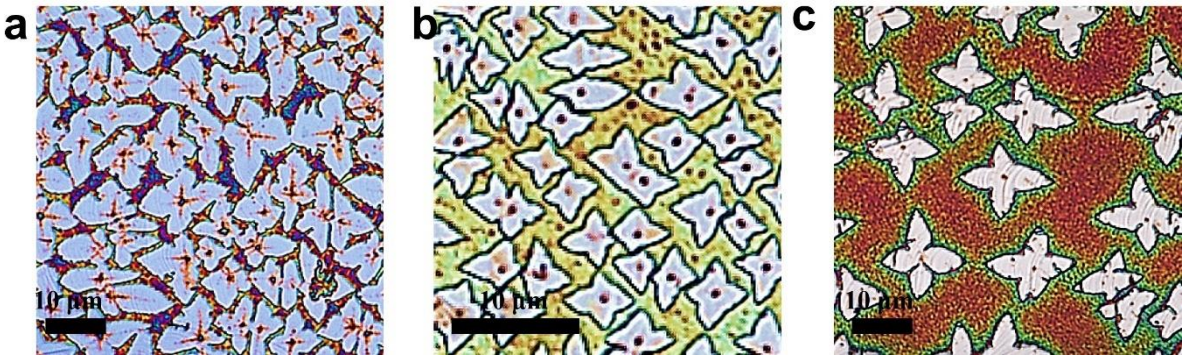

Figure 2.16 OM images of the partially grown graphene on Cu (100) after oxidation method under various growth rate of graphene. Graphene were partially grown (**a**) at 1050 °C for 30 sec with CH_4 of 10 sccm and H_2 of 5 sccm, (**b**) at 1000 °C for 30 sec with CH_4 of 10 sccm and H_2 of 20 sccm, and (**c**) at 1,000 °C for 3min with CH_4 of 2 sccm and H_2 of 5 sccm

As shown in Figure 2.17a, we also observe that the nucleation sites oxidation did not occur at center of graphene islands. We took several images of graphene islands above 100 using high resolution SEM and observed that the nucleation sites oxidation did not occur at multilayer area of graphene nucleation. Because the multilayer graphene reduce the reflection of secondary electrons, multilayer graphene has

darker image in the SEM than monolayer graphene[41] as shown in inset of Figure 2.17a. Through these results we can know that multilayer area protecting copper substrates from air oxidation in blue arrows of Figure 2.17b. The ability to protect the copper substrates from oxidation was also confirmed for 240 min oxidation in blue arrows of Figure 2.17c. Although the nucleation sites of the graphene islands were still defective being identified by the Raman mapping in Figure 2.18a–c, the oxidation did not occur at the nucleation sites with multilayer graphene area. Because the oxygen molecules had very high diffusivity between graphitic layers[42], these results resolutely suggest that the oxygen molecule in air was not a major origin of the underlying copper oxidation. In Figure 2.19 this phenomenon was also observed at not only multilayer graphene area but also wrinkles of graphene forming a kink of oxidation features from intra grain boundaries when the oxidation line features met the folded wrinkles of graphene. We can know that the multilayer stacking was formed by folding to decrease compressive stress was not oxidized after oxidation method being effectively resistant to oxidation.

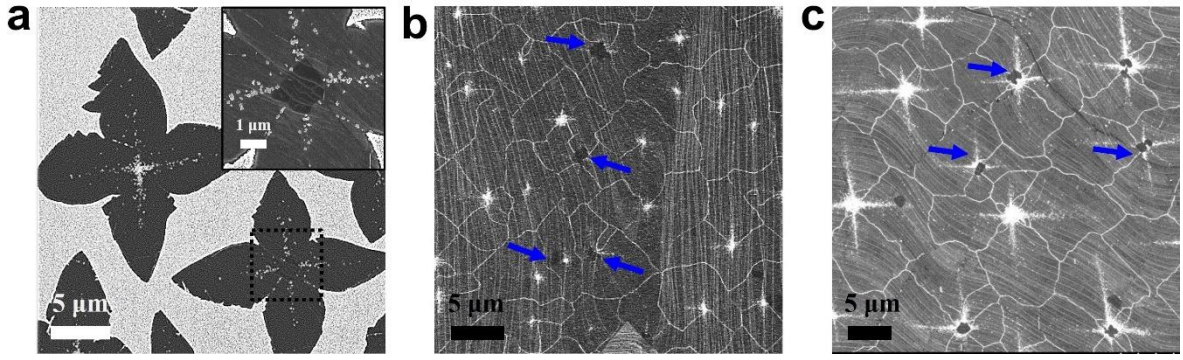

Figure 2.17 (**a**) SEM image of partially grown graphene on Cu (100) after oxidation. Inset indicates a highly magnified SEM image of in (a). SEM images of the as-grown graphene composites after oxidation for (**b**) 120 and (**c**) 240 min. Blue arrows indicate multilayer formed on nucleation center

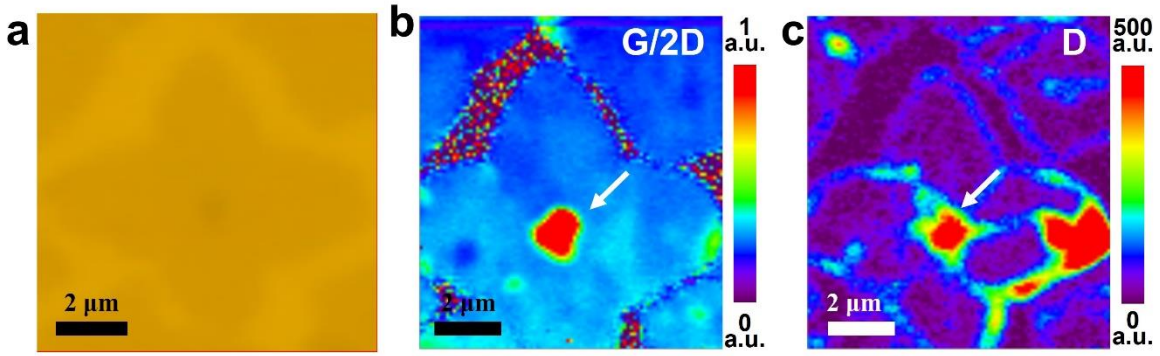

Figure 2.18 (**a**) OM image and Raman mapping images for G/2D and D of partially grown graphene having a multilayer, after transfer onto silicon oxide. White arrows indicate multilayer formed on nucleation center

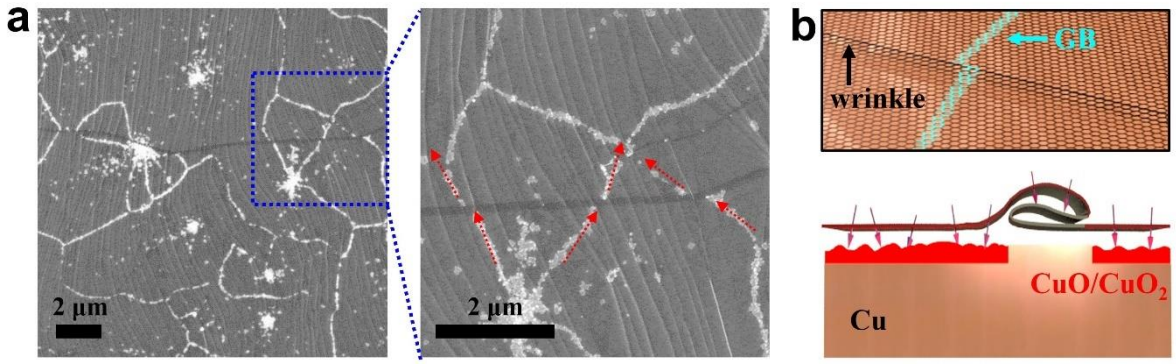

Figure 2.19 (**a**) SEM images of the graphene containing folded wrinkles after oxidation. The right is a high magnified SEM image, and the red arrows indicate a kink of oxidation features formed on the wrinkle. (**b**) Scheme of the folded wrinkles in graphene acted as effective barrier film to air oxidation

2.5 Oxidation mechanism of Cu into defects of graphene

As shown in Figure 2.20a-e, we proceeded the various oxidation experiments in various oxidation environments at ~200°C to explore the origin of the selective oxygen permeation to copper substrate through graphene intrinsic defects. Interestingly, in the condition of vacuum and pure oxygen atmosphere with pressure of 150 Torr, the graphene/copper samples were not oxidized along intrinsic defects of graphene such as inter grain boundaries, intra grain boundaries, and nucleation sites of the graphene in Figure 2.20a and b, in contrast to air oxidation in Figure 2.20c. We confirmed that oxygen molecules were not the major origin for oxidation of underlying copper substrate and that oxygen contained in bulk copper was also not a major origin released during vacuum annealing[23] from the controlled experiments. There are previous experimental and theoretical researches about the dissociation of oxygen molecules and water molecules on graphene with or without defects[43, 44]. According to the results, oxygen molecules has relatively high activation energy of dissociative reaction as 1.78 and 2.80 eV on ideal graphene layer and the grain boundaries of graphene. However, water molecules on a defective sites of graphene has low activation energy of dissociative reaction as monovacancy of 0.04 eV, divacancy of 0.35 eV or edge of 0.06 eV, being easily split to H radical and OH radical, even at RT. As shown in Figure 2.20d, we also proceeded oxidation experiments in a humid oxygen environment with relative humidity (RH) of 80% to investigate the role of water and found that the oxidation features with humid oxygen were considerably thick and distinctly obvious compared to ambient air with RH of 30-40% as shown in Figure 2.20c. Furthermore, as shown in Figure 2.20e, we proceeded the oxidation experiment in humid nitrogen atmosphere with RH of 50% to exclude other oxygen interference of samples. Similarly, the oxidation features occurred at underlying copper through graphene intrinsic defects and they were detected clearly by SEM and OM images as shown in Figure 2.21a, b after oxidation in a humid nitrogen atmosphere. We observed that the degree of forming oxidation features was considerably different with various gas ambient, as other phase transformation and thin film formation[45]. As expected, there were no oxidation features when the graphene/copper samples was oxidized in dry nitrogen atmosphere as shown in Figure 2.21c. Through this result, we could know that the water molecules in air were the major origin for selective oxidation permeation to copper substrate through graphene intrinsic defects.

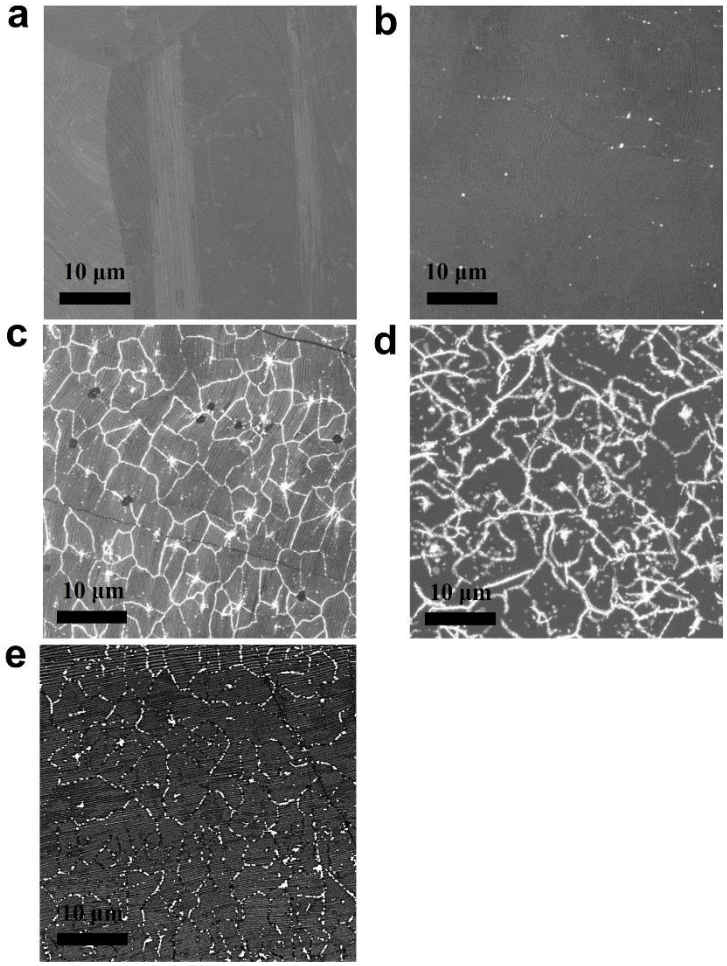

Figure 2.20 SEM images of as-grown graphene composites after air oxidation at 200 °C (**a**) for 120min under vacuum (**b**) for 120min in dry oxygen environment of 150 Torr, (**c**) for 120min in air (RH ≈ 30–40%), (**d**) for 60min in a humid oxygen environment (RH ≈ 80%), and (**e**) for 60min in a humid nitrogen environment (RH ≈ 50%).

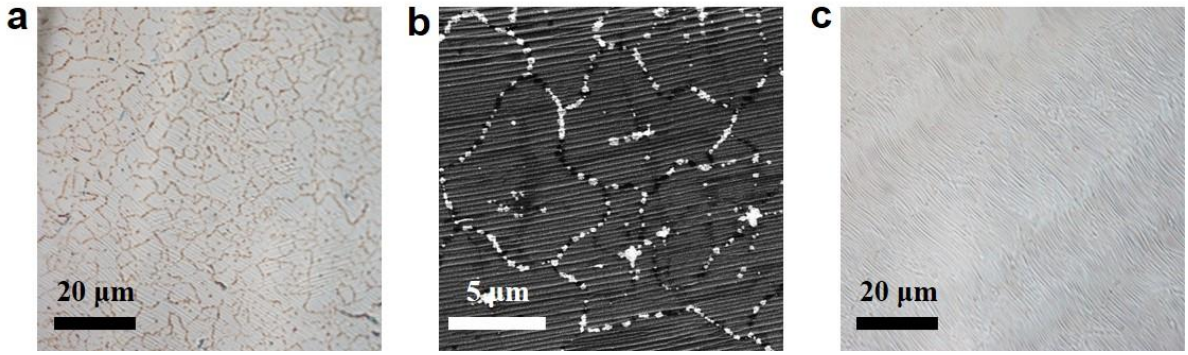

Figure 2.21 (a,b) Representative OM (a) and SEM (b) images of as-grown graphene composites after oxidation at 200 °C for 60 min in a wet-N_2 atmosphere (RH ≈50%). (c) A OM image of as-grown graphene composites after oxidation at ~200 °C for 60 min in a dry-N_2 atmosphere

As shown in Figure 2.22a, the XPS data was gained from as-grown graphene samples with various annealing condition as temperature was set to 100 and 200 °C and oxidation time was set to 60 and 120min in air including not annealed samples. The oxidation features of underlying copper were detected only in 200 °C oxidation samples by OM and SEM. In the 100 °C oxidation samples, there were no oxidation features. However, the XPS spectra of all of oxidation samples showed clear O 1s peaks as carbonyl group of 530 eV and hydroxyl group of 533 eV. In contrast to 100 °C oxidation composites, carboxyl groups were also detected in 200 °C oxidation composites which had oxidation features as shown in Figure 2.22b. This mean that the carboxyl groups are major byproducts formed on graphene after proceeding oxidation method demanding humid atmosphere. Therefore, we predict that the oxygen radicals decomposed from water molecules are main origins for selectively oxygen permeation through graphene intrinsic defects. For estimating disorder of water permeation defects, we measured many graphene domains with an aberration-corrected HR-TEM. It was hard to detect the vacancies or pores in graphene lattice. Instead, as shown in Figure 2.22c, the graphene grain boundaries consisted of pentagon and heptagon carbon rings in rotation as Stone Wales defects.

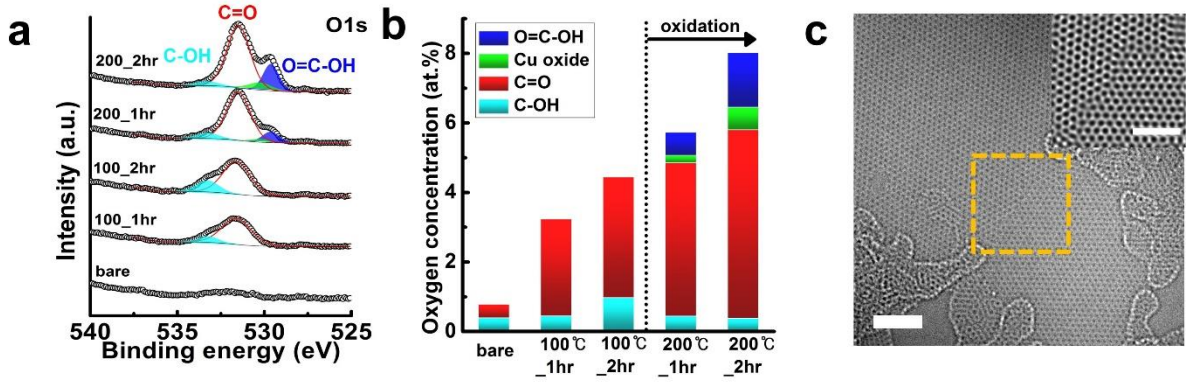

Figure 2.22 (**a**, **b**) A comparison between High resolution XPS O 1s scans and the chemical contents of as-grown graphene after air oxidation along oxidation temperature and time. (**c**) Plan-view highly resolved TEM image (scale bar=2 nm) of graphene after transfer onto a TEM grid. The inset (scale bar=0.5 nm) indicates an atomic-resolution image of a graphene grain boundary, marked by a yellow square

It is a main question to find mechanism of the underlying copper oxidation through SW defects of graphene grain boundaries without any vacancies. For finding the answer, we proceeded spin-polarized density functional theory calculations[25, 26] on the selective permeation of oxygen atoms through only graphene membrane and on effects of attached functional groups formed on graphene surface to explore the origin of the oxygen atom inversion to copper substrate. The activation energy for inversion was 2.46 eV for a single epoxide at the stone-wales defect. However, as shown in Table 3, various functional

groups as H, OH, or O atoms considerably diminished the barrier energy with attaching around the epoxide. When an additional O atom was attached to the epoxide at SW defects, the activation energy for inversion decreased to 0.31 eV, meaning the possibility of the selective oxygen permeation through the SW defect even in 200 ℃. For matching with experiments, we also proceeded the calculation of activation energy considering copper substrate effects. The activation energy for oxygen inversion through graphene with copper slab had higher as 0.7 eV than without copper slab as shown in Figure 2.23. However, the selective oxygen permeation through the stone-wales defect of graphene can still occur in 200 ℃. In addition, the difference of free energy after oxygen inversion through stone-wales defects was negative 0.1 eV, meaning that the reaction of oxygen inverse in epoxide was thermodynamically more stable in the graphene/copper structures. Furthermore, the oxygen atom of permeated epoxide with single bond will be decomposed with copper substrate considering the fact that a bond breaking energy of the carbon dioxide on Cu is ~1.0 eV[46], and the selective oxidation can occur at various intrinsic defects of graphene.

Functional group	Oxygen inversion barrier
without	2.461 eV
1 H	1.700 eV
2 H	1.573 eV
1 OH	1.484 eV
2 OH	1.502 eV
1 O	0.314 eV

Table 3 Calculated activation energy for inversion of an oxygen radical at stone-wales defect on graphene without substrate along facilitator molecules

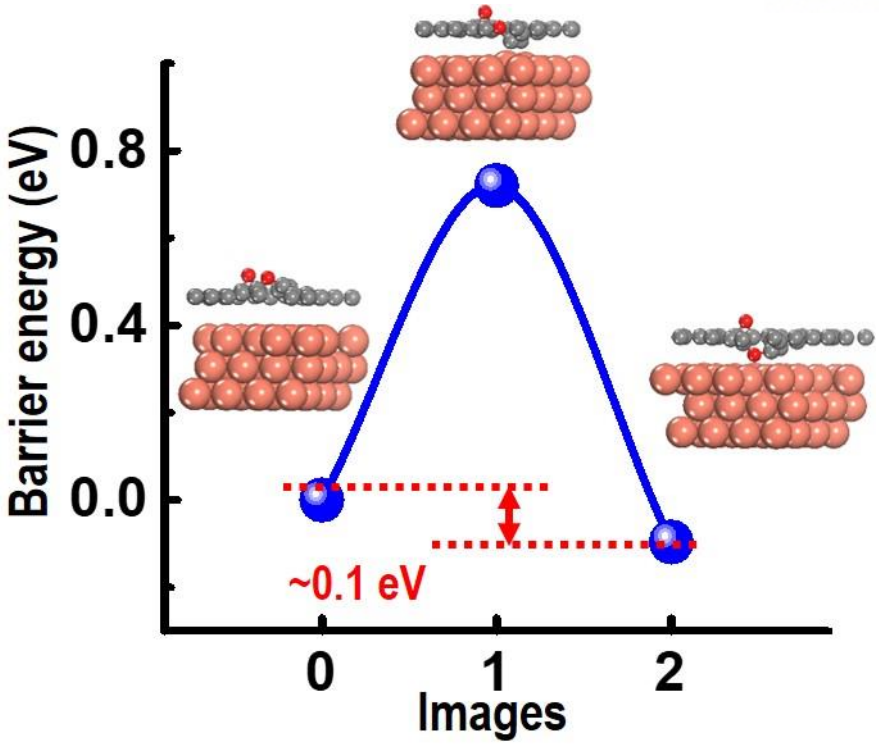

Figure 2.23 DFT calculation results about inversion barrier of the O atom on a Cu substrate.

It is needed to discuss the mechanism for production of oxygen radicals for selective penetration through graphene stone-wales defects. It is hard to directly dissociate the water molecules at SW defects because of high activation energy of 2.71 eV[44]. In place of that, we predicted other defects for dissociating water into oxygen radicals. Through previous experimental and theoretical researches, the nature of intrinsic defects of CVD grown graphene is always existent and set at ease, and they can be applied as catalysis for the dissociation of water molecules from air. The activation energy for dissociating water is very low with various intrinsic defects as edge of 0.06 eV, monovacancy of 0.04 eV and divacancy of 0.35 eV[43, 44]. As shown in figure 2.24, we also proceeded the spin-polarized DFT calculations on the water molecule dissociation at a graphene monovacancy. The water molecule is split into one oxygen atom and two hydrogen atoms on monovacancy, and both the each oxygen and hydrogen atoms can diffuse along graphene lattice with the activation energy of 1.9 eV. Although activation energy for diffusion of oxygen and hydrogen atoms along graphene lattice from the monovacancy are still high, it is more acceptable than the dissociation of water at SW defects having activation energy of 2.71 eV[44]. The monovacancy can act as catalyst for consistent decomposition of water after the dissociated oxygen and hydrogen atoms are diffused out from monovacancy repeating the dissociative reaction. Interestingly, we confirmed that the copper substrate could significantly reduce the diffusion barrier for oxygen and hydrogen radicals into neighboring carbon rings. In addition, the activation energy of oxygen radicals diffusion to ideal graphene is sufficiently low below 1 eV

depending on the local confiuration[47, 48]. Furthermore, the electron doping from copper substrate decrease the activation energy for diffusion of oxygen atoms[49, 50]. Finally, the oxygen atoms accumulate at grain boundaries of graphene because the high activation energy of 1.4 eV[48] is needed to escape from grain boundaries. Therefore, it is reasonable that the water dissociated oxygen radicals are supplied from monovacancy more frequently than from graphene grain boundaries. Finally, the oxygen atoms diffuse and accumulate on grain boundaries of graphene, and then the permeation of oxygen occurs as stone-wales defects with the support of facilitators.

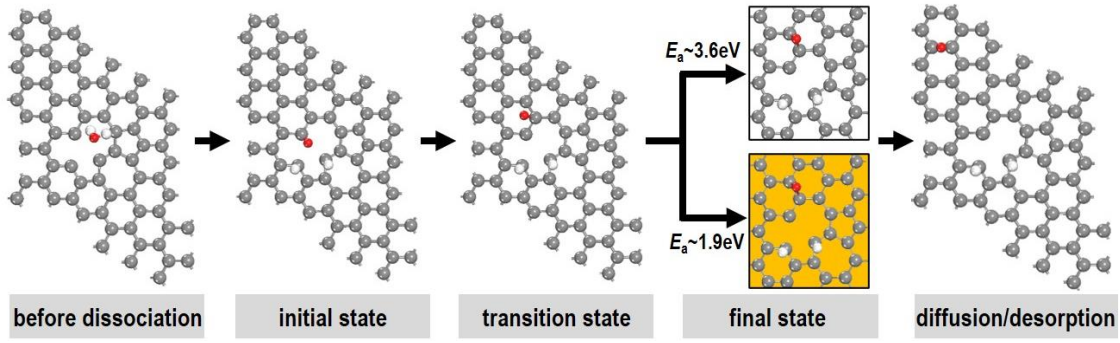

Figure 2.24 The configurations of a water molecule on a mono-vacancy. In this Figure, the white and red spheres are the hydrogen and oxygen atom.

The scheme of oxidation mechanism was suggested in Figure 2.25. In Figure 2.25a, we showed the level of reaction energy for whole oxidation method which is based on the oxygen atom reaction with stabilized configurations and activation energy for each reaction stage. In step 1, the water vapors from air dissociate into hydrogen and oxygen atoms at the graphene monovacancies with the activation energy of 0.04 eV, forming into a carbonyl group as the red dashed line in Fig. 5a and two C–H states[44]. In step 2, the hydrogen and oxygen atoms produced by water dissociation diffuse laterally from the monovacancies to other six carbon rings with the activation energy of ~1.9 eV. In step 3, the hydrogen and oxygen radicals consistently diffuse from a six carbon ring to another six carbon ring state with the activation energy of ~0.3 eV[51] and ~0.75 eV[47], respectively. In stage 4, the oxygen radicals accumulate at stone-wales defects of graphene having lower activation energy of 0.3 eV for diffusion from six carbon ring to grain boundaries than reverse reaction energy of 0.8 eV[48]. Finally, in step 5, the oxygen radical invers into underlying copper substrate through the stone-wales defect with the support of other attached O radicals, with the activation energy of 0.70 eV.

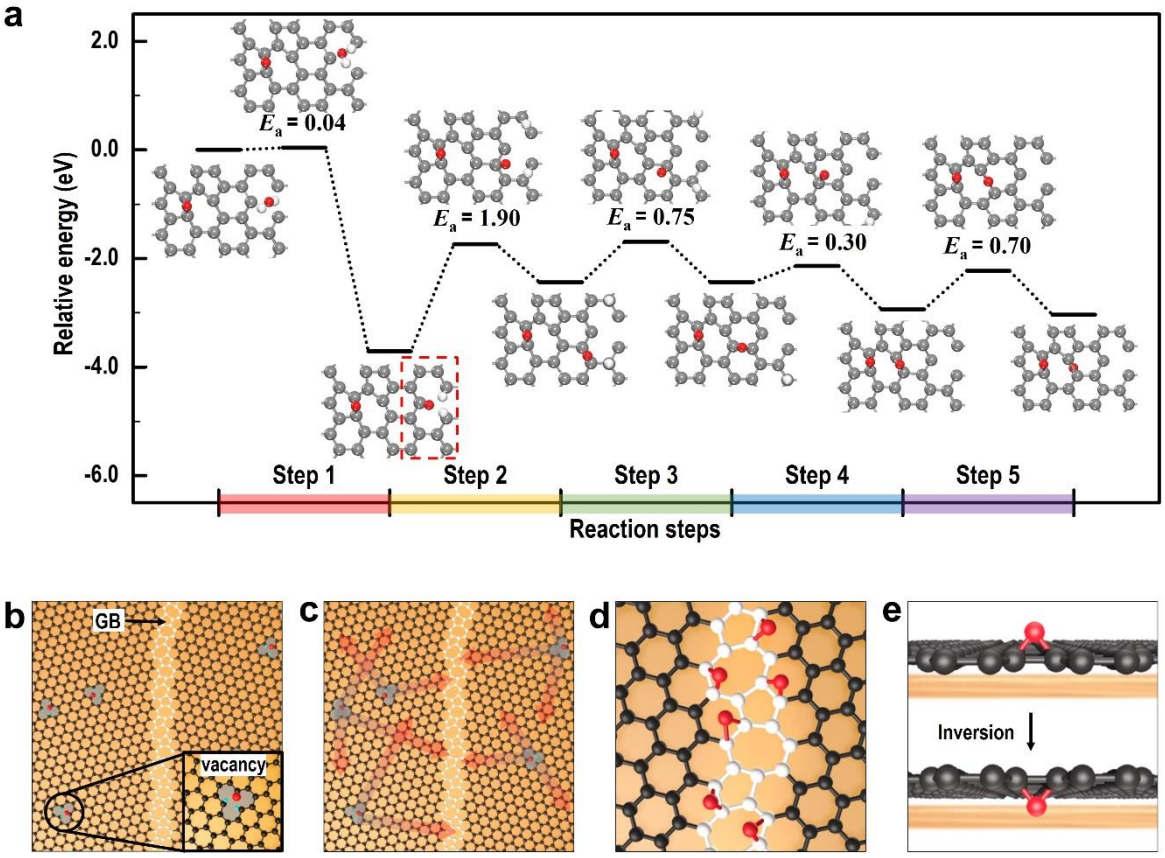

Figure 2.25 Reaction process and scheme of oxidation method. (**a**) Minimum energy rout of oxidation reaction (eV) from formation of oxygen radical dissociated from water at monovacancy to inversion of O radicals into graphene through grain boundaries on Cu (111) substrate. The carbon, hydrogen and oxygen atoms are represented as gray, white and red spheres. The scheme indicate representative stages of oxidation mechanism including (**b**) the dissociation of water at point defects in graphene, (**c**) the shift of oxygen radicals on the graphene, (**d**)the aggregation of oxygen radicals at the grain boundaries of graphene, and (**e**) the inversion of the oxygen radicals at a stone-wales defect with another oxygen as facilitator

Furthermore, as shown in Figure 2.26, we also confirmed that other functional groups as carboxyl and hydroxy groups were match with our oxidation mechanism because other functional groups were generously formed on graphene through XPS data in Figure 2.6a and 2.22a. The carboxyl and hydroxyl groups also has stable states at monovacancy as carbonyl groups, and we should confirm the possibility for the hydroxy and carboxyl groups to hinder our oxidation mechanism. We found that both functional groups could not diffuse from monovacancy, but they also could be dissociated to other states with activation energy using nudged elastic band calculations. The carboxyl group could be split into a hydroxyl group and a carbonyl group with activation energy of 0.72 eV. The dissociated OH radical can diffuse from the monovacancy to other site with activation energy of 0.5 eV[52]. Therefore, we can predict that the final configuration of dissociation of carboxyl group is the same with the state of water dissociation at monovacancies. This means that the carboxyl group formed on graphene can be dissociated to a carbonyl group joining our oxidation mechanism. Therefore, the carboxyl group formed on graphene does not prevent the oxidation method. In addition, we also examined that the opportunity for the hydroxyl group to dissociated into a carbonyl group and a single hydrogen atom. Because of high diffusion energy of 1.23 eV, the hydroxyl groups decelerate the oxidation process as shown in Figure 2.26.

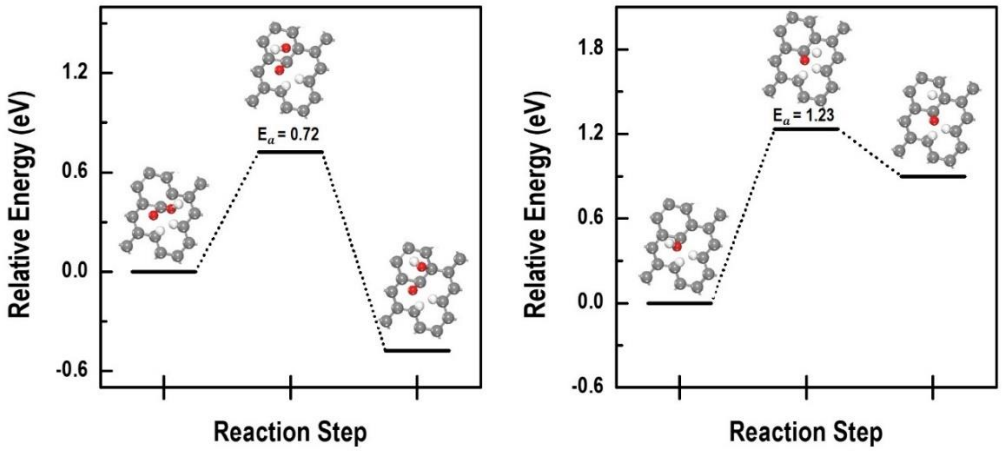

Figure 2.26 Minimum energy path for oxidation mechanism of Cu(111) substrate under graphene predicted by NEB calculations. At mono-vacancy graphene highlighted by red dotted-line, (**a**) carboxyl, (**b**) carboxylic acid, and (**c**) hydroxyl functional groups are introduced. The initial configuration is fitted to 0 eV. All calculations are including 3 layer of copper slab.

The copper oxidation occurs between graphene and copper substrate with penetration and dissociation of oxygen atoms in our works. We also observed the atomic deformation of the graphene stone-wales defects and the existence of unsaturated C atoms having the chain of 5- and 9- carbon ring after oxidation using aberration-corrected high resolution TEM. However, as shown in Figure 2.27, the grain boundaries are maintained in the investigated area without breaking. The deformation in the atomic structure of graphene grain boundaries may be caused by the high tensile strain induced by expansion of copper volume during oxidation[35-37, 53]. The main byproducts of oxidation from XPS measurement are expected to be located at unsaturated C atoms in grain boundaries having dangling bonds[54, 55]. In Figure 2.28, the ratio of oxygen to carbon was similar with the fraction of oxidation features in CVD graphene after 200 ºC oxidation for 120 min.

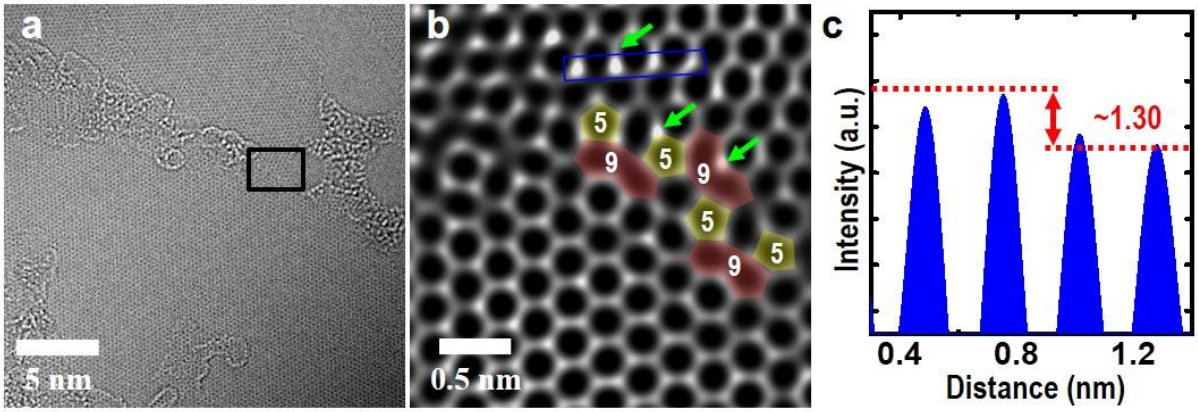

Figure 2.27 (**a**) A typical plan-view highly resolved TEM image of a graphene layer after air oxidation method for 120 min after transfer onto a TEM grid. (**b**) An atomically resolved image of a GGB, marked by a black square in a. (**c**) Intensity line profile taken from a blue square in (**b**).

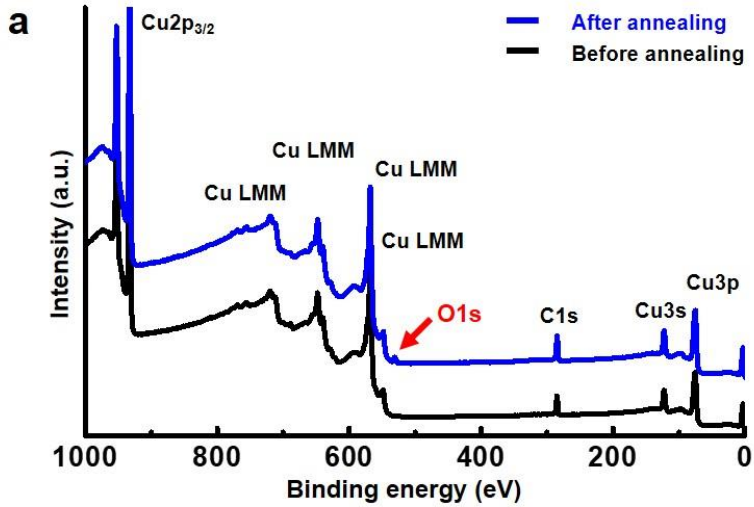

Composition (atomic percentage)

	Before annealing (%)	After annealing (%)
Cu	59.40	51.31
C	40.60	44.43
O	0	4.26
O/C		9.6×10^{-2} (8.8×10^{-2})

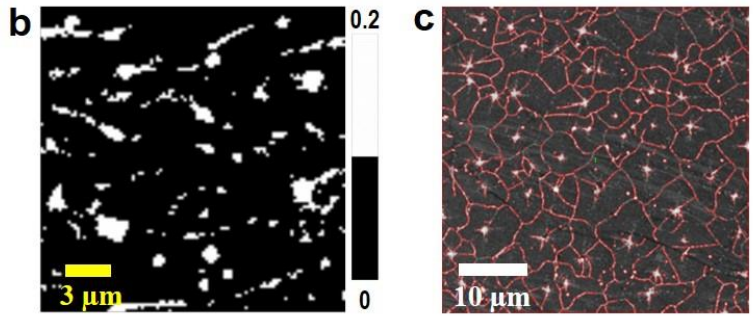

Figure 2.28 Chemical compositions of Gr/Cu after annealing at 200C in air

In addition, we also explored the possibility for the carboxyl groups to consistently oxidize the underlying copper substrate. We proceeded the consistent oxidation of as-grown CVD graphene samples as a function of oxidation time. In Figure 2.29 and 30, the average width of the oxidation features of graphene grain boundaries was linearly expanded from 0.25 to 1.40 μm during consistent oxidation from 2 hr to 48 hr. This result means that the oxidation consistently maintains without disturbance of carboxyl groups.

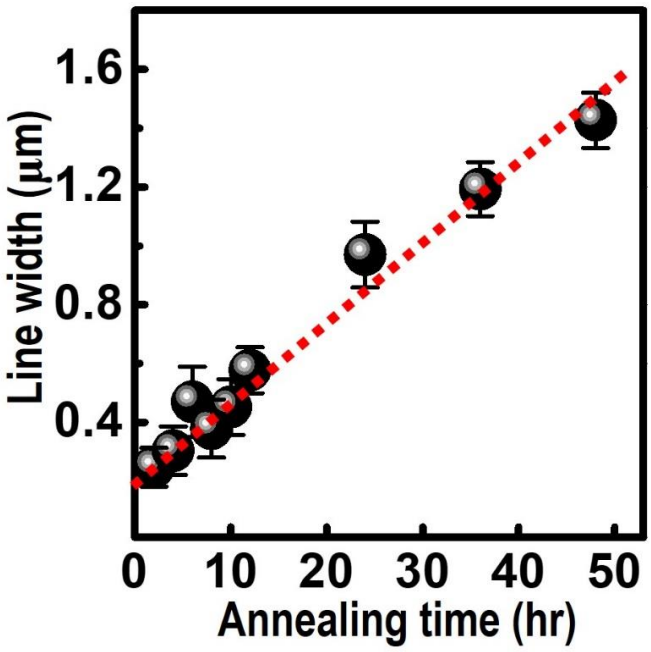

Figure 2.29 The average width of the oxidation feature as oxidation time is increased to 48 hr observed by SEM. Standard deviation as error bars are gained from 100 points in sample.

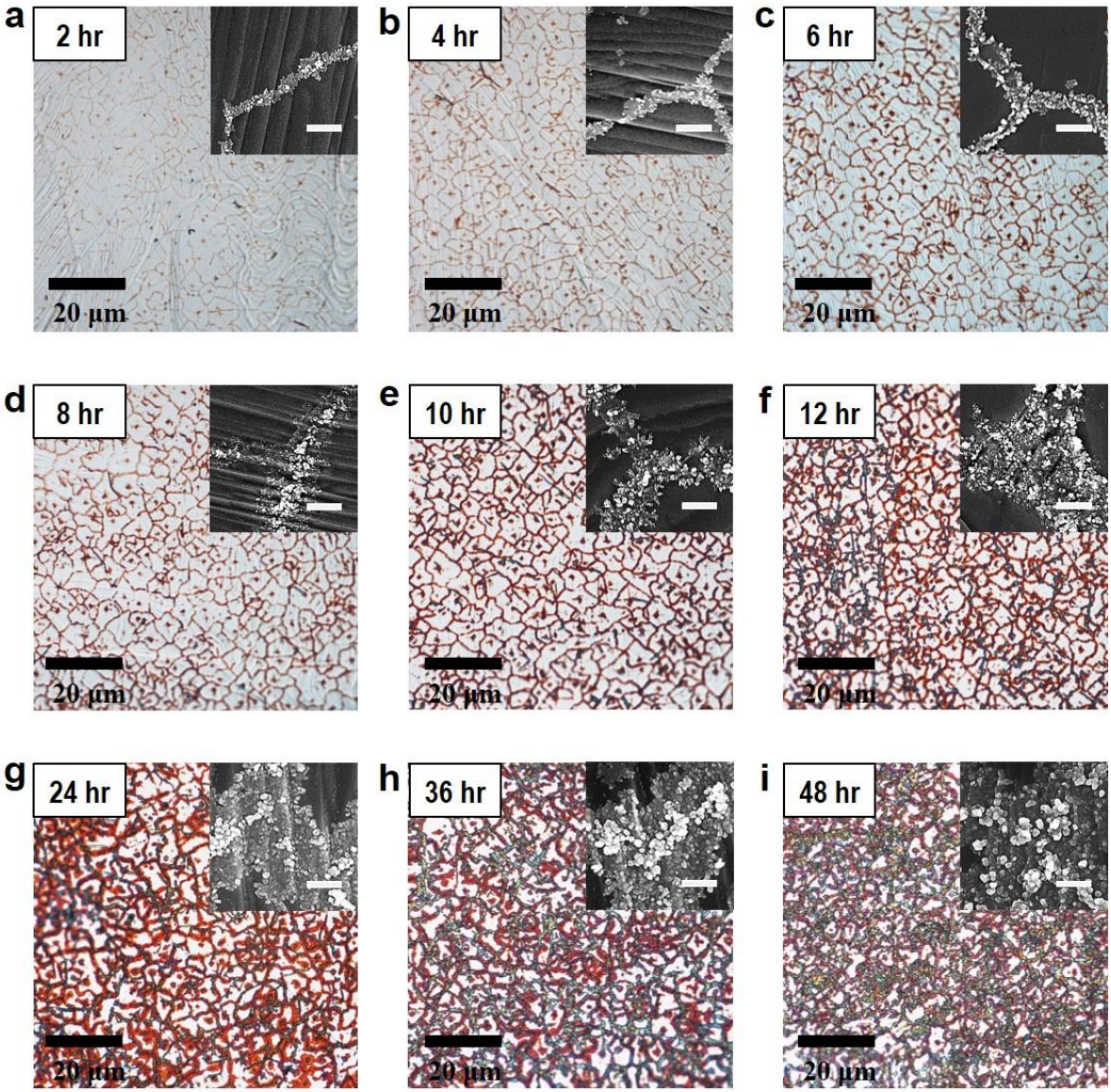

Figure 2.30 (a-i) OM images of as-grown graphene composites after air oxidation method for (**a**) 2, (**b**) 4, (**c**) 6, (**d**) 8, (**e**) 10, (**f**) 12, (**g**) 24, (**h**) 36, and (**i**) 48 hours. Insets in (**a-i**) are SEM images of oxidation features originated from the inter-granular grain boundaries. Scale bars are 500 nm.

2.6 Summary and Outlook

In conclusion, selective oxygen permeation and oxidation of underlying copper substrate visualize various atomic structural defects of graphene such as nucleation site defects, the intra and inter grain boundaries of graphene domains in large-area CVD grown graphene film. We also confirmed that the major origins for selective oxidation were the dissociation of water molecules in air through experimental and computational results. Through our oxidation method, we could estimate the level of CVD-grown graphene deficiencies with various dependences on the crystallographic orientations of copper substrate, growth conditions of graphene, and the growth rate of the graphene. In addition, we suggested that multilayer graphene growth was a core technology for reaching thin, flexible, and transparent protective barrier film for blocking permeation through chemical reaction from environment. This facile oxidation method can be applied to measuring the distribution of various intrinsic defects in large-area graphene film and optimizing the growth condition of graphene for commercialization. We also anticipate the oxidation method to be utilized to other CVD-grown two-dimensional materials besides graphene.

CHAPER 3

Water permeation through water permeable nano-sized holes of graphene

3.1 Water-permeable CVD-grown graphene

Many studies have shown that ideal graphene shows excellent impermeability to liquids, gases, and solids even if He which is smallest gas molecule, and many researchers have great expectations for its use as thinnest barrier film. Unfortunately, graphene grown through CVD does not reach the value required for practical commercialization as water vapor transmission rate (WVTR ≈ 1 $gm^{-2}d^{-1}$) and thus has limitations in diverse practical applications as barrier film[11, 56]. CVD-grown graphene, unlike the perfect graphene, has a variety of defects such as inter grain boundaries, intra grain boundaries, point defects, tears, and wrinkles and among these, it is believed that there will be permeable origins of graphene, and many researchers predict that water permeation will occur in atomic structural defects and various nanometer-sized holes of ≈1–10 nm[57-59].

When copper etchants contact with copper such as ammonium persulfate, ferric chloride, sulfuric acid, nitric acid or hydrochloric acid, reactive ions generally react with copper to form copper complexes and dissolve in water, resulting in copper chipping. Since graphene has excellent chemical stability and impermeability, when graphene coated copper is immersed in copper etching solution, copper etching occurs at water and ions permeable origins if graphene is not damaged. Therefore, the copper etching pits can find water permeable origins of CVD-grown graphene after dipping in copper etching solution such as hydrochloric acid.

Here, we use HCl etching method to systemically investigate the water permeable origins on the graphene grown on copper by CVD observing copper etching pits through optical microscopy and secondary electron microscopy. When we observed the distribution of these etching pits through SE and BSE mode of SEM, it was found that the etching pits mainly occurs at the copper surface underlying wrinkles of CVD-grown graphene induced by difference of thermal expansion coefficient. In addition, the copper etching pits were observed at the intersection of wrinkles of CVD-grown graphene and copper step bunches that formed below graphene during the growth process, after dipping in copper etchant for a short time. It was confirmed by emphasizing that the etching pits occurred at the junction of the wrinkles and the copper step bunches when the copper (111) had higher density of copper etching pits, which had the higher density of copper step bunches than copper (100). Furthermore, it was confirmed that nanosized ruptures, cracks, and holes were formed in folded graphene wrinkles through TEM. The water permeable origins of CVD-grown graphene have not been completely understood. However, HCl etching method can determine where the water permeations occur in the CVD-grown graphene. Moreover, these results will contribute to the application to graphene as protective barrier film for development of flexible organic electronics with high water impermeability offering flexibility.

3.2 Experimental Methods

Synthesis of graphene

A conventional thermal CVD equipment was utilized to grow graphene on copper foils (99.8% purity, 25-μm) that were previously cut into 4 × 3 cm^2. The foils were rinsed with acetone followed by isopropyl alcohol (IPA) to eliminate surface organic matters. After organic matters cleaning, those went through a process of electropolishing in 85 % w/w phosphoric acid for 15min to eliminate the impurities of Cu surface and then they were rinsed in distilled water followed by IPA for eliminating phosphoric acid residue. The Cu foils were put into a 4-inch quartz tube and the chamber was evacuated to ~3mTorr after the cleaning process. After evacuation, the temperature was increased to 1000–1050 °C with H_2 gas (5 sccm) flow maintaining evacuation of chamber. After the copper foils were annealed for 30min, the graphene was grown with CH_4 gas (10 sccm) for 30 min, and then cooling chamber with H_2 gas and CH_4 gas for full growth and without gas for partial growth.

Etching test for water-permeable origins

As-grown Gr/Cu composites were dipped in copper etchants (HCl solution 3.7 wt%, H_2SO_4 solution 10 v/v %, $FeCl_3$ solution 0.1 M) to etch the water-permeable origins of graphene for 10 s-10 min. After dipping in the etchants, the etched Gr/Cu composites were rinsed in deionized water for 1min and dried with nitrogen gun. After the process, the etched samples were characterized with SEM and OM.

Characterization

Raman spectroscopy and mapping data were gained with a WiTec Alpha 300R M-Raman which controlled the stage along x-y axis and have a 532 nm excitation source. The laser had a 640 nm spot size with a x50 objective lens (numerical aperture: 0.5). The measurement was proceeded with ~1 mW of laser power at the surface for preventing laser-induced thermal damage and effects. The data of Raman spectra and mapping were analyzed by the WiTec Project 2.10 provided from WiTec.

Electron-backscatter diffraction (EBSD) measurement was proceeded for analyzing the crystallographic orientations of the copper foils during CVD graphene growth with AMETEK EBSD equipment installed in a FEI Quanta 3D FEG SEM. The condition of measurements was set with the probe current, the incident angle, and the accelerating voltage being maintained at 16 nA, 70º, and 15 kV, respectively. The EBSD mapping was proceeded with a 0.25 μm step size and the data of EBSD mapping were analyzed through the TSL OIM Analysis 6 software for getting mapping images of inverse pole figures of the copper crystallographic orientation.

Scanning electron microscope was performed with secondary electron and back-scattered electron modes accelerating 1kV. The surface of samples was measured by atomic force microscopy (Bruker Multimode 8) in the tapping mode.

3.3 HCl etching for detecting water-permeable origins

We just dipped the graphene grown by CVD in HCl solution for 10 min to estimate the impermeability of macro-scaled graphene membrane as simple method. Many rectangular shaped pits newly occurred at surface of as-grown graphene/copper samples as shown in the red arrows of Figure 3.1. As shown in inset of Figure 3.1, those rectangular shaped pits were retractions of copper surface originated from etching copper surface, and these rectangular shapes were correlated to the crystalline orientation of copper (100) leading to anisotropic etching. It is needed to pass the water molecules, which have the O-H bond length as 0.97 Å and bend with 104.44º oxygen atom as axis, and reactive chloride ions through graphene membrane for arising this etching phenomenon. The penetrated chloride ions react with copper surface transformed to copper chlorides, which is water soluble, and the copper chlorides are soluble in water. Through these reactions, the etching pits of copper surface are distributed on graphene/copper samples meaning water permeable spots. The HCl molecules, which have a bond length of 1.28 Å, are entirely dissolved in water forming hydronium cations and chloride anions with large ionization constant of -6.3 at room temperature as hydrochloric acid solution. When the hydrochloric acid solution reacted with copper, two complexes of copper and chloride are produced as $CuCl_2$ or H_2CuCl_4, and these complexes were immediately dissociated into $[Cu(H_2O)_6]^{2+}$, Cl^-, and $[CuCl_{2-x}]^{x-}$ ions in water[60]. Therefore, we can easily estimate the distribution of water permeable origins on CVD-grown graphene through observing the micro-sized copper etching pits.

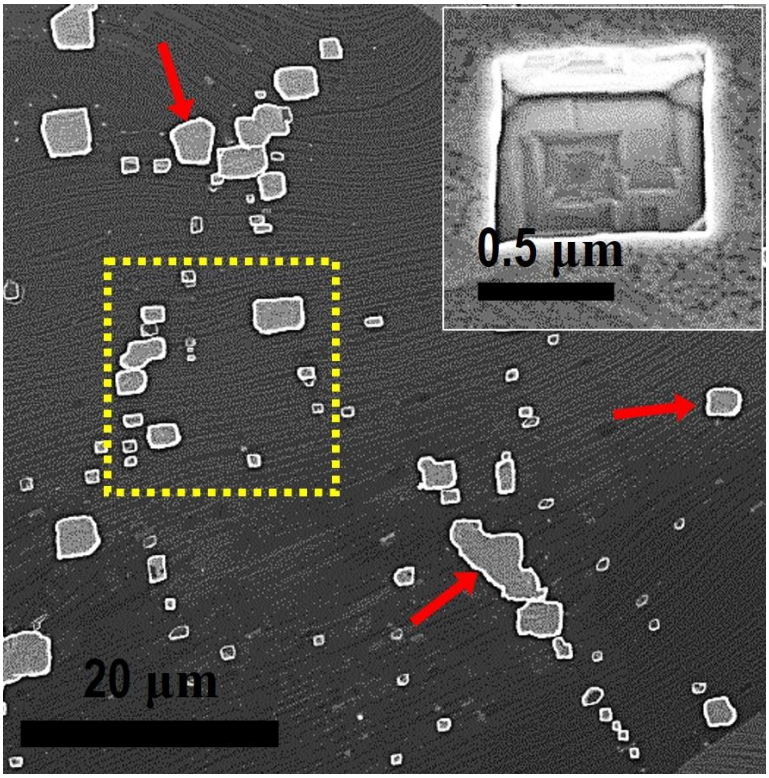

Figure 3.1 A SEM image of the as-grown graphene after HCl etching method for 10 min. Inset indicates a highly magnified SEM image of an etch pit

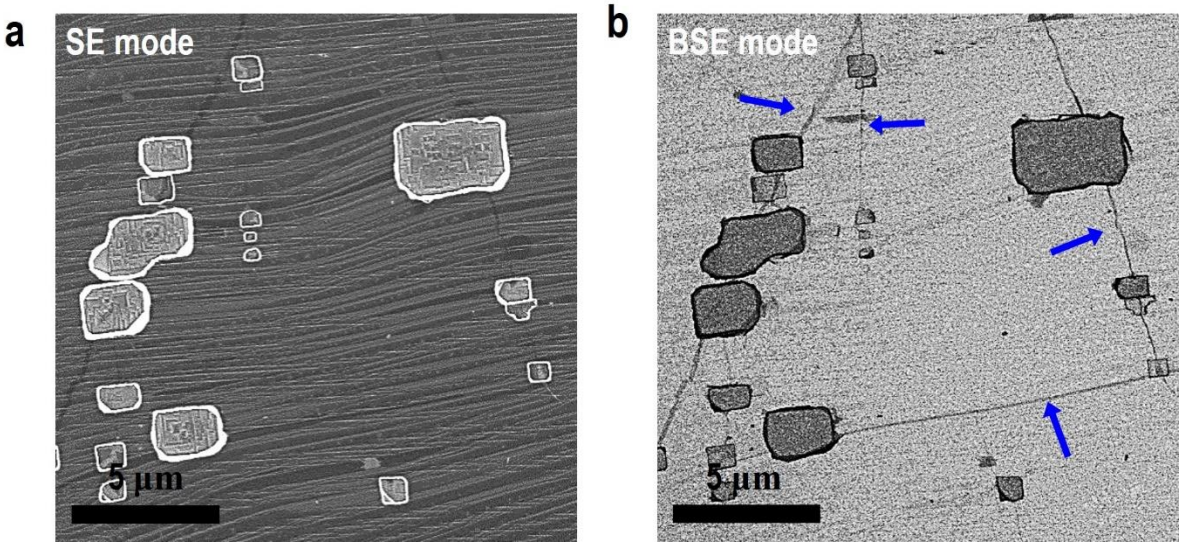

Figure 3.2 SEM images of the area a yellow-dotted square in Figure 3.1 using (**a**) SE and (**b**) BSE modes

We firstly recognized that the position of etching pits was related to the wrinkles of graphene using HCl etching method. The formation of wrinkles are inevitable in high temperature CVD graphene growth on copper because of the difference of thermal expansion coefficients between copper surface and graphene[33, 61]. We proceeded the SEM measurement with back-scattered electron mode for clearly observing the folded graphene wrinkles with stacking the graphene layer on copper foil[62]. The back scattered electron mode can detect elastically scattered electrons generated from response for an accelerated electron collision to surface of sample. Therefore, the back scattered electron SEM images have more information about the atomic number of measured area than about morphology of surface such as copper stem bunches. Furthermore, back scattered electrons arisen from copper surface were diminished as penetration of the graphene layers, so the BSE mode could emphasize the contrast of images according to thickness of graphene. There are SEM images detected by the secondary electron and back scattered electron modes appearing that most of copper etching pits occurs at wrinkles of graphene with blue and red arrows in Figure 3.2 a, b. As shown in Figure 3.3, regardless of the crystallographic orientations of copper substrate, the HCl etching pits were mainly located at the wrinkles of graphene grown on Cu (100), Cu (111), and high-index orientations. In addition, we proceeded the HCl etching method to partially merged graphene islands with four-lobed shapes on Cu (100) to explore the etching behavior at graphene grain boundaries by shortening the growth time of 1~2 min. Most of copper etching pits, which were located at the single graphene islands without graphene grain boundaries, occurred at the wrinkles of graphene as shown in yellow colored area of Figure 3.4a. We also examined the HCl etching method to graphene grain boundaries, which were merged with two graphene islands, showing that there was no copper etching pits on red-dotted square in Figure 3.4b. Through this result, we confirmed that the well stitched grain boundaries of graphene had excellent impermeability of water molecules with blocking the formation of copper etching pits. In other words, the wrinkles formed on CVD-grown graphene are the main origins permitting the water permeation to the opposite side. This result is different with selective permeation of oxygen and hydroxyl radicals through atomic structural defects of CVD-grown graphene as shown in the previous reports[8, 63, 64].

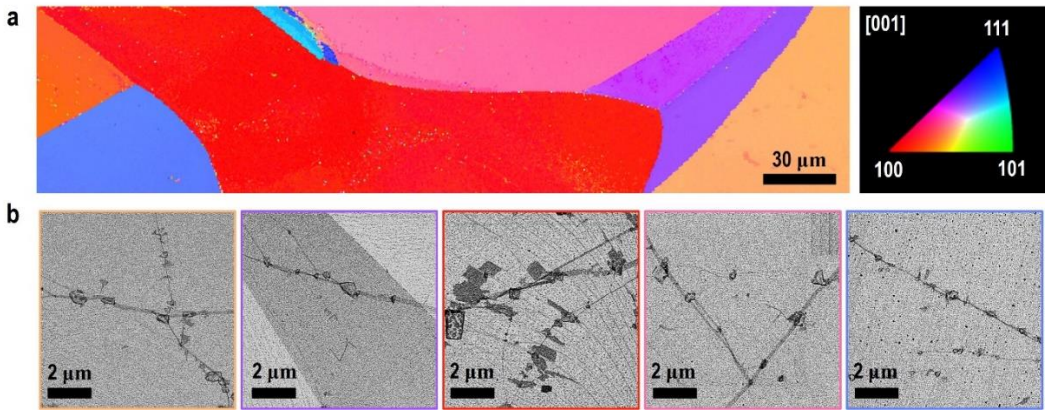

Figure 3.3 (**a**,**b**) A typical EBSD map image of the etched as-grown graphene after HCl etching method and corresponding SEM images measured by the BSE mode of Gr surfaces grown on different Cu orientations. The right in (**a**) is a inverse pole figure.

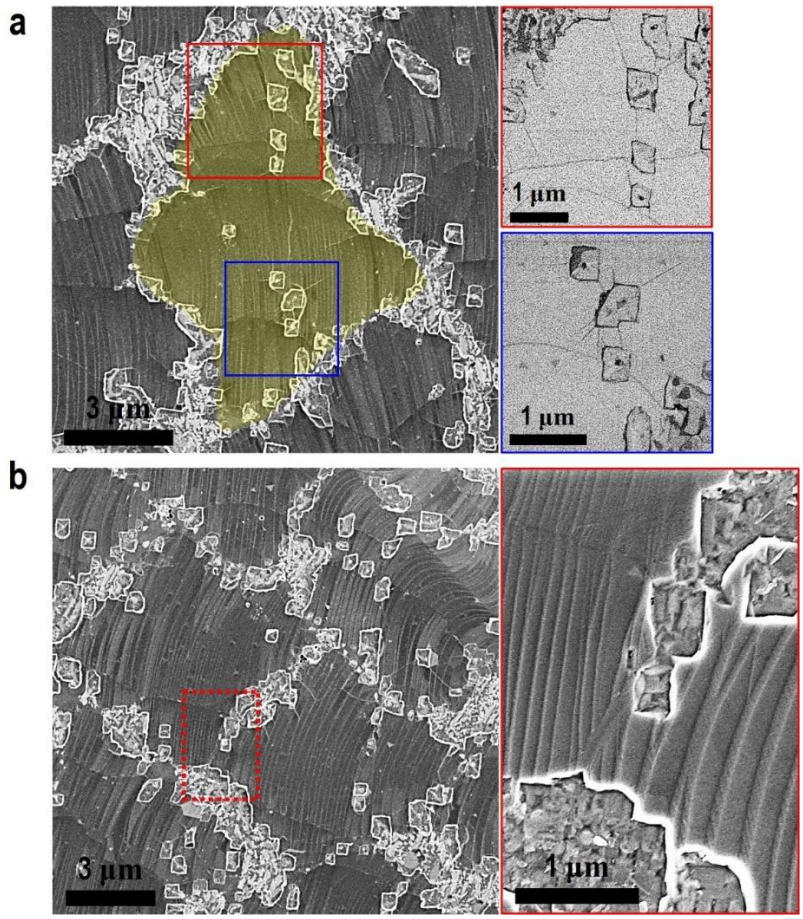

Figure 3.4 SEM images of partially grown graphene on a copper after HCl etching method. Right in (**a**) is BSE-SEM images of the area as a red and blue square. Right in (**b**) indicates a highly magnified SEM image of the grain boundary of graphene from combining nearby graphene islands.

3.4 Main water-permeable origins of CVD grown graphene on copper

For deeply investigating the phenomenon passing the water molecules through graphene wrinkles, we examined the evolution of copper etching pits according to etching time dipping in hydrochloric acid solution. The tiny etching pits was detects along the wrinkles of graphene with optical OM dipping the samples in HCl solution for short time below 3 min in Figure 3.5a, and these pits were just grown up combining a pit with another pit according to increasing dipping time from 3 min to 60min, without nucleation of new etching pits. In addition, the size of copper etching pits was varied in the same sample induced by the size and density of water permeable origins. Firstly, through the result of etching time control, this difference of size in 60 min etching was induced by the combining close etching pits each other as shown in red-dotted squares of Figure 3.4b. Furthermore, we also confirmed that the sizes of copper etching pits were different when dipping in solution for a short time below 1 min, although the etching pits were not merged each other as shown in blue-dotted circles of Figures 3.6 and 3.7. This result means that the sizes of water permeable origins are different in CVD-grown graphene. We also examined the etching method for detecting water permeable origins using other copper etchants such as sulfuric acid and ferric chloride, and the sizes of etching pits were varied with the sort of copper etchants because of difference of etching ability as shown in Figure 3.8. Through the results, we confirm that the water permeation is not induced by chemical reaction unzipping the graphene lattice as oxidative unzipping of carbon nanotubes[56, 65, 66]. Through HCl etching method, we can perceive that the origins of water penetration are located at wrinkles of graphene, and the cooling process is also a important key of reducing water permeation because the wrinkles are formed when the sample cools down to room temperature.

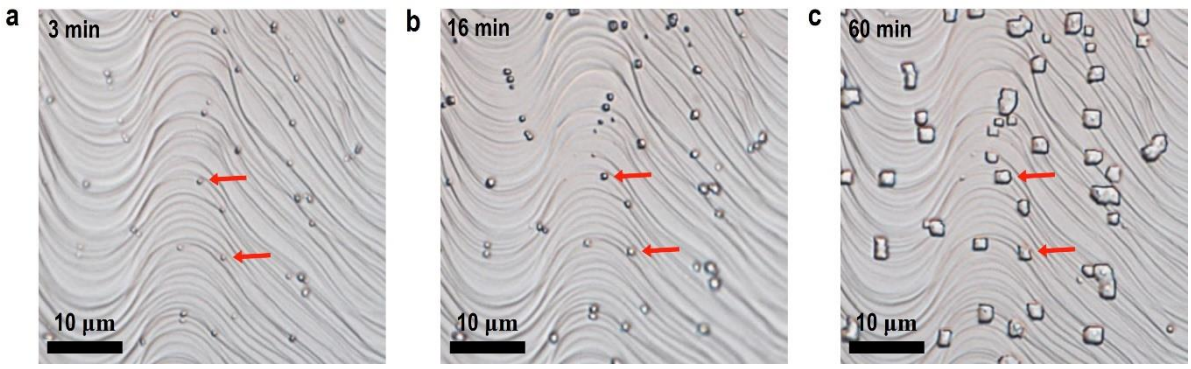

Figure 3.5 (**a**-**c**) OM images of as-grown graphene after HCl etching method for 3 (**a**), 16 (**b**), and 60 min (**c**). Red arrows indicate the etching pits at same positions.

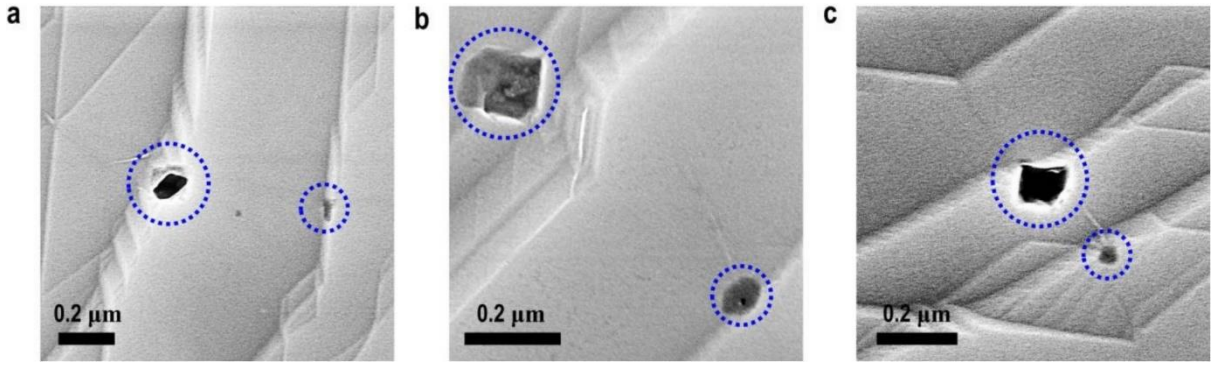

Figure 3.6 (**a-c**) High resolution SEM images of as-grown graphene after HCl etching method for a short time (≤1 min).

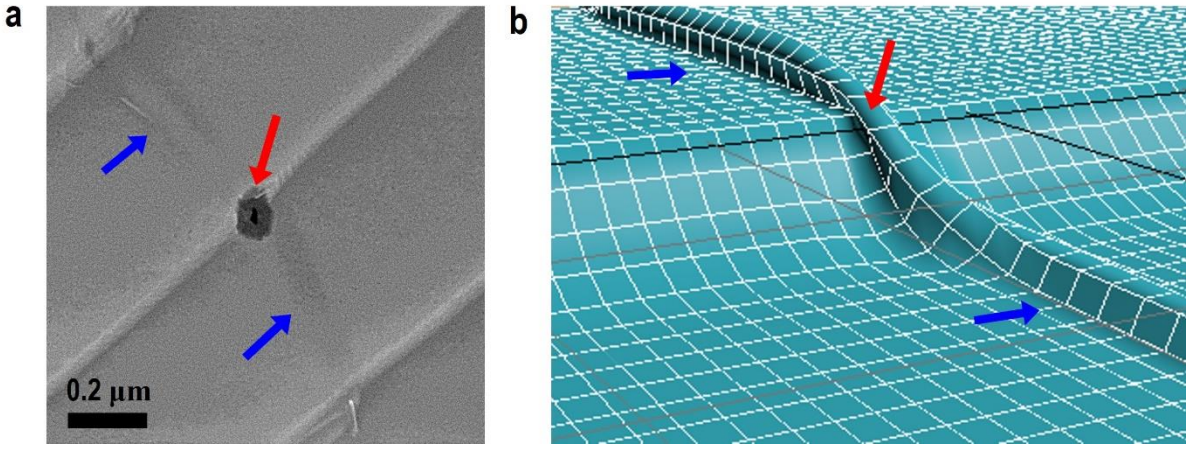

Figure 3.7 A representative SEM image (**a**) and a schematic diagram (**b**) of the Gr/Cu surface underlying a Gr wrinkle (blue arrows) after short etching time (<1min).

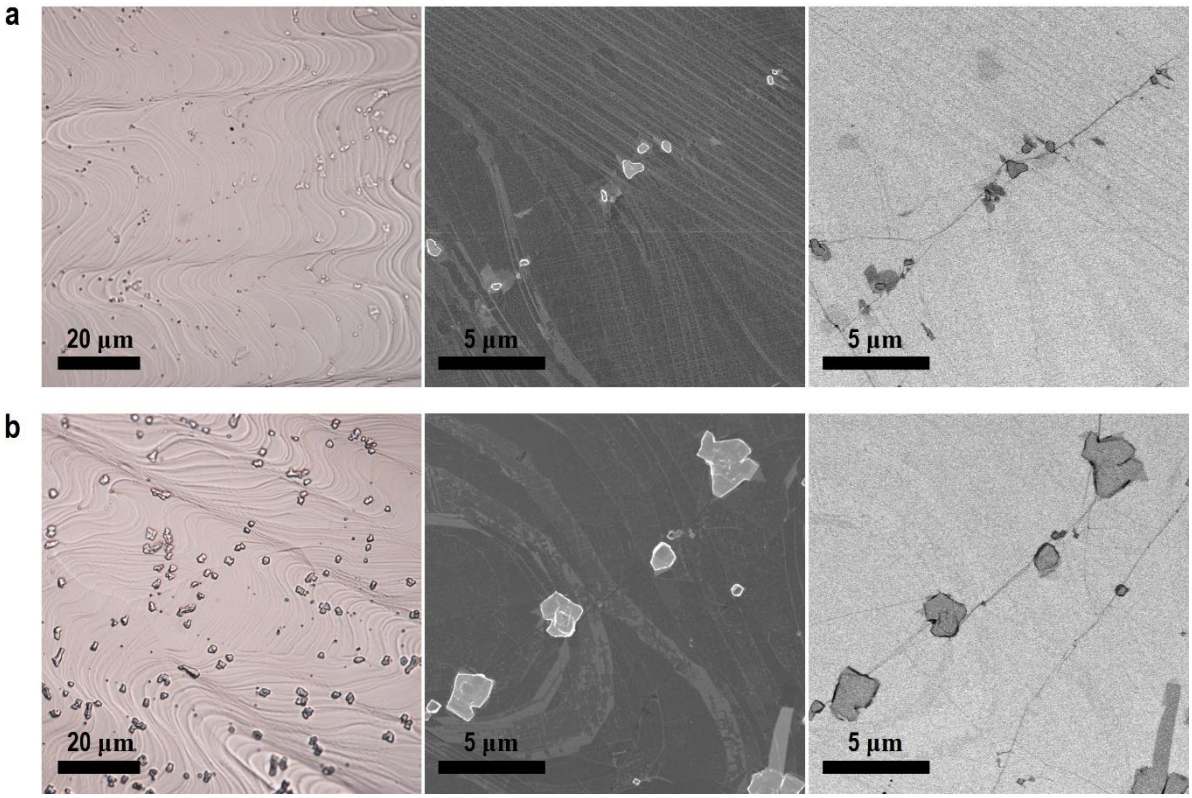

Figure 3.8 (**a**) Representative OM, SE-SEM, and BSE-SEM images of as-grown graphene after etching with H_2SO_4 solution (10 v/v %) for 10 min. (**b**) Typical OM, SE-SEM, and BSE-SEM images of a as-grown graphene after etching with an $FeCl_3$ solution (0.1 M) for 3 s. These results indicate that Cu etching pits are dominantly located at the wrinkles of graphene regardless of etchants.

To examine the role of wrinkles for water permeation, we proceeded the reannealing of as grown graphene/copper composites at 400 °C, and we observed the change of etching pits distribution after HCl etching method. The wrinkles of as-grown graphene are straightened by increase of temperature, and the wrinkles are recovered to form the wrinkles again on similar position of as-grown graphene during cooling stage because the distribution of intrinsic defects affects the formation of wrinkless[67, 68]. The density of copper etching pits as 5.6×10^7 cm^{-2} during second wrinkling was higher than that during as-grown wrinkling as 2.2×10^6 cm^{-2} in Figure 3.9b. Furthermore, the copper etching pits also occurred at the second wrinkles of reannealing samples as as-grown CVD graphene in Figure 3.9c and d. Through the result, we confirm that the origins of water permeation as nanosized holes are mainly formed by the graphene wrinkling process as detaching the graphene layer from copper substrate or folding the graphene layer on rough copper step bunches, occurring by the difference of thermal expansion coefficients between graphene and copper surface. In addition, we confirmed that the copper etching pits were located at intersecting point of copper step bunches with the wrinkles, originated form the kinetics of copper atom with sublimation on the copper surface during high temperature CVD growth[4].

To deeply examine the phenomenon, we proceeded that the as-grown graphene was dipped in HCl solution for a short time below 1min for finding the origins of water permeation in detail. The etching pits were located at the intersecting points of graphene wrinkles and copper step bunches in Figure 3.7a. In addition, we also proceeded the HCl etching method to two copper crystallographic orientation (100) and (111) which had a different density of copper step bunches. As a result, the density of copper etching pits on a Cu(111) had higher value as 4.0×10^6 cm^{-2} than Cu (100) as 2.2×10^6 cm^{-2} because the density of Cu (111) step bunches was higher than that of Cu (100) in Figure 3.10. In consideration of our results and previously reported fracture and binding energy of graphene [69-71], it is reasonable that the graphene layer are strictly bound to copper step bunches, which are rough and protruded. The extraordinary surface induces the nanosized holes and fractures for water permeation origins during wrinkling process rather than other smooth surface.

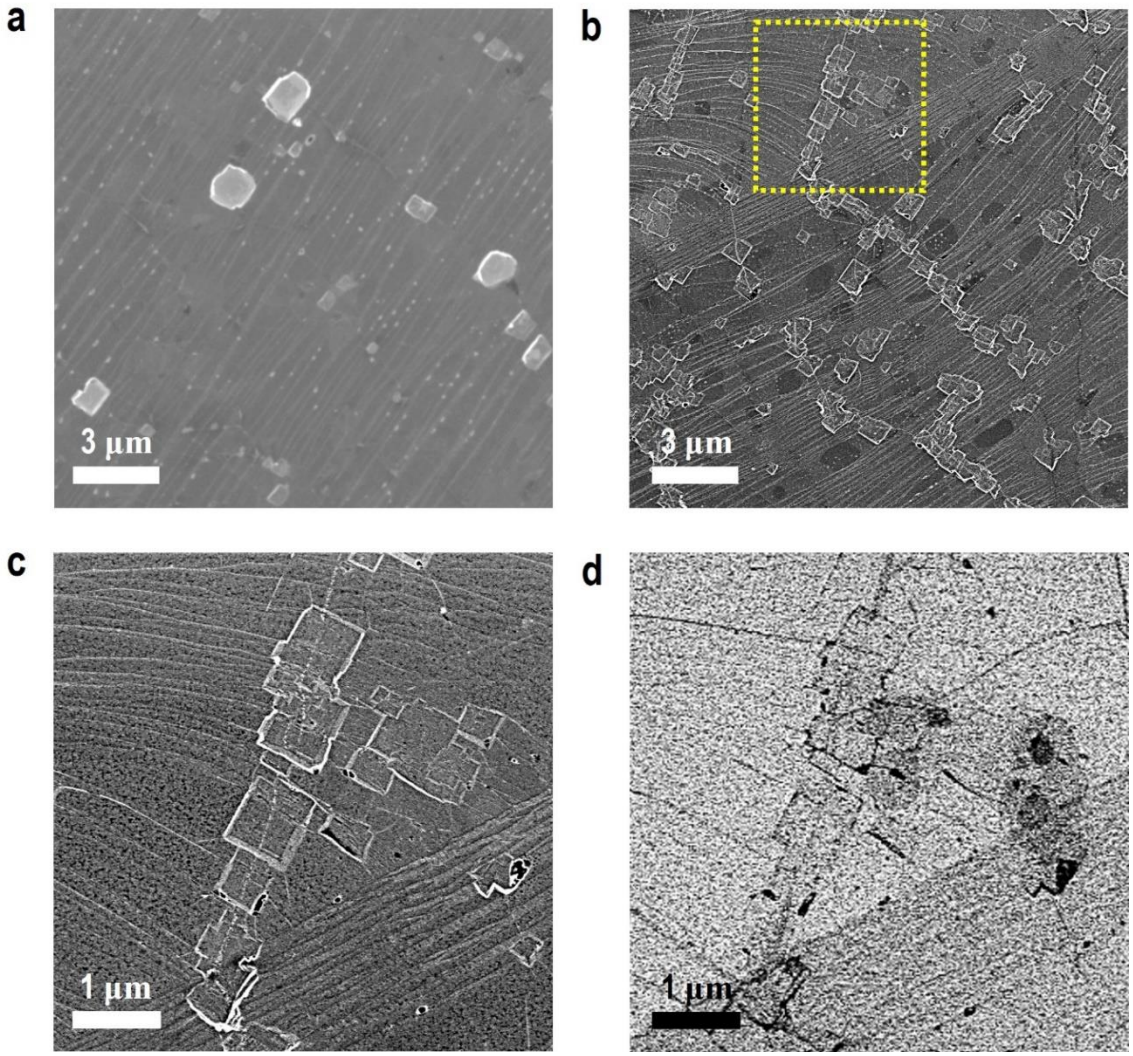

Figure 3.9 Typical SEM images of as-grown graphene without (**a**) and with heating in vacuum at 500 °C for 1 min (**b**) after HCl etching method. (**c,d**) High magnification SEM images of a yellow square in (**b)** detected by SE (**c**) and BSE mode (**d**).

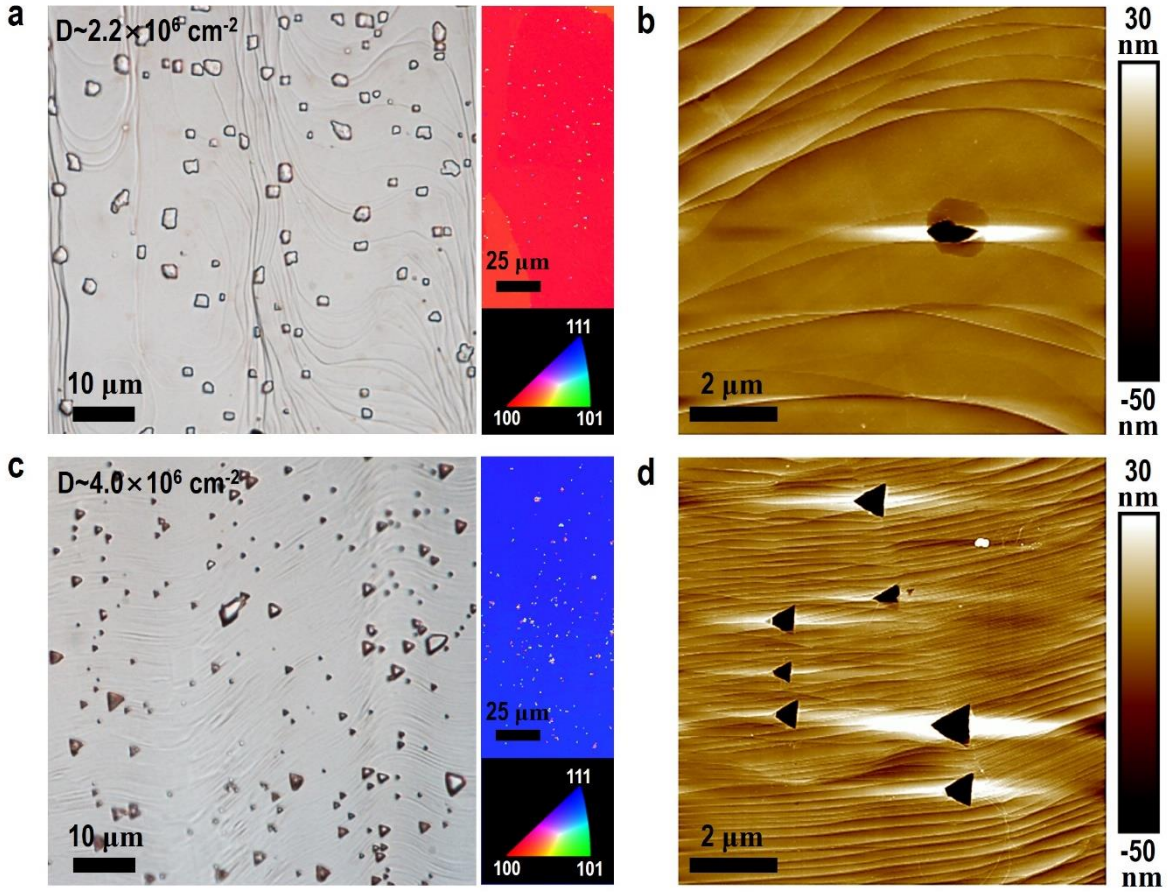

Figure 3.10 A typical OM and an AFM image of the as-grown graphene surface on Cu (100) (**a,b**) and Cu(111) (**c,d**). In **a** and **c**, right panels are corresponding EBSD maps.

3.5 Transmission electron microscope image of water-permeable points

We proceeded TEM study to deeply observe the intrinsic defects on wrinkles of graphene. Firstly, the CVD-grown graphene was directly transferred on TEM grid through previously reported direct transfer which etched the copper substrate without PMMA coatings[24]. The most of wrinkles of graphene were formed as folded layer structure as shown in Figure 3.11[41]. When the graphene monolayer was folded twice, the wrinkle structure was locally formed as triple layer of graphene as shown in inset of Figure 3.11b. Through the TEM measurement, it was observed that the wrinkles consisted of top edge folded part as blue arrows of Figure 3.11 and Moiré patterns formed by stacking three graphene layers[23]. There were three specific water permeable defects such as nanosized ruptures, cracks and holes on flat surface as shown in Figure 3.11c through high resolution TEM images. In previously reported scanning tunneling microscopy researches, there were no water permeable defects such as nanosized ruptures, cracks or holes on the wrinkles of graphene[67, 72], because the STM researches were proceeded in the condition with single crystal metal substrate and smooth surface for STM measurement not intersecting the wrinkles to copper step bunches. Therefore, our results are reasonable to form various water permeable origins on the wrinkles of graphene, which is grown by conventional CVD system. Moreover, we also predict that the nanosized water permeable origins on the edge of wrinkle were mainly originated from wrinkling process as the delamination of as-grown graphene from copper step bunches or strain induced by deformation of rough copper step bunches as shown in the location of copper etching pits on intersecting point between wrinkles and step bunches.

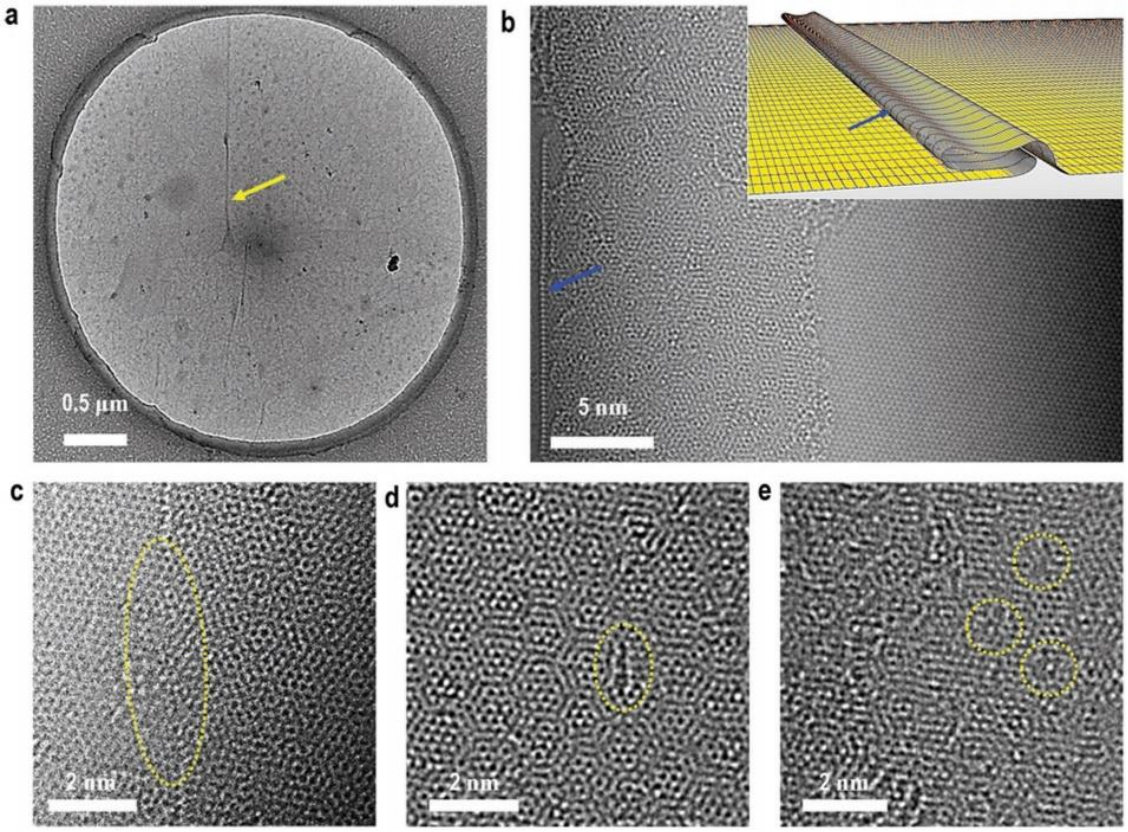

Figure 3.11 (**a**) Lowly magnified TEM image of CVD-grown graphene having the wrinkle marked by a yellow arrow. (**b**) Highly resolved TEM image of wrinkle. Inset of (**b**) is a scheme of folded wrinkle structure. (**c**–**e**) Highly magnified TEM images of intrinsic defects located at wrinkle in (**b**) (**c**) nanosized ruptures located at the edge of wrinkle, (**d**) cracks, and (**e**) holes.

3.6 Summary and Outlook

In conclusion, there were nanosized ruptures, cracks and holes on CVD-grown graphene on copper substrate, which acted as water permeable origins. With HCl etching method, it was confirmed that the main origins were located at wrinkles of graphene degrading water impermeability of graphene layer grown by CVD system etching the underlying copper foil. Through high resolution TEM studies, the water permeable defects were directly observed as nanosized ruptures, cracks or holes below 3 nm on wrinkles of CVD-grown graphene. In addition, we confirmed that the water permeable origins on wrinkles of graphene were originated from wrinkling process for releasing compressive stress by detaching of graphene layer from copper step bunches or strain induced by deformation on rough copper step bunches. The methodology for tracking the water permeable origins will be applied to enhancing the impermeability of graphene and other two-dimensional layer for protecting the large area, flexible, and transparent productions from hazardous environment to various devices. Furthermore, the elimination of copper step bunches and wrinkles in CVD-grown graphene is a challenge for handing over the graphene layer to commercialization as thinnest impermeable barrier film.

CHAPTER 4

Enhancing impermeability of CVD grown graphene

4.1 Graphene as protective barrier

As part of efforts to make electronic products more closely related to our real life, the expectations of smart electronics life have grown with the development of light, flexible, compact and transparent electronic components. Flexible organic devices are weak to water and oxygen in ambient air degrading performance of organic materials and electrodes with oxidation and corrosion, that is why barrier materials are inevitable for various electronics industries including display[73, 74]. In addition, the flexible and transparent protective barrier film is a problem awaiting solution to bring the industries to convenient new-type life style.

Graphene is an atomically thin 2D carbon material with hexagonal lattice structures. Excellent electrical, chemical, mechanical properties of graphene have attracted attention of many researchers after debut of exfoliated graphene. Graphene atomic structure is densely packed to hinder the penetration of gases or liquids, then the graphene has been focused as a promising barrier material with its flexibility and transparency[2, 13, 14]. Many researchers have developed impermeable composites to deposit inorganic materials such as silicon oxides and aluminum oxides using sputter, chemical vapor deposition, and atomic layer deposition. However, inorganic impermeable films have poor flexibility for applying to flexible organic devices. In this point, graphene films have potential power to realize flexible organic display for gas impermeable, flexible and transparent electrodes. Although mechanical exfoliated graphene has perfect impermeable ability, the CVD-grown graphene which is inevitable for mass production have poor impermeability for applying to organic devices because of water permeable origins such as nanosized ruptures, holes and cracks at wrinkles in chapter 3.

For practical applications of graphene as impermeable layer, graphene has been combined with other polymeric substrate, multi-stacking graphene, two-step growth for low nucleation, and so on. However, the WVTR value is limited from 10^{-1} to 10^{-2} 1 $gm^{-2}d^{-1}$ [11, 75]. For commercial flexible organic devices, the WVTR value must be down to 10^{-6} $gm^{-2}d^{-1}$.

Here, we describe a simple protocol to enhance impermeability of graphene by amorphous carbon (a-C) layer deposited by an electron beam, sputtered carbon, and CH_4 plasma expecting the impermeability of CVD-grown graphene with HCl etching method. It was employed to passivate the graphene nanosized ruptures, holes and cracks less than 5nm, formed on crossing points of wrinkles and copper step bunches. For effectively blocking the water permeation, the a-C layer is needed to be deposited up to 5 nm. In addition, the wrinkles on the part of multilayer graphene also had excellent water impermeability to copper etchants. Through the suggestion of these carbon-based layers, flexible, transparent, and thin barrier films will be developed for water impermeable electrodes and substrates to

safely protect future ubiquitous electronics from the air being exposed to everyday life.

4.2 Experimental methods

Two step bilayer growth

A conventional thermal CVD equipment was utilized to grow graphene on copper foils (99.8% purity, 25-μm) that were previously cut into 4 × 3 cm^2. The foils were rinsed with acetone followed by isopropyl alcohol (IPA) to eliminate surface organic matters. After organic matters cleaning, those went through a process of electropolishing in 85 % w/w phosphoric acid for 15min to eliminate the impurities of Cu surface and then they were rinsed in distilled water followed by IPA for eliminating phosphoric acid residue. The Cu foils were put into a 4-inch quartz tube and the chamber was evacuated to ~1 mTorr after the cleaning process. After evacuation, the temperature was increased to 1050 °C under flowing H_2 gas (100 sccm) with evacuation. After the copper foils were heated for 30min, the graphene was slowly grown with CH_4 gas (0.5 sccm) for 1 hr, and then the methane gas flow was increased to 2 sccm for 1 hr to connect between domains. After growth, the chamber was cooled with H_2 gas and CH_4 gas to room temperature.

Graphene transfer

Graphene/copper foil composites were coated with 5 wt. % poly(methyl methacrylate) (PMMA) as supporting layer by spin coating of 3000 revolutions per minute for 60 sec and annealed at 130 ºC for 10 min. After PMMA coating, the graphene of copper foils backside was eliminated with O_2 plasma for 30 min and the copper foils were etched with 0.1 M ammonium persulfate with floating those composites. After etching process, the PMMA/graphene layers are rinsed by floating on fresh deionized water three times and scooped on SiO_2/Si substrates. PMMA layers is eliminated with acetone after mild dry(50 ºC for 30 min) and hard dry(130 ºC for 30 min).

E-beam induced Deposition of a-C Layer

In SEM equipment (FEI Quanta 200FEG), the amorphous carbon layer was deposited on the scanned area of sample. The SEM chamber was evacuated to high vacuum as 3×10^{-6} Torr. The electron voltage was accelerated as steps from 1 to 15 kV for varying the deposition condition. The quantity of electrons current was measured by Faraday cups at the specimen position. Along the scanned time from 10 to 50 min, the thickness of amorphous carbon layer was linearly increased with constant SEM scan conditions as current of 10 nA accelerated with 1 kV and the scanned area of 69.51 × 47.87 μm^2.

Ar^+ ion bombardment induced deposition of a-C layer

Precision etching and coating system (PECS, Gatan 682) was used for deposition of a-C layer. The PECS chamber was evacuated to $2x10^{-5}$ Torr. After evacuation, the argon ion beam was accelerated with 5 kV and the beam current of left and right gun was stabilized at 180 μA for sputtering carbon-source plate. After sputtering the carbon plate for 1min without exposure of Gr/Cu samples to make a deposition condition, Gr/Cu samples were exposed to sputtered carbon for 1~5 min.

CH_4 plasma induced deposition of a-C layer

Plasma enhanced chemical vapor deposition system (PECVD, FABStar+) was used for deposition of a-C layer. The deposition chamber was increased to 100 ℃ and loaded as-grown Gr/Cu samples. The chamber was evacuated under 1 mTorr and stabilized with CH_4 gas flow (50 sccm) at 60 mTorr through automatic gate control. Methane plasma was ignited with 300 W from 13.56 MHz radio frequency generator and a-C layer was deposited on Gr/Cu samples for 1~10min.

Characterization

Raman spectroscopy data were gained with a WiTec Alpha 300R M-Raman which controlled the stage along x-y axis and have a 532 nm excitation source. The laser had a 640 nm spot size with a x50 objective lens (numerical aperture: 0.5). During the measurement, the laser power was ~1 mW at the sample to avoid laser-induced thermal damage or effects. The data of Raman spectra were analyzed through the WiTec Project program.

Scanning electron microscope was performed with secondary electron and back-scattered electron modes accelerating 1kV. The surface of samples was measured by atomic force microscopy (Bruker Multimode 8) in the tapping mode.

4.3 Selectively enhancement of CVD graphene water impermeability

We found a fresh method for enhancement of water impermeability of CVD-grown graphene membrane, which have various water permeable origins as nano-sized ruptures, cracks, and holes on wrinkles. The amorphous carbon layer was selectively deposited on SEM scanned area induced by electron beam of SEM, and this technique was used to deposition of amorphous carbon layer on wrinkles of graphene without damage to graphene lattice. Interestingly, the gaseous carbon contaminants in SEM chamber and surface of sample can be decomposed to amorphous carbon depositing amorphous carbon layer on electron beam scanned area[76, 77].

As shown in Figure 4.1a-c, below an irradiation time of 30 min, With this method of deposition time below 30 min, the copper etching pits were detected at the wrinkles of graphene after HCl etching method as shown in Figure 4.1 a-c, and the size of copper etching pits with amorphous carbon deposition was smaller than that of undeposited area. However, when the deposition time increased up to 40 min having thickness of 2.3 nm, there were no copper etching pits along wrinkles of graphene in Figure 4.1 d and e. Through the experiment, we predicted that the water permeable defects on wrinkles of graphene had a size below 3 nm as shown in Figure 4.1f. Therefore, the water permeable origins were welded by the amorphous carbon layer of 2.3 nm thickness deposited by electron beam induce in SEM system.

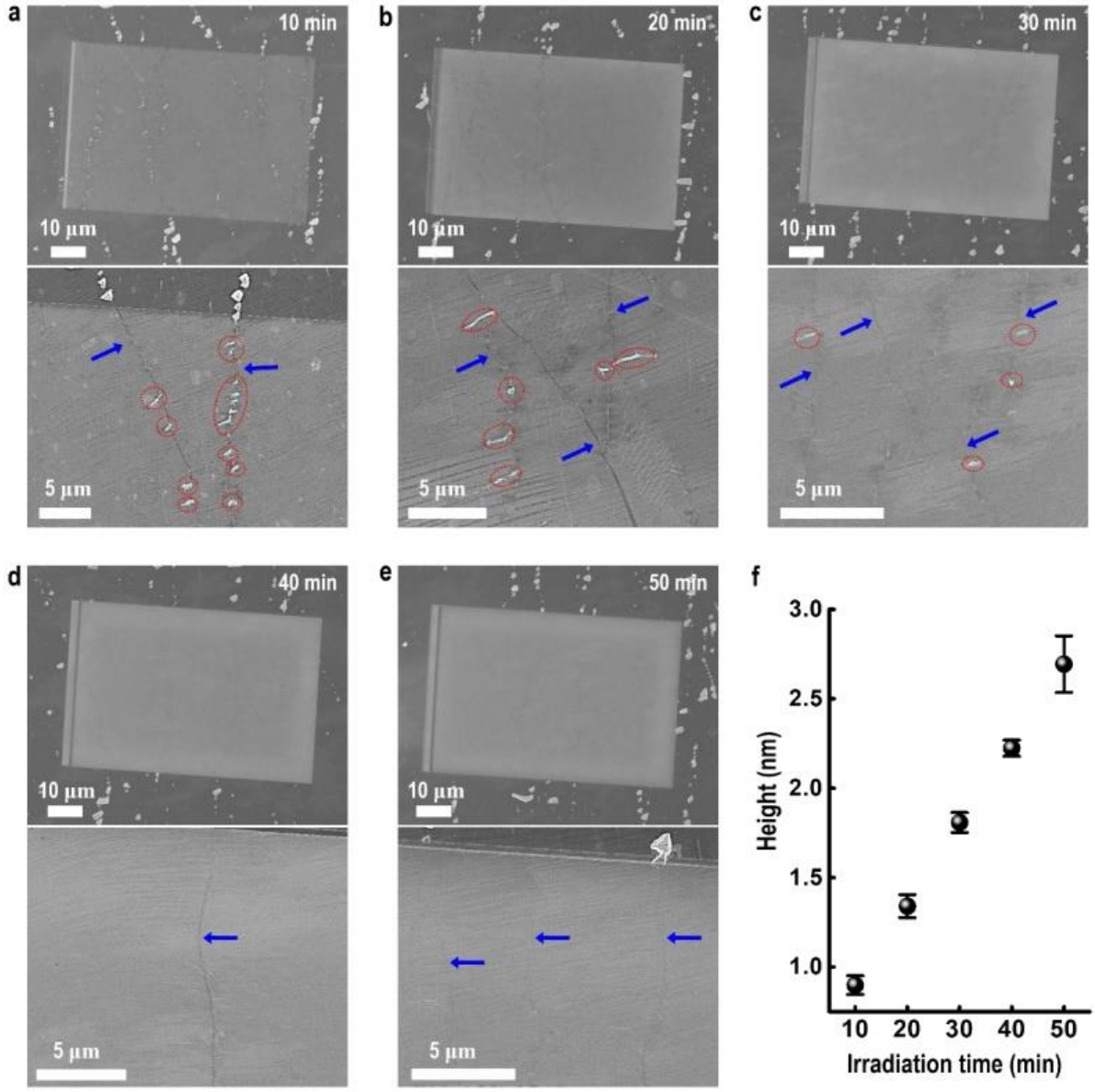

Figure 4.1 (**a**-**e**) Typical SEM images of as-grown graphene irradiated by electron beam for (**a**) 10, (**b**) 20, (**c**) 30, (**d**) 40, and (**e**) 50 min after etching in a 3.7 wt% HCl solution for 10 min. Lower panels in (**a**-**e**) are high-magnification SEM images of the a-C region. Blue arrows and red-dotted circles indicate wrinkles and Cu etch pits, respectively. (**f**) Thickness of a-C layer depending on irradiation time under the same irradiation conditions.

There was an optical microscopy image of graphene/copper sample after selective deposition of amorphous carbon layer by irradiation of electron beam of 10 nA accelerated by 1 kV in Figure 4.2a, and the deposited area was rectangular shaped and a little brown colored. For distinct investigation of amorphous carbon deposited surface, we performed the AFM measurement. The surface of deposited amorphous carbon was coarse and the copper step bunches were a little buried in the layer as shown in Figure 4.2d, e. We also performed the Raman measurement for estimating that the SEM deposition method affect the quality of graphene, and deposition of amorphous carbon layer after polymer supported wet etching transfer onto silicon oxide substrate after treatment of SEM scans. As a result, the amorphous carbon layer was exactly deposited on the scanned area by electron beam in SEM system as shown in Figure 4.3a and b[78].

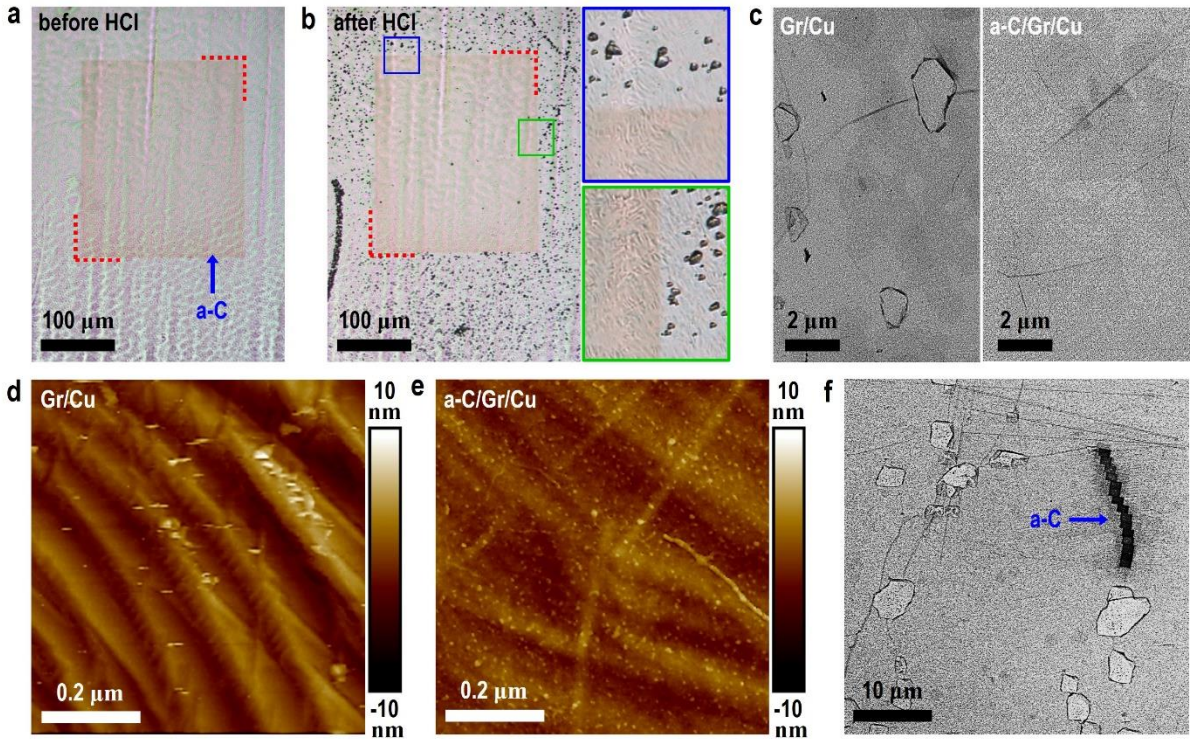

Figure 4.2 (**a,b**) OM images of the as-grown graphene deposited by amorphous carbon layer induced by electron beam before (**a**) and after dipping in an aqueous HCl solution (3.7 wt%) for 20 min (**b**). In **b**, right indicates highly magnified OM images of two squares. (**c-d**) Representative BSE-SEM and AFM images of as-grown graphene without and with a-C layer after the HCl treatment. (**f**) A BSE-SEM image of as-grown graphene after patterning with amorphous carbon along wrinkle of graphene after HCl etching method for 20 min.

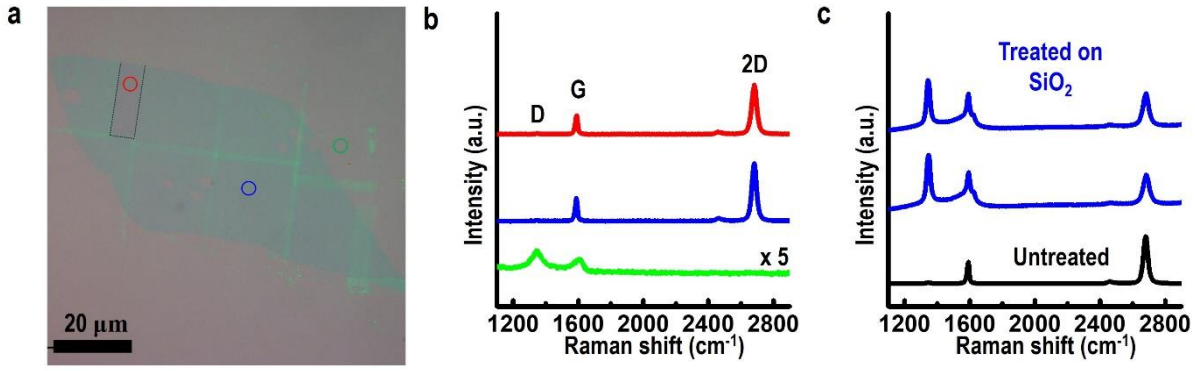

Figure 4.3 OM image of graphene island transferred onto silicon oxide substrate after the electron beam treatment (**b**) Raman spectra from red, blue, and green circles in **a**. (**c**) Raman spectra after the e-beam treatment on a SiO_2/Si, in which the D bands are significantly increased because of the interaction of the energetic electrons with both Gr and SiO_2.

Interestingly, the deposition of amorphous carbon through electron beam induce did not affect the atomic structures of graphene in our scanning condition, when the disorder related D bands of 1350 cm^{-1} by Raman measurement were compared each other for electron beam treated and untreated area as shown in blue and red lines of Figure 4.3b[78]. The copper substrate under graphene layer was acted as buffer for reducing the beam damage to atomic structure of graphene during irradiation process. However, in case of replacing copper substrate to silicon oxide substrate, the D band of Raman measurement was increased after electron beam irradiation process. In previous report, electron irradiated silicon oxide could be dissociated into oxygen atoms with breaking the Si-O bonds because the silicon oxide was unstable to accelerated electron beam[79]. Therefore, the graphene transferred on silicon oxide substrate was affected by electron beam irradiation, because the dissociated oxygen atoms from silicon oxide or water from wet transfer damaged to graphene[80-82]. We also performed the HCl etching method for large area scanning samples composed of amorphous carbon layer, graphene, and copper. Interestingly, there were no copper etching pits in large area scanned regions with SEM after HCl etching method. As shown in Figure 4.2b, the difference between electron beam treated and untreated area was distinctive, as the copper etching pits only occurred at electron beam untreated area, indicating that the deposition of amorphous carbon layer on graphene blocked the various water permeable origins effectively enhancing the impermeability of graphene layer. We also performed the deposition of amorphous carbon along the acceleration voltage of electron beam. As a result, the electron beam accelerated by high voltage over 10 kV did not effectively induce the amorphous carbon layer, so the samples treated by high voltage had copper etching pits on surface after HCl etching

method as shown in Figure 4.4. The reason of this phenomenon is predicted as the quantity of secondary electrons from high voltage irradiation was insufficient for dissociation of carbon contaminants[83, 84]. In addition, the SEM system can be precisely controlled by restriction of scanned area, the amorphous carbon layer can be patterned along the wrinkle of graphene as shown in Figure 4.2f. Therefore, this method will be applicable to production of impermeable graphene layer with restricted area and various devices functionalized by amorphous carbons[85, 86].

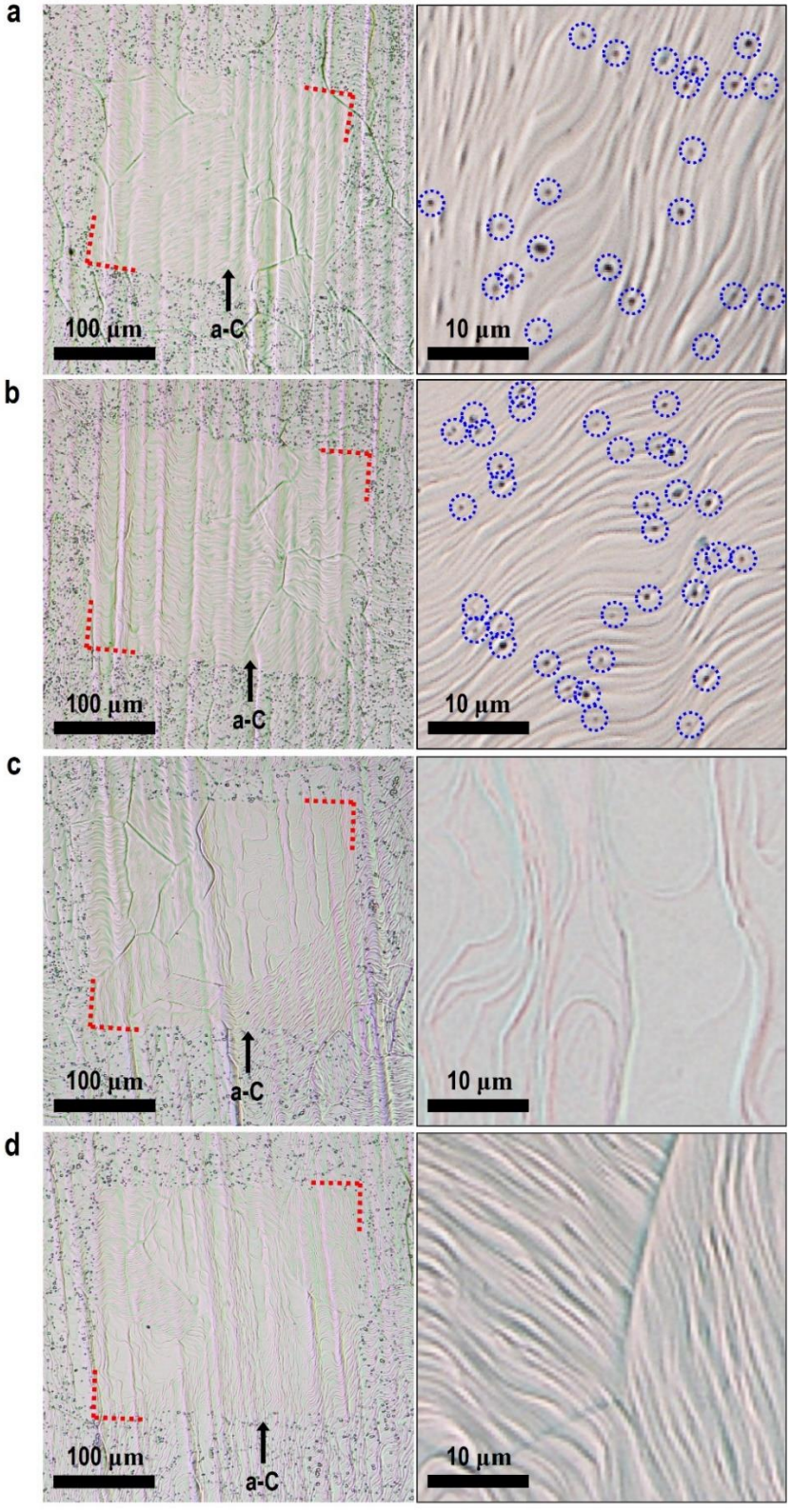

Figure 4.4 OM images of graphene surfaces selectively coated with the a-C layer using the accelerated electron-beam of (**a**) 15, (**b**) 10, (**c**) 5, (**d**) 1 kV, respectively. In **a**-**d**, right indicate representative OM images taken from the region

4.4 Large-area enhancement of CVD graphene water impermeability

Interestingly, the nano-sized water permeable origins were predominantly detected on wrinkles of monolayer graphene as copper etching pits after HCl etching method, rather than on multilayer graphene. We could achieve the multilayer abundant graphene on copper foil by two step growth as previously reported growth technique [87, 88] in Figure 4.5a, and this multilayer abundant samples reduced the density of copper etching pits by half as 1.4×10^6 cm^{-2} after HCl etching method. We observed that the copper etching pits were not located at the wrinkles of multilayer flakes as shown in Figure 4.5b, c, although the wrinkles of monolayer still permitted the water permeation making the copper etching. If the water permeable origins were formed on wrinkles of multilayer graphene by the same reason of monolayer, the copper etching pits should occur at the wrinkles of multilayer flakes because the velocity of water diffusion through permeable origins and along interface of graphitic layers[89-91], as shown in Figure 4.6 which was the data meaning the copper etching pits of multi stacking graphene/graphene/copper samples by transfer was slightly reduced. Therefore, we suggest that the wrinkling process on multilayer graphene does not originate the water permeable origins, because the copper etching pits do not occur at the multilayer area as shown in Figure 4.7. In previous report, the adhesion energy of graphene to substrate is reduced and the strength of graphene is increased as the number of layers is increased[92] . So, the water permeable defects do not occur at multilayer graphene during wrinkling process. In consideration to impermeability of multilayer graphene, the growth of uniform bilayer is a core competence to realize flexible, transparent, and water-impermeable electrodes for organic light emitting diodes.

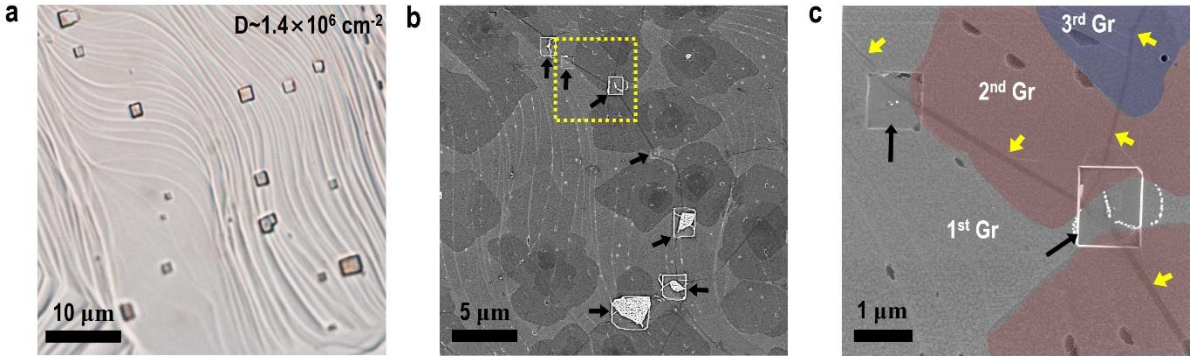

Figure 4.5 (**a**,**b**) OM and SEM images of as-grown graphene with two-step growth after HCl oxidation method (**c**) A highly magnified SEM image of the yellow square in (**b**) with back scattered electron mode. Black and yellow arrows in (**c**) are the copper etching pits and wrinkles

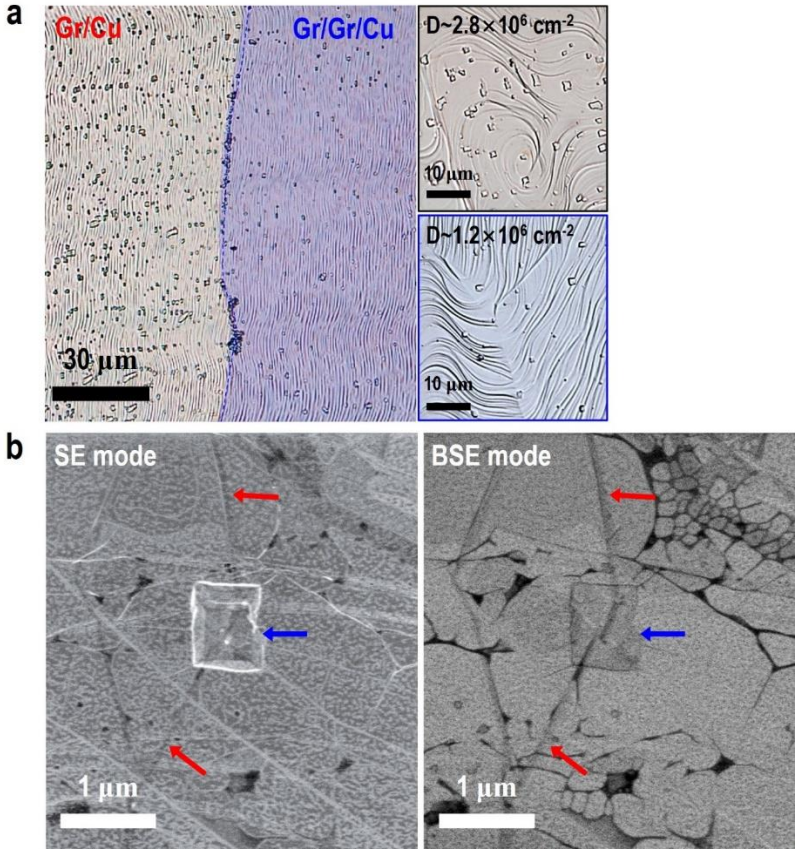

Figure 4.6 (**a**) Representative OM images of boundary between as-grown graphene region and the transferred Gr region onto a Gr/Cu (Gr/Gr/Cu) after dipping 3.7 wt% HCl solution for 20 min. Right indicates high magnification OM images of the Gr/Cu (upper) and Gr/Gr/Cu composites (lower). (**b**) SEM images of the Gr/Gr/Cu composites measured with the SE (left) and BSE mode (right). In (**b**), blue and red arrows indicate a Cu etch pit and wrinkles.

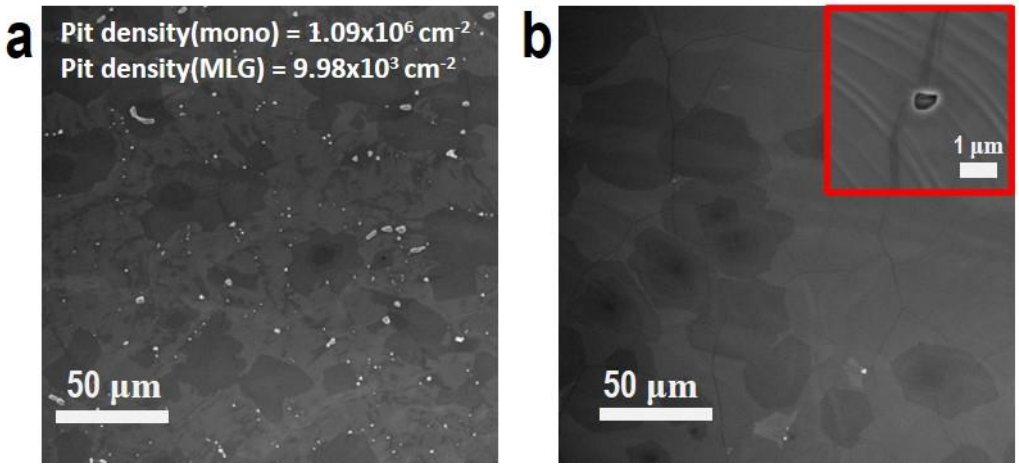

Figure 4.7 A SEM image of as-grown graphene with two-step growth after dipping aqueous HCl solution 2hr (**a**) monolayer dominant part and (**b**) multilayer dominant part.

It is not suitable for massive production of impermeable layer to deposit electron beam induced a-C layer because of selectively scanning deposition. There are some techniques for deposition of large-area amorphous carbon layer. We proceeded a-C layer deposition on as-grown graphene samples for producing a-C/Gr/Cu composites using PECVD and PECS. As show in Figures 4.8, 4.9, amorphous carbon layer was deposited on all over Gr/Cu composites and annealed copper through Ar^+ ion beam induced amorphous carbon layer and tens micrometer-sized etching pits with was formed on the composites after HCl solution dipping for 1 hr. As shown in Figure 4.8b, c, only a-C layer on annealed copper enhanced the water impermeability over 3 min deposition. For 2 min deposition, the density of etching pits was not able to be measured because annealed copper foil was etched overall in Figure 4.8a. Furthermore, a-C layer on graphene grown copper foil was also etched in HCl solution for 1 hr in Figure 4.9. As shown in Figure 4.10, pit density of a-C/Gr/Cu composites was lower than that of a-C/Cu composites by two orders and that of as-grown graphene by three orders. However, raman spectrum of the graphene after PECS deposition had wide D and G bands (~1350 cm^{-1} and ~1580 cm^{-1}) and no 2D peak meaning graphene structure damaged with carbon and argon bombardments. We also used PECVD to deposit a large area amorphous carbon layer. As shown in Figure 4.11, the a-C/Gr/Cu composites deposited by PECVD also had excellent water-impermeability. For deposition of a-C below 3 min, HCl solution was permeable to the composites, but the a-C/Gr/Cu composites with 5min deposition time that the a-C layer had ~5.5 nm thickness was resistant to HCl solution. Regardless of deposition methods as SEM, PECS, or PECVD, the a-C/Gr/Cu composites were impermeable to water when the thickness of a-C layer was over 5 nm because of the size of delamination induced hole

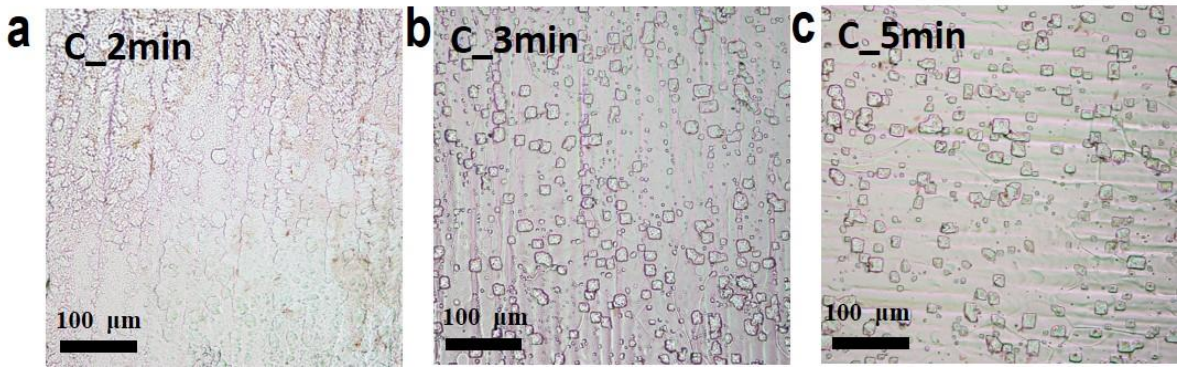

Figure 4.8 OM images of annealed copper deposited with amorphous carbon layer using PECS for (**a**) 2min, (**b**) 3min, and (**c**) 5min.

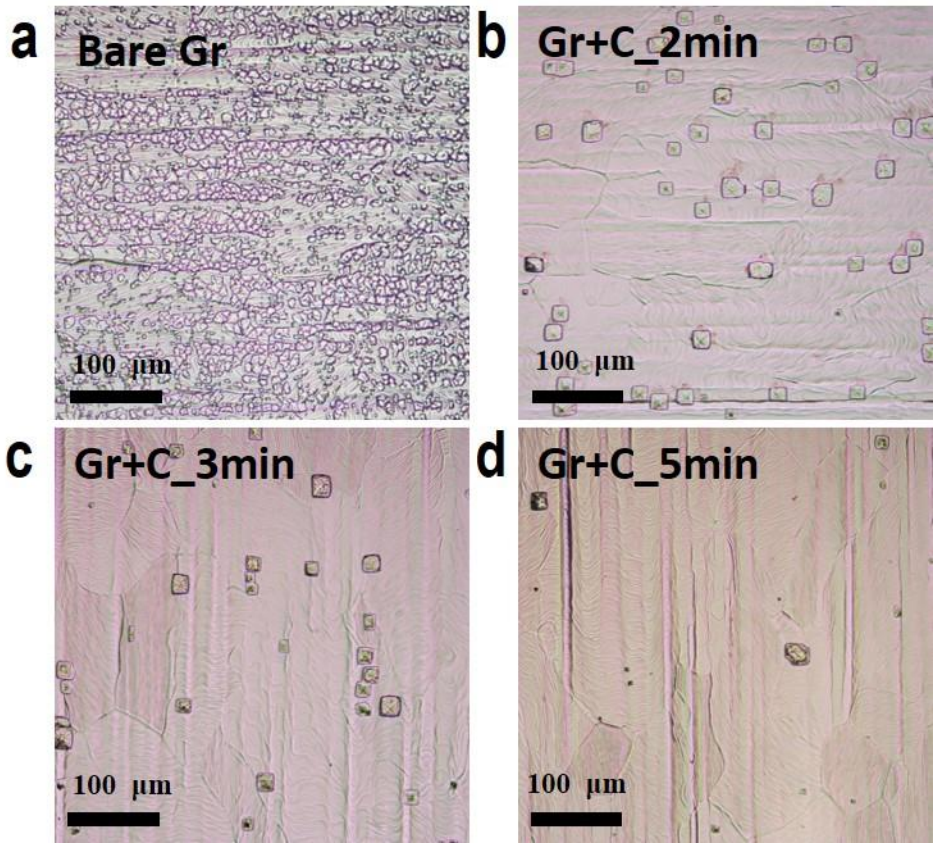

Figure 4.9 Typical OM images of CVD-grown graphene deposited with amorphous carbon layer using PECS for (**a**) 0min, (**b**) 2min, (**c**) 3min, and (**d**) 5min after dipping in 3.7 wt% HCl solution.

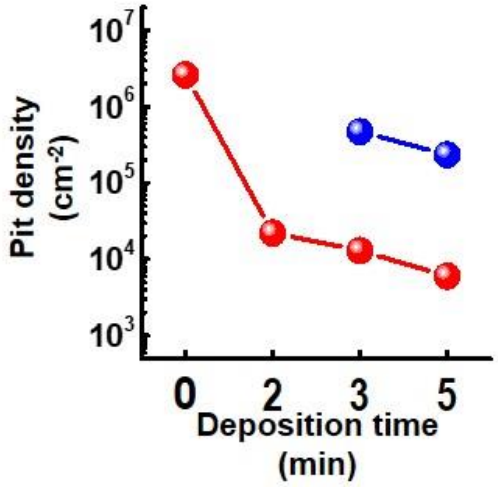

Figure 4.10 Correlation between density of etching pits and deposition time by PECS. Blue and red graphs indicates a-C/annealed Cu and a-C/Gr/Cu composites, respectively

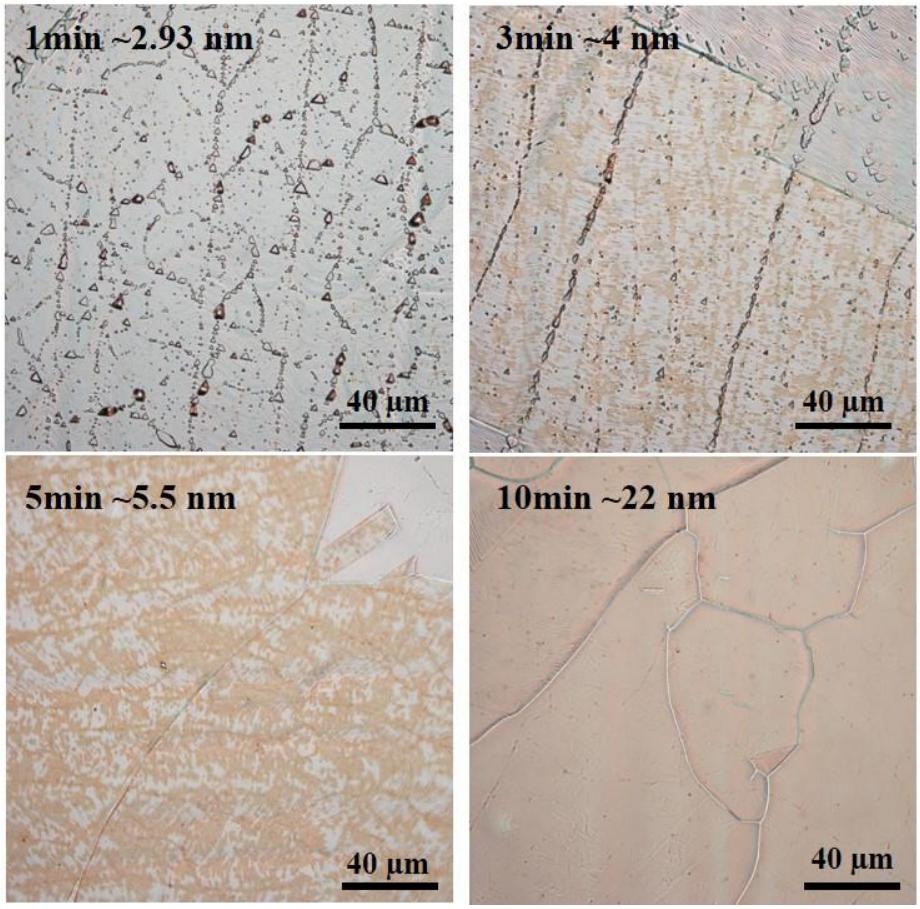

Figure 4.11 OM images of as-grown graphene deposited with amorphous carbon layer using PECVD for (**a**) 1 min, (**b**) 3 min, (**c**) 5 min, and (**d**) 10 min after dipping in 3.7 wt% HCl solution

4.5 Summary and Outlook

In conclusion, we enhanced the impermeability of CVD-grown graphene by deposition of amorphous carbon layer through SEM, PECS, and PECVD and multilayer graphene growth resulting in low density of copper etching pits after HCl solution etching. For blocking 1~3 nm nanosized holes or cracks of graphene, it was necessary that the thickness of a-C layer was over 5 nm. Multilayer graphene also had a promising impermeability to water, and it was expected to flexible and transparent impermeable electrodes. Furthermore, the a-C layer/graphene composite deposited by PECS and PECVD had a poor electrical property with impermeability to water, it was expected to flexible and transparent impermeable substrate in this work. The combination of multilayer graphene and a-C/graphene may be useful for scalable production of a carbon-based flat foam for flexible and transparent organic field-effect transistors.

5. Conclusion and Discussion

As mentioned in previous chapters, CVD grown graphene is vital to industrial fields retaining good quality, scalable production, and reasonable cost. However, the CVD grown graphene has inevitable nature of various defects such as nucleation site, intra-grain boundaries, inter-grain boundaries, and wrinkles hindering application to industrial products. The tools for evaluating quality of graphene and enhancing mechanical, chemical, and electronic properties of graphene are critical techniques to optimizing synthesis of graphene-based composites.

In this dissertation, selective oxygen permeation and oxidation of underlying copper substrate visualize various atomic structural defects of graphene such as nucleation site defects, the intra and inter grain boundaries of graphene domains in large-area CVD grown graphene film. We also confirmed that the major origins for selective oxidation were the dissociation of water molecules in air through experimental and computational results. Through our oxidation method, we could estimate the level of CVD-grown graphene deficiencies with various dependences on the crystallographic orientations of copper substrate, growth conditions of graphene, and the growth rate of the graphene.

Furthermore, there were also nanosized ruptures, cracks and holes on CVD-grown graphene on copper substrate, which acted as water permeable origins. With HCl etching method, it was confirmed that the main origins were located at wrinkles of graphene degrading water impermeability of graphene layer grown by CVD system etching the underlying copper foil. Through high resolution TEM studies, the water permeable defects were directly observed as nanosized ruptures, cracks or holes below 3 nm on wrinkles of CVD-grown graphene. In addition, we confirmed that the water permeable origins on wrinkles of graphene were originated from wrinkling process for releasing compressive stress by detaching of graphene layer from copper step bunches or strain induced by deformation on rough copper step bunches.

Finally, we enhanced the impermeability of CVD-grown graphene by deposition of amorphous carbon layer through SEM, PECS, and PECVD and multilayer graphene growth resulting in low density of copper etching pits after HCl solution etching. We also discovered that it was necessary that the thickness of a-C layer was needed to be over 5 nm for blocking 1~3 nm nanosized holes or cracks of graphene. The a-C layer/graphene composite deposited by PECS and PECVD had a poor electrical property with impermeability to water, and it was expected to flexible and transparent impermeable substrate in this work. Not only the a-C/Gr composites, but also multilayer graphene had a promising impermeability to water, and it was expected to flexible and transparent impermeable electrodes.

These results reveal that multilayer graphene growth was a core technology for reaching thin, flexible, and transparent protective barrier film for blocking permeation through chemical reaction from environment. The facile oxidation method can be applied to measuring the distribution of various intrinsic defects in large-area graphene film and optimizing the growth condition of graphene for

commercialization. Furthermore, the methodology for tracking the water permeable origins will be applied to finding the condition enhancing the impermeability of graphene layer for protecting the large area, flexible, and transparent productions from hazardous as the elimination of copper step bunches and wrinkles in CVD-grown graphene. The combination of multilayer graphene as electrodes and amorphous carbon and graphene composites as substrates will be a key for mass-production of a carbon-based flat foam for flexible and transparent environmentally stable devices.

REFERENCES

1. Berry, V., Impermeability of graphene and its applications. *Carbon* **2013,** *62*, 1-10.
2. Bunch, J. S.; Verbridge, S. S.; Alden, J. S.; van der Zande, A. M.; Parpia, J. M.; Craighead, H. G.; McEuen, P. L., Impermeable atomic membranes from graphene sheets. *Nano Lett* **2008,** *8* (8), 2458-2462.
3. Novoselov, K. S.; Fal'ko, V. I.; Colombo, L.; Gellert, P. R.; Schwab, M. G.; Kim, K., A roadmap for graphene. *Nature* **2012,** *490* (7419), 192-200.
4. Wofford, J. M.; Nie, S.; McCarty, K. F.; Bartelt, N. C.; Dubon, O. D., Graphene islands on Cu foils: the interplay between shape, orientation, and defects. *Nano Lett.* **2010,** *10*, 4890-4896.
5. Tsen, A. W.; Brown, L.; Levendorf, M. P.; Ghahari, F.; Huang, P. Y.; Havener, R. W.; Ruiz-Vargas, C. S.; Muller, D. A.; Kim, P.; Park, J., Tailoring electrical transport across grain boundaries in polycrystalline graphene. *Science* **2012,** *336* (6085), 1143-1146.
6. Banhart, F.; Kotakoski, J.; Krasheninnikov, A. V., Structural defects in graphene. *ACS Nano* **2011,** *5* (1), 26-41.
7. Kim, D. W.; Kim, Y. H.; Jeong, H. S.; Jung, H. T., Direct visualization of large-area graphene domains and boundaries by optical birefringency. *Nat Nanotechnol* **2011,** *7* (1), 29-34.
8. Duong, D. L.; Han, G. H.; Lee, S. M.; Gunes, F.; Kim, E. S.; Kim, S. T.; Kim, H.; Ta, Q. H.; So, K. P.; Yoon, S. J.; Chae, S. J.; Jo, Y. W.; Park, M. H.; Chae, S. H.; Lim, S. C.; Choi, J. Y.; Lee, Y. H., Probing graphene grain boundaries with optical microscopy. *Nature* **2012,** *490* (7419), 235-239
9. Kim, K.; Lee, H. B.; Johnson, R. W.; Tanskanen, J. T.; Liu, N.; Kim, M. G.; Pang, C.; Ahn, C.; Bent, S. F.; Bao, Z., Selective metal deposition at graphene line defects by atomic layer deposition. *Nat Commun* **2014,** *5*, 4781.
10. Hofmann, M.; Shin, Y. C.; Hsieh, Y.-P.; Dresselhaus, M. S.; Kong, J., A facile tool for the characterization of two-dimensional materials grown by chemical vapor deposition. *Nano Research* **2012,** *5* (7), 504-511.
11. Seo, T. H.; Lee, S.; Cho, H.; Chandramohan, S.; Suh, E. K.; Lee, H. S.; Bae, S. K.; Kim, S. M.; Park, M.; Lee, J. K.; Kim, M. J., Tailored CVD graphene coating as a transparent and flexible gas barrier. *Sci Rep* **2016,** *6*, 24143.
12. Chen, X.; Zhang, L.; Chen, S., Large area CVD growth of graphene. *Synthetic Metals* **2015,** *210*, 95-108.
13. Novoselov, K. S.; Geim, A. K.; Morozov, S. V.; Jiang, D.; Zhang, Y.; Dubonos, S. V.; Grigorieva, I. V.; Firsov, A. A., Electric field effect in atomically thin carbon films. *Science* **2004,** *306* (5696), 666-669.

14. Lee, C.; Wei, X. D.; Kysar, J. W.; Hone, J., Measurement of the elastic properties and intrinsic strength of monolayer graphene. *Science* **2008,** *321* (5887), 385-388.
15. Balandin, A. A.; Ghosh, S.; Bao, W.; Calizo, I.; Teweldebrhan, D.; Miao, F.; Lau, C. N., Superior Thermal Conductivity of Single-Layer Graphene. *Nano Letters* **2008,** *8* (3), 902-907.
16. Nair, R. R.; Blake, P.; Grigorenko, A. N.; Novoselov, K. S.; Booth, T. J.; Stauber, T.; Peres, N. M. R.; Geim, A. K., Fine Structure Constant Defines Visual Transparency of Graphene. *Science* **2008,** *320* (5881), 1308.
17. Akturk, A.; Goldsman, N., Electron transport and full-band electron-phonon interactions in graphene. *J. Appl. Phys.* **2008,** *103* (5), 053702.
18. Sreeprasad, T. S.; Berry, V., How Do the Electrical Properties of Graphene Change with its Functionalization? *Small* **2013,** *9* (3), 341-350.
19. Hernandez, Y.; Nicolosi, V.; Lotya, M.; Blighe, F. M.; Sun, Z.; De, S.; McGovern, I. T.; Holland, B.; Byrne, M.; Gun'Ko, Y. K.; Boland, J. J.; Niraj, P.; Duesberg, G.; Krishnamurthy, S.; Goodhue, R.; Hutchison, J.; Scardaci, V.; Ferrari, A. C.; Coleman, J. N., High-yield production of graphene by liquid-phase exfoliation of graphite. *Nature Nanotechnology* **2008,** *3* (9), 563-568.
20. Forbeaux, I.; Themlin, J. M.; Debever, J. M., Heteroepitaxial graphite on 6*H*-SiC(0001): Interface formation through conduction-band electronic structure. *Physical Review B* **1998,** *58* (24), 16396-16406.
21. Li, X.; Cai, W.; An, J.; Kim, S.; Nah, J.; Yang, D.; Piner, R.; Velamakanni, A.; Jung, I.; Tutuc, E.; Banerjee, S. K.; Colombo, L.; Ruoff, R. S., Large-Area Synthesis of High-Quality and Uniform Graphene Films on Copper Foils. *Science* **2009,** *324* (5932), 1312.
22. Reina, A.; Jia, X.; Ho, J.; Nezich, D.; Son, H.; Bulovic, V.; Dresselhaus, M. S.; Kong, J., Large Area, Few-Layer Graphene Films on Arbitrary Substrates by Chemical Vapor Deposition. *Nano Letters* **2009,** *9* (1), 30-35.
23. Chu, J. H.; Kwak, J.; Kim, S.-D.; Lee, M. J.; Kim, J. J.; Park, S.-D.; Choi, J.-K.; Ryu, G. H.; Park, K.; Kim, S. Y.; Kim, J. H.; Lee, Z.; Kim, Y.-W.; Kwon, S.-Y., Monolithic graphene oxide sheets with controllable composition. *Nature Communications* **2014,** *5* (1), 3383.
24. Regan, W.; Alem, N.; Alemán, B.; Geng, B.; Girit, Ç.; Maserati, L.; Wang, F.; Crommie, M.; Zettl, A., A direct transfer of layer-area graphene. *Applied Physics Letters* **2010,** *96* (11), 113102.
25. Kresse, G.; Furthmüller, J., Efficiency of ab-initio total energy calculations for metals and semiconductors using a plane-wave basis set. *Computational Materials Science* **1996,** *6* (1), 15-50.
26. Kresse, G.; Furthmüller, J., Efficiency of ab-initio total energy calculations for metals and semiconductors using a plane-wave basis set. *Computational Materials Science* **1996,** *6* (1), 15-50.
27. Vanderbilt, D., Soft self-consistent pseudopotentials in a generalized eigenvalue formalism. *Phys. Rev. B* **1990,** *41*, 7892.

28. Ceperley, D. M.; Alder, B. J., Ground state of the electron gas by a stochastic method. *Phys. Rev. Lett.* **1980,** *45*.
29. Mills, G.; Jonsson, H.; Schenter, G. K., Reversible work transition state theory: application to dissociative adsorption of hydrogen. *Surf. Sci.* **1995,** *324*, 566.
30. Barinov, A.; Malcioğlu, O. B.; Fabris, S.; Sun, T.; Gregoratti, L.; Dalmiglio, M.; Kiskinova, M., Initial Stages of Oxidation on Graphitic Surfaces: Photoemission Study and Density Functional Theory Calculations. *The Journal of Physical Chemistry C* **2009,** *113* (21), 9009-9013.
31. Platzman, I.; Brener, R.; Haick, H.; Tannenbaum, R., Oxidation of polycrystalline copper thin films at ambient conditions. *J. Phys. Chem. C* **2008,** *112*, 1101-1108.
32. Li, X.; Magnuson, C. W.; Venugopal, A.; An, J.; Suk, J. W.; Han, B.; Borysiak, M.; Cai, W.; Velamakanni, A.; Zhu, Y.; Fu, L.; Vogel, E. M.; Voelkl, E.; Colombo, L.; Ruoff, R. S., Graphene Films with Large Domain Size by a Two-Step Chemical Vapor Deposition Process. *Nano Letters* **2010,** *10* (11), 4328-4334.
33. Choi, J.-K.; Kwak, J.; Park, S.-D.; Yun, H. D.; Kim, S.-Y.; Jung, M.; Kim, S. Y.; Park, K.; Kang, S.; Kim, S.-D.; Park, D.-Y.; Lee, D.-S.; Hong, S.-K.; Shin, H.-J.; Kwon, S.-Y., Growth of Wrinkle-Free Graphene on Texture-Controlled Platinum Films and Thermal-Assisted Transfer of Large-Scale Patterned Graphene. *ACS Nano* **2015,** *9* (1), 679-686.
34. Zeng, M.; Tan, L.; Wang, L.; Mendes, R. G.; Qin, Z.; Huang, Y.; Zhang, T.; Fang, L.; Zhang, Y.; Yue, S.; Rümmeli, M. H.; Peng, L.; Liu, Z.; Chen, S.; Fu, L., Isotropic Growth of Graphene toward Smoothing Stitching. *ACS Nano* **2016,** *10* (7), 7189-7196.
35. Zhu, Y.; Mimura, K.; Lim, J. W.; Jiang, M. I., Brief review of oxidation kinetics of copper at 350 ºC to 1050 ºC. *Metall. Mater. Trans. A* **2006,** *37A*, 1231-1237.
36. Yuan, L.; Wang, Y.; Mema, R.; Zhou, G., Driving force and growth mechanism for spontaneous oxide nanowire formation during the thermal oxidation of metals. *Acta Mater.* **2011,** *59*, 2491-2500.
37. Lee, S. K.; Hsu, H. C.; Tuan, W. H., Oxidation behavior of copper at a temperature below 300 ºC and the methodology for passivation. *Mater. Res.* **2016,** *19*, 51-56.
38. Kurra, N.; Bhadram, V. S.; Narayana, C.; Kulkarni, G. U., Few layer graphene to graphitic films: infrared photoconductive versus bolometric response. *Nanoscale* **2013,** *5*, 381-389.
39. Rogge, P. C.; Thürmer, K.; Foster, M. E.; McCarty, K. F.; Dubon, O. D.; Bartelt, N. C., Real-time observation of epitaxial graphene domain reorientation. *Nature Communications* **2015,** *6* (1), 6880.
40. Kim, S.-Y.; Kwak, J.; Chu, J. H.; Kim, J. B.; Kim, S. Y.; Park, K.; Kwon, S.-Y., Controllable Synthesis of Graphene-Encapsulated Low-Dimensional Nanocomposites. *Advanced Materials Interfaces* **2015,** *2* (11), 1500112.
41. Zhu, W.; Low, T.; Perebeinos, V.; Bol, A. A.; Zhu, Y.; Yan, H.; Tersoff, J.; Avouris, P., Structure and Electronic Transport in Graphene Wrinkles. *Nano Letters* **2012,** *12* (7), 3431-3436.

42. Chihara, K.; Suzuki, M.; Kawazoe, K., Interpretation for micropore diffusivities of gases in molecular-sieving carbon. *J. Colloid Interf. Sci.* **1978,** *64*, 584-587.
43. Feng, X. F.; Maier, S.; Salmeron, M., Water splits epitaxial graphene and intercalates. *J. Am. Chem. Soc.* **2012,** *134*, 5662-5668.
44. Xu, Z.; Ao, Z.; Chu, D.; Younis, A.; Li, C. M.; Li, S., Reversible Hydrophobic to Hydrophilic Transition in Graphene via Water Splitting Induced by UV Irradiation. *Scientific Reports* **2014,** *4* (1), 6450.
45. Kwon, S.-Y.; Ren, Z.; Sun, Q.; Han, J.; Kim, Y.-W.; Yoon, E.; Kong, B. H.; Cho, H. K.; Kim, I.-J.; Cheong, H., Observation of oxide precipitates in InN nanostructures. *Applied Physics Letters* **2007,** *91* (23), 234102.
46. Nakamura, J.; Rodriguez, J. A.; Campbell, C. T., Does CO2 dissociatively adsorb on Cu surfaces? *J. Phys. Condens. Matter.* **1989,** *1*, SB149-SB160.
47. Mehmood, F.; Pachter, R.; Lu, W. J.; Boeckl, J. J., Adsorption and diffusion of oxygen on single-layer graphene with topological defects. *J. Phys. Chem. C* **2013,** *117*, 10366-10374.
48. Wang, B.; Puzyrev, Y. S.; Pantelides, S. T., Enhanced chemical reactions of oxygen at grain boundaries in polycrystalline graphene. *Polyhedron* **2013,** *64*, 158-162.
49. Walter, A. L.; Nie, S.; Bostwick, A.; Kim, K. S.; Moreschini, L.; Chang, Y. J.; Innocenti, D.; Horn, K.; McCarty, K. F.; Rotenberg, E., Electronic structure of graphene on single-crystal copper substrates. *Physical Review B* **2011,** *84* (19), 195443.
50. Suarez, A. M.; Radovic, L. R.; Bar-Ziv, E.; Sofo, J. O., Gate-voltage control of oxygen diffusion on graphene. *Phys. Rev. Lett.* **2011,** *106*, 146802.
51. Boukhvalov, D. W., Modeling of hydrogen and hydroxyl group migration on graphene. *Phys. Chem. Chem. Phys.* **2010,** *12*, 15367-15371.
52. Gurel, H. H. a., S., Enhanced reduction of graphene oxide by means of charging and electric fields applied to hydroxyl groups. *J. Phys.: Condens. Matter.* **2013,** *25*, 435304.
53. Raynaud, G. M.; Rapp, R. A., In situ observation of whiskers, pyramids and pits during the high-temperature oxidation of metals. *Oxid. Metals* **1984,** *21*, 89-102.
54. Kurasch, S.; Meyer, J. C.; Künzel, D.; Groß, A.; Kaiser, U., Simulation of bonding effects in HRTEM images of light element materials. *Beilstein Journal of Nanotechnology* **2011,** *2*, 394-404.
55. Robertson, A. W.; Warner, J. H., Atomic resolution imaging of graphene by transmission electron microscopy. *Nanoscale* **2013,** *5*, 4079.
56. Kosynkin, D. V.; Higginbotham, A. L.; Sinitskii, A.; Lomeda, J. R.; Dimiev, A.; Price, B. K.; Tour, J. M., Longitudinal unzipping of carbon nanotubes to form graphene nanoribbons. *Nature* **2009,** *458* (7240), 872-U5.

57. Hsieh, Y. P.; Hofmann, M.; Chang, K. W.; Jhu, J. G.; Li, Y. Y.; Chen, K. Y.; Yang, C. C.; Chang, W. S.; Chen, L. C., Complete Corrosion Inhibition through Graphene Defect Passivation. *Acs Nano* **2014,** *8* (1), 443-448.
58. Boutilier, M. S. H.; Sun, C. Z.; O'Hern, S. C.; Au, H.; Hadjiconstantinou, N. G.; Karnik, R., Implications of Permeation through Intrinsic Defects in Graphene on the Design of Defect-Tolerant Membranes for Gas Separation. *Acs Nano* **2014,** *8* (1), 841-849.
59. O'Hern, S. C.; Stewart, C. A.; Boutilier, M. S. H.; Idrobo, J. C.; Bhaviripudi, S.; Das, S. K.; Kong, J.; Laoui, T.; Atieh, M.; Karnik, R., Selective Molecular Transport through Intrinsic Defects in a Single Layer of CVD Graphene. *Acs Nano* **2012,** *6* (11), 10130-10138.
60. Cakir, O., Copper etching with cupric chloride and regeneration of waste etchant. *J. Mater. Process. Technol.* **2006,** *175* (1-3), 63-68.
61. Li, X. S.; Colombo, L.; Ruoff, R. S., Synthesis of Graphene Films on Copper Foils by Chemical Vapor Deposition. *Advanced Materials* **2016,** *28* (29), 6247-6252.
62. Kim, S.-Y.; Kwak, J.; Kim, J. H.; Lee, J.-U.; Jo, Y.; Kim, S. Y.; Cheong, H.; Lee, Z.; Kwon, S.-Y., Substantial improvements of long-term stability in encapsulation-free WS 2 using highly interacting graphene substrate. *2D Materials* **2016,** *4* (1), 011007.
63. Kwak, J.; Jo, Y.; Park, S. D.; Kim, N. Y.; Kim, S. Y.; Shin, H. J.; Lee, Z.; Kim, S. Y.; Kwon, S. Y., Oxidation behavior of graphene-coated copper at intrinsic graphene defects of different origins. *Nature Communications* **2017,** *8*, 12.
64. Ly, T. H.; Duong, D. L.; Ta, Q. H.; Yao, F.; Vu, Q. A.; Jeong, H. Y.; Chae, S. H.; Lee, Y. H., Nondestructive Characterization of Graphene Defects. *Advanced Functional Materials* **2013,** *23* (41), 5183-5189.
65. Jiao, L. Y.; Zhang, L.; Wang, X. R.; Diankov, G.; Dai, H. J., Narrow graphene nanoribbons from carbon nanotubes. *Nature* **2009,** *458* (7240), 877-880.
66. Ma, L.; Wang, J. L.; Ding, F., Strain-Induced Orientation-Selective Cutting of Graphene into Graphene Nanoribbons on Oxidation. *Angew. Chem.-Int. Edit.* **2012,** *51* (5), 1161-1164.
67. N'Diaye, A. T.; van Gastel, R.; Martinez-Galera, A. J.; Coraux, J.; Hattab, H.; Wall, D.; zu Heringdorf, F. J. M.; Horn-von Hoegen, M.; Gomez-Rodriguez, J. M.; Poelsema, B.; Busse, C.; Michely, T., In situ observation of stress relaxation in epitaxial graphene. *New J. Phys.* **2009,** *11*, 14.
68. Hattab, H.; N'Diaye, A. T.; Wall, D.; Klein, C.; Jnawali, G.; Coraux, J.; Busse, C.; van Gastel, R.; Poelsema, B.; Michely, T.; Heringdorf, F.; Horn-von Hoegen, M., Interplay of Wrinkles, Strain, and Lattice Parameter in Graphene on Iridium. *Nano Letters* **2012,** *12* (2), 678-682.
69. Das, S.; Lahiri, D.; Lee, D. Y.; Agarwal, A.; Choi, W., Measurements of the adhesion energy of graphene to metallic substrates. *Carbon* **2013,** *59*, 121-129.

70. Yoon, T.; Shin, W. C.; Kim, T. Y.; Mun, J. H.; Kim, T. S.; Cho, B. J., Direct Measurement of Adhesion Energy of Monolayer Graphene As-Grown on Copper and Its Application to Renewable Transfer Process. *Nano Letters* **2012,** *12* (3), 1448-1452.
71. Zhang, P.; Ma, L. L.; Fan, F. F.; Zeng, Z.; Peng, C.; Loya, P. E.; Liu, Z.; Gong, Y. J.; Zhang, J. N.; Zhang, X. X.; Ajayan, P. M.; Zhu, T.; Lou, J., Fracture toughness of graphene. *Nature Communications* **2014,** *5*, 7.
72. Lim, H.; Jung, J.; Ruoff, R. S.; Kim, Y., Structurally driven one-dimensional electron confinement in sub-5-nm graphene nanowrinkles. *Nature Communications* **2015,** *6*, 6.
73. Schaer, M.; Nuesch, F.; Berner, D.; Leo, W.; Zuppiroli, L., Water vapor and oxygen degradation mechanisms in organic light emitting diodes. *Advanced Functional Materials* **2001,** *11* (2), 116-121.
74. Yang, H. C.; Yang, L.; Ling, M. M.; Lastella, S.; Gandhi, D. D.; Ramanath, G.; Bao, Z. N.; Ryu, C. V., Aging Susceptibility of Terrace-Like Pentacene Films. *Journal of Physical Chemistry C* **2008,** *112* (42), 16161-16165.
75. Seo, H. K.; Park, M. H.; Kim, Y. H.; Kwon, S. J.; Jeong, S. H.; Lee, T. W., Laminated Graphene Films for Flexible Transparent Thin Film Encapsulation. *ACS Appl. Mater. Interfaces* **2016,** *8* (23), 14725-14731.
76. Koops, H. W. P.; Kretz, J.; Rudolph, M.; Weber, M.; Dahm, G.; Lee, K. L., Characterization and Application of Materials Grown by Electron-Beam-Induced Deposition. *Jpn. J. Appl. Phys. Part 1 - Regul. Pap. Short Notes Rev. Pap.* **1994,** *33* (12B), 7099-7107.
77. Luo, J. S.; Sung, C. S.; Hsu, W. S.; Huang, L. Y.; Russell, J. D., Electron beam induced carbon deposition using hydrocarbon contamination for XTEM analysis. *Microelectronics Reliability* **2010,** *50* (9-11), 1446-1450.
78. Ferrari, A. C.; Robertson, J., Resonant Raman spectroscopy of disordered, amorphous, and diamondlike carbon. *Physical Review B* **2001,** *64* (7), 13.
79. Nonaka, H.; Ichimura, S.; Arai, K.; Legressus, C., Defect formation observed by AES in a-SiO_2 films prepared by photochemical vapour deposition. *Surf. Interface Anal.* **1990,** *16* (1-12), 435-439.
80. Fujita, D.; Homma, T., Surface precipitation of graphite layers on carbon-doped nickel and their stabilization effect against chemisorption and initial oxidation. *Surf. Interface Anal.* **1992,** *19* (1-12), 430-434.
81. Xu, M. S.; Fujita, D.; Hanagata, N., Monitoring electron-beam irradiation effects on graphenes by temporal Auger electron spectroscopy. *Nanotechnology* **2010,** *21* (26), 7.

82. Childres, I.; Jauregui, L. A.; Foxe, M.; Tian, J. F.; Jalilian, R.; Jovanovic, I.; Chen, Y. P., Effect of electron-beam irradiation on graphene field effect devices. *Applied Physics Letters* **2010,** *97* (17), 3.
83. Lin, Y. H.; Joy, D. C., A new examination of secondary electron yield data. *Surf. Interface Anal.* **2005,** *37* (11), 895-900.
84. Rykaczewski, K.; White, W. B.; Fedorov, A. G., Analysis of electron beam induced deposition (EBID) of residual hydrocarbons in electron microscopy. *J. Appl. Phys.* **2007,** *101* (5), 12.
85. Krasheninnikov, A. V.; Banhart, F., Engineering of nanostructured carbon materials with electron or ion beams. *Nat. Mater.* **2007,** *6* (10), 723-733.
86. Raghuveer, M. S.; Kumar, A.; Frederick, M. J.; Louie, G. P.; Ganesan, P. G.; Ramanath, G., Site-selective functionalization of carbon nanotubes. *Advanced Materials* **2006,** *18* (5), 547-+.
87. Liu, L. X.; Zhou, H. L.; Cheng, R.; Yu, W. J.; Liu, Y.; Chen, Y.; Shaw, J.; Zhong, X.; Huang, Y.; Duan, X. F., High-Yield Chemical Vapor Deposition Growth of High-Quality Large-Area AB-Stacked Bilayer Graphene. *Acs Nano* **2012,** *6* (9), 8241-8249.
88. Zhou, F.; Li, Z.; Shenoy, G. J.; Li, L.; Liu, H., Enhanced room-temperature corrosion of copper in the presence of graphene. *ACS Nano* **2013,** *7*.
89. Suk, M. E.; Aluru, N. R., Water Transport through Ultrathin Graphene. *J. Phys. Chem. Lett.* **2010,** *1* (10), 1590-1594.
90. Nair, R. R.; Wu, H. A.; Jayaram, P. N.; Grigorieva, I. V.; Geim, A. K., Unimpeded Permeation of Water Through Helium-Leak-Tight Graphene-Based Membranes. *Science* **2012,** *335* (6067), 442-444.
91. Celebi, K.; Buchheim, J.; Wyss, R. M.; Droudian, A.; Gasser, P.; Shorubalko, I.; Kye, J. I.; Lee, C.; Park, H. G., Ultimate Permeation Across Atomically Thin Porous Graphene. *Science* **2014,** *344* (6181), 289-292.
92. He, Y.; Chen, W. F.; Yu, W. B.; Ouyang, G.; Yang, G. W., Anomalous interface adhesion of graphene membranes. *Scientific Reports* **2013,** *3*, 7.

ACADEMIC ACHIEVEMENTS

Publications

1. Kwak, J.; **Jo, Y.**; Park, S. -D.; Kim, N. Y.; Kim, S. -Y.; Shin, H. -J.; Lee, Z.; Kim, S. Y.; Kwon, S. -Y. Oxidation behavior of graphene-coated copper at intrinsic graphene defects of different origins. *Nature Communications* **2017,** *8*, 1549.
2. Kwak, J.; **Jo, Y.**; Song, S.; Kim, J. H.; Kim, S. -Y.; Lee, J. -U.; Lee, S.; Park, J.; Kim, K.; Lee, G. D.; Yoo, J. -W.; Kim, S. Y.; Kong, Y. M.; Lee, G. -H.; Lee, W. -G.; Park, J.; Xu, X.; Cheong, H.; Yoon, E.; Lee, Z.; Kwon, S. -Y. Single-Crystalline Nanobelts Composed of Transition Metal Ditellurides. *Advanced Materials* **2018,** *30*, 1707260.
3. Kwak, J.; Kim, S.-Y.; **Jo, Y.**; Kim, N. Y.; Kim, S. Y.; Lee, Z.; Kwon, S.-Y. Unraveling the Water Impermeability Discrepancy in CVD-Grown Graphene. *Advanced Materials* **2018,** *30*, 1800022.
4. Kim, S. -Y.; Kwak, J.; Kim, J. H.; **Jo, Y.**; Kim, S. Y.; Cheong, H.; Lee, Z.; Kwon, S. -Y. Substantial improvements of long-term stability in encapsulation-free WS_2 using highly interacting graphene substrate. *2D Materials* **2016,** *4*, 011007.
5. Kim, S.-Y.; Kim, J. H.; Lee, S.; Kwak, J.; **Jo, Y.**; Yoon, E.; Lee, G.-D.; Lee, Z.; Kwon, S.-Y., The impact of substrate surface defects on the properties of two-dimensional van der Waals heterostructures. *Nanoscale* **2018,** *10* (40), 19212-19219.
6. Sim, Y.; Kwak, J.; Kim, S.-Y.; **Jo, Y.**; Kim, S.; Kim, S. Y.; Kim, J. H.; Lee, C.-S.; Jo, J. H.; Kwon, S.-Y., Formation of 3D graphene–Ni foam heterostructures with enhanced performance and durability for bipolar plates in a polymer electrolyte membrane fuel cell. *Journal of Materials Chemistry A* **2018,** *6* (4), 1504-1512.
7. Song, S.; Kim, S.-Y.; Kwak, J.; **Jo, Y.**; Kim, J. H.; Lee, J. H.; Lee, J.-U.; Kim, J. U.; Yun, H. D.; Sim, Y.; Wang, J.; Lee, D. H.; Seok, S.-H.; Kim, T.-i.; Cheong, H.; Lee, Z.; Kwon, S.-Y., Electrically Robust Single-Crystalline WTe2 Nanobelts for Nanoscale Electrical Interconnects. *Advanced Science* **2019,** *6* (3), 1801370.

Patents

1. Kwon, S.-Y.; Kwak, J.; **Jo, Y.;** Song, S.; Lee, Z.; Lee, J., 전이금속 칼코젠 화합물의 제조 방법. Korean Patent application number : 10-1993365
2. Kwon, S.-Y.; Song, S.; Kwak, J.; Kim, S. -Y.; **Jo, Y.;** Lee, J., 일차원 전이금속 칼코젠 화합물 및 일차원 전이금속 칼코젠 화합물 배선, 및 이를 포함하는 전자 장치. Korean Patent application number : 10-2023045

Conferences

1. **Jo, Y.**; Kwak, J.; Park, S. -D.; Kim, N. Y.; Kim, S. -Y.; Lee, Z.; Kim, S. Y.; Kwon, S. -Y., Facile Observation of Intrinsic CVD Graphene Defects through Selective Oxygen Transport. *MRS-K* **2016**.
2. **Jo, Y.**; Kwak, J.; Park, S. -D.; Kim, N. Y.; Kim, S. -Y.; Lee, Z.; Kim, S. Y.; Kwon, S. -Y., Oxidation behavior of intrinsic graphene defects of different origins on copper. *ICAMD* **2017**.
3. **Jo, Y.**; Kwak, J.; Park, S. -D.; Kim, N. Y.; Kim, S. -Y.; Lee, Z.; Kim, S. Y.; Kwon, S. -Y., Facile Observation of Intrinsic CVD Graphene Defects through Selective Oxygen Transport. *KSLOE* **2018,** *Spring meeting.*
4. **Jo, Y.**; Kwak, J.; Park, S. -D.; Kim, N. Y.; Kim, S. -Y.; Lee, Z.; Kim, S. Y.; Kwon, S. -Y., Ambient air oxidation behavior of intrinsic graphene defects for different origins on copper. *The Korean Ceramic Society* **2018,** *Spring meeting***.**
5. **Jo, Y.**; Kwak, J.; Park, S. -D.; Kim, N. Y.; Kim, S. -Y.; Lee, Z.; Kim, S. Y.; Kwon, S. -Y., Air oxidation behavior of intrinsic graphene defects for different origins on copper. *KSLOE* **2018,** *Fall meeting.* **Award.**
6. **Jo, Y.**; Kwak, J.; Park, S. -D.; Kim, N. Y.; Kim, S. -Y.; Lee, Z.; Kim, S. Y.; Kwon, S. -Y., Oxidation behavior of graphene-coated copper at intrinsic graphene defects with different origins. *The Korean Ceramic Society* **2018,** *Fall meeting.*
7. **Jo, Y.**; Kwak, J.; Park, S. -D.; Kim, N. Y.; Kim, S. -Y.; Shin, H. -J.; Lee, Z.; Kim, S. Y.; Kwon, S. -Y., Selective oxidation phenomenon of graphene-coated copper through graphene defects. *KCS* **2019**.
8. **Jo, Y.**; Kwak, J.; Park, S. -D.; Kim, N. Y.; Kim, S. -Y.; Shin, H. -J.; Lee, Z.; Kim, S. Y.; Kwon, S. -Y., Oxidation behavior of intrinsic graphene defects of different origins on copper. *ICAE* **2019**.
9. **Jo, Y.**; Kwak, J.; Park, S. -D.; Kim, N. Y.; Kim, S. -Y.; Shin, H. -J.; Lee, Z.; Kim, S. Y.; Kwon, S. -Y., Selective Oxidation Behavior of Various Intrinsic Graphene Defects in Graphene-Coated Cu. *ICAMD* **2019**.
10. **Jo, Y.**; Kwak, J.; Park, S. -D.; Kim, N. Y.; Kim, S. -Y.; Shin, H. -J.; Lee, Z.; Kim, S. Y.; Kwon, S. -Y., Partial Oxidation Behavior of Diverse Intrinsic Graphene Defects in Graphene-Grown Copper. *KCS* **2020**.
11. Song, S.; Kwak, J.; Lee, J. H.; Lee, J.-U.; Kim, S.-Y.; Kim, J. H.; Lee, S.; Sim, Y.; **Jo, Y.**; Cheong, H.; Lee, Z.; Kwon, S.-Y., Electrical Properties of van der Waals WTe_2 Nanobelts Synthesized from Cu_xTe_y Eutectic Alloy. *ENGE* **2018**.

12. Kim, S. -Y.; Kim, J. H.; Lee, S.; Kwak, J.; **Jo, Y.**; Yoon, E.; Lee, G.-D.; Lee, Z.; Kwon, S.-Y., Interlayer Properties of van der Waals Heterostructures with Substrate Surface Defects. *ENGE* 2018.
13. Kim, S. -Y.; Kwak, J.; Kim, J. H.; Lee, J.-U.; **Jo, Y.**; Kim, S. Y.; Cheong, H.; Lee, Z.; Kwon, S. -Y., Remarkably improved air stability of monolayer TMDs on graphene substrate. *KSLOE* **2018,** *Spring meeting*.
14. Sim, Y.; Kwak, J.; Kim, S.-Y.; **Jo, Y.**; Kim, S.; Kim, S. Y.; Kim, J. H.; Lee, C.-S.; Jo, J. H.; Kwon, S.-Y., 3D Graphene-Ni Foam Heterostructures for Highly-efficient and Durable Bipolar Plates in a Polymer Electrolyte Membrane Fuel Cell. *The Korean Ceramic Society* **2018,** *Fall meeting*
15. Kwak, J.; Kim, S.-Y.; **Jo, Y.**; Kim, N. Y.; Kim, S. Y.; Lee, Z.; Kwon, S.-Y., Unraveling the Water Impermeability Discrepancy in CVD-grown Graphene. *The Korean Ceramic Society* **2018,** *Fall meeting.*

ACKNOWLEDGEMENTS

2010년 대학교를 입학한 이후, 10년이라는 시간의 세례를 통하여 지금 졸업 논문의 마지막인 감사의 말을 작성하며 학생 신분에 마침표를 찍으려 합니다. 10년이라는 긴 기간동안 스쳐 지나갔던 많은 사람들의 도움과 배려가 있었기에 이 논문을 완성시킬 수 있었다고 생각됩니다. 저와 인연을 함께한 모든 분들에게 감사인사를 올리며, 긴 과정의 끝에서 느끼고 있는 아쉬움과 설렘, 그리고 후련한 기쁨을 함께 나누고 싶습니다.

우선, 2011년 재료공학개론 수업시간에 그래핀의 세계를 펼쳐 보여주신, 현재 저의 기원이라 할 수 있는, 권순용 교수님께 감사인사 올립니다. 교수님께서 기억하실 지는 모르겠으나 대학원에 들어오기 이전, 신소재 공학부에 들어온 학부생 때부터 교수님께서는 저의 지도교수를 맡고 계셨습니다. 교수님께서 많이 바쁘셔서 수강 신청 승인을 두 번 정도 누락하여 수강 과목의 수정을 해야 했던 추억이 기억나네요. 물론 학부생 때부터 권순용 교수님께서 저의 지도교수님으로 배정된 이 우연이 저는 크나큰 행운이라고 생각합니다. 만약 학부시절부터 교수님께서 저의 지도교수님이 아니셨다면 지금의 저는 없었을 거라 생각이 드네요. 강아지 대통령 강형욱이 강아지를 다루는 모습을 봤을 때, 문득 교수님이 생각이 났던 적이 있습니다. 아마도 교수님의 부드러운 카리스마가 이러한 생각을 들게 했던 거 같아요. 항상 감정을 억제하시고 이성적으로 학생을 대하려고 노력하시는 권순용 교수님. 앞으로 그 부드러운 카리스마로 많은 훌륭한 연구자들을 훈련하여 배출할 것이라 생각이 듭니다. 항상 가정에 평화와 행복이 가득하길 기원하며, 학부부터 대학원까지 저의 학생 기간의 반 이상을 함께해 주셔서 영광입니다. 감사합니다.

다음으로 이 졸업 논문의 심사를 맡아 주신, 박기복 교수님, 송명훈 교수님, 이종훈 교수님께 감사인사 올립니다. 중후한 부드러움을 소유하신 박기복 교수님. 교수님께서 기억하실 지는 모르지만 예전에 프로브 스테이션을 사용하기 위하여 박기복 교수님 실험실에 들어간 적이 있는데, 제가 측정을 하는 동안 옆에서 몽키 스패너를 들고 학생과 함께 장비를 고치고 있던 박기복 교수님의 모습이 기억에 남네요. 언제나 반갑게 인사해주시는 송명훈 교수님. 예전에 교수님 오피스에서 아이언맨 피규어를 봤던 기억이 있는데 이번에 찾아뵈었을 때는 아이언맨 피규어가 보이지 않아 먼가 허전한 기분이 들었어요. 교수님 오피스에 많은 수집품들이 가득 차 있으면 든든할 거 같아요. 수줍은 카리스마의 이종훈 교수님. 럭비를 좋아하셔서 럭비 동아리 지도를 맡아보고 싶다고 말씀하시던 모습이 기억나네요. 물론 럭비 동아리는 없어 검도 동아리 지도를 맡아주셨지만. 그 때 검향의 지도를 맡아 주셔서 정말 감사했습니다. 제가 대학원에 들어오고나서 쥐도 새도 없이

사라졌다는게 조금 아쉽네요. 박기복 교수님, 송명훈 교수님, 이종훈 교수님 세 분의 실험실에 가슴이 웅장해질 좋은 실험 결과가 나오길 기원하고, 세 분의 가정에 신의 축복이 함께하길 기도합니다. 감사합니다.

마지막으로 이 졸업 논문의 심사와 저의 대학원 생활을 함께 동고동락(어떤 의미에선 동거동락)한 곽진성 교수님이자, 진성이형에게 감사인사 올립니다. 처음에 형을 만났을 때, 저희 작은 아버지를 많이 닮으셨다는 생각을 했어요. 그래서인지 형이랑은 대학원 내내 친숙하게 지낼 수 있었던 게 아닌가 생각이 드네요. 첫 인상은 먼가 까칠하고 만사가 다 귀찮은 표정을 짓고 있지만 알고 보면 사려 깊고 수줍음 많은 형이었던 것 같아요. 형과 오랫동안 지내다 보니 많은 추억이 생각나네요. 반바지 입고 실험실 가서 잔소리 들었던 거나 랩미팅 때 컵에 물 담아가서 잔소리 들었던 게 생각나네요. 다른 사람들이 치마를 입든 반바지를 입든 텀블러를 가져가든 아무 말도 안하시면서... 지금 생각해보면 애증 담긴 잔소리였던 거 같아요. 무슨 비행기 게임 노트북에 잠시 깔아서 마지막 클리어하고 만세를 부르던 모습은 사진으로도 있지만 제 기억에 더 선명히 남아 있네요. 또, 라만실에 저를 가둬 두고 혼자 퇴근하던 뒷 모습도 생각나네요. 요즘은 전자 담배 펴서 조용하지만 예전에 연초 필 때 쓰읍 쓰읍 하던 소리가 많이 그리워요. 이야기할 추억은 가득하지만 추억 나열은 이정도만 할게요(할많하않). 실험만 할 수 있으면 어디를 가도 상관없다던 열정을 보여주던 형의 목소리가 아직 생생해요. 물론 이후에 잠시 번아웃이 왔었지만 이번에 창원대에서의 모습을 보니 그 예전의 실험 열정 가득하던 진성이 형으로 돌아온 거 같아서 먼가 뿌듯하고 좋았어요. 이제부터 진짜 교수님으로서 건강한 새싹들을 피우고 멋진 꽃을 맺을 수 있기를 기원할게요. 창원대학교에 소재 혁명의 바람을 일으켜 보셔요. 언제나 가정과 삶에 러브&피스가 가득하기를 기원합니다. 감사합니다.

감사의 말 끝을 맺으며, 언제나 부드럽게 저를 챙겨주던 재경이형, 친동생처럼 후배들을 배려해주는 형덕이형, 엄격하고도 깔끔한 연구실의 질서 수호자 재환이형, 귀찮은 척하면서 챙겨줄 거 다 챙겨주는 태양이형, 연구실을 분위기를 밝혀주는 고명이형, 부드러운 조언을 아낌없이 해주시는 허재훈 박사님. 이하 FIND의 선배님들께 감사인사 올리며, 선배인 듯 선배 아닌 선배 같은 세양이, 학부부터 대학원까지 심리적으로 서로 지탱해주던 도희, 언제나 긍정적으로 저의 시덥잖은 이야기를 잘 들어주는 여선이, FIND의 부드러운 군기반장 승욱이형, 조용히 남의 말에 귀 기울이며 모두와 함께 평화를 추구하는 시현이. 이하 FIND의 동기들에게 감사인사 올립니다. 재원이, 주형이, 영호, 행운이, 일존이, 지훈이. 이 FIND의 후배들이 앞으로 FIND를 멋지게 이끌어 갈 거라고 생각하며, FIND의 뿌리에서 나온 많은 연구자들이 각자의 이상향을 위해 하늘로 뻗어 나가 FIND라는 거대한

대나무숲을 이룰 것이라고 생각합니다. 마지막으로 제가 박사를 딸 때까지 전력으로 지지와 지원을 해준 저의 어머니, 아버지, 누나에게 감사인사를 올리며 감사의 말과 이 논문의 끝을 맺도록 하겠습니다.

다들 항상 건강하세요.

감사합니다.

조 용수 拜上